GEOCHEMISTRY OF VALLE GRANDE MEMBER RING FRACTURE RHYOLITES VALLES CALDERA, NEW MEXICO

by

Terry L. Spell

Submitted in Partial Fulfillment
of the Requirements for the Degree of
Master of Science in Geology

New Mexico Institute of Mining and Technology

Socorro, New Mexico

July 1987

NEW MEXICO BUREAU OF MINES
CAMPUS STATION
SOCORRO, N.M. 87801

TABLE OF CONTENTS

LIST OF TABLES

LIST OF FIGURES

ACKNOWLEDGMENTS

Many people have been invaluable in providing assistance and support throughout this study.

First of all I owe Dr. Philip Kyle, my advisor, for suggesting the project and guiding me through the long process leading to the finished product that you see here. Without him the idea would never have become reality.

Several people at Los Alamos National Laboratory have helped at various times. Dr. Jamie Gardner, my supervisor during summer appointments at the lab, contributed ideas, suggestions, and his obvious enthusiasm to the project. Dr. Frasier Goff provided samples from the VC-1 drillcore. Roland Hagan provided instructions and assistance in the electron microprobe lab for several days. Dave Mann and co-workers were helpful in preparation of thin and polished sections. Finally, the staff of the ESS-1 group provided the use of a vehicle for field work on several occasions.

The New Mexico Bureau of Mines and Mineral Resources helped greatly by providing a field vehicle for almost 3 weeks during June of 1986.

The New Mexico Geological Society kindly awarded me a grant-in-aid which helped finance field work and thin section preparation.

Associated Western Universities provided funding for

two summers without which I would have been unable to accomplish much of the work which went into completion of this project.

Many people at New Mexico Tech have helped along the way. Dr. Dave Johnson provided materials and instructions on making slides. Ted Eggleston, Bill McIntosh, Clay Crow, Tom Kendrick, and Anne Wright helped with many aspects of word processing, modelling, and production of diagrams through the use of various computer programs and software.

This work has benefited from discussions with and reviews by Philip Kyle, John Wolff, Jamie Gardner, Ted Eggleston, and Clay Crow.

Last, but certainly not least, I owe much to my parents who have always given their support, encouragment, and unconditional love, although I am sure they have probably wondered exactly what I've been doing all these years.

ABSTRACT

The Valles Caldera, located near the center of the Jemez Mountains Volcanic Field in north-central New Mexico was formed at ~1.12 Ma following eruption of the upper Bandelier Tuff and subsequent emptying of a large shallow magma chamber. Rhyolite domes and flows of the Valle Grande Member were erupted from at least 14 ring fracture vents encircling the caldera. They range in age from the time of caldera formation to ~0.45 Ma and are volumetrically and temporally the dominant post-caldera eruptives.

Phenocryst assemblages include sanidine (Or_{44-61}) + quartz + plagioclase (An_{7-20}) + biotite + hornblende + Fe-Ti oxides ± zircon ± allanite ± apatite ± clinopyroxene ± orthopyroxene. Changes in mineralogy seen with decreasing age include an increase in the Or component of sanidines, an increase in the An component of plagioclase, and an increase in Al, Ti, Mg, and K content and decrease in Fe and Mn content of biotites. Phenocryst sizes and abundances also increase with decreasing age.

Plots of major and trace elements versus age as well as co-variation diagrams indicate that Valle Grande Member rhyolites can be divided into 3 groups; group 1 ranging in age from 1.18-0.71 Ma, group 2 from 0.55-0.51 Ma, and group 3 at 0.45 Ma. Groups 1 and 2 define differentiation trends in which trace elements such as Rb, Cs, Y, Nb, HREE's, Ta, Pb, Th, and U increase with decreasing age whereas Sr, Ba, Zr, Hf, LREE's, and Eu decrease. Abundances of trace elements may increase or decrease 2-3 fold within eruptive groups. In contrast, major elements remain relatively constant in abundance. Breaks in these trends and subsequent eruption of less differentiated lavas occur at 0.71-0.55 Ma and with the last eruption at 0.45 Ma.

Mechanisms considered or tested to account for the observed differentiation trends include; 1) silicate liquid immiscibility; 2) volatile complexing; 3) Soret (thermal) diffusion; 4) progressive partial melting of a mid to lower crustal source; 5) country rock contamination; and 6) crystal-liquid fractionation involving phenocrysts present in the mode. All of these mechanisms except crystal-liquid fractionation either produce trends opposite to those seen (3,4, and 5) or are difficult to constrain with any degree of certainty (1 and 2). Crystal-liquid fractionation involving side-wall crystallization, rise of a bouyant boundary layer, and collection of differentiated liquids in a stable stratified roof zone of a magma chamber was modelled using the Rayleigh fractionation equation. Acceptable

models for differentiation trends seen in groups 1 and 2 using the earliest erupted (least evolved) rhyolites as parent compositions and the latest erupted (most evolved) rhyolites as daughter compositions were obtained.

Reversals in trends could possibly be accounted for by; 1) disruption of a stable stratified roof zone of a magma chamber by eruption of unusually large volumes of magma; 2) magma mixing; or 3) eruption of a new and totally unrelated magma batch at each reversal. Calculations of volumes of magma erupted relative to age do not totally support mechanism 1. Calculations undertaken to constrain magma mixing indicate that only mixing with another high-silica rhyolite can account for the reversals seen in each case. Recent work has suggested that rhyolites erupted in the Jemez Mountains over the last 2-3 M.Y. represent many separate magma batches and were not derived from one large long-lived magma chamber as was previously thought. Rhyolites of the Valle Grande Member can be interpreted as representing 3 separate magma batches (groups 1, 2, and 3), two of which remained closed systems for sufficient periods of time to generate highly evolved differentiates (groups 1 and 2).

Thermobarometry using two-feldspar equilibria, geobarometry using hornblende rim Al contents, and plots of normative compositions on the Q-Ab-Or diagram indicate that fractionation took place at 1-2 kb pressure (2.5-7.5 km depth) with liquidus temperatures ranging from 724-808 °C.

INTRODUCTION

Location and General Description

The Valles Caldera is located near the center of the Jemez Mountains Volcanic Field in north-central New Mexico (Fig. 1). The Jemez Mountains are a complex volcanic succession built up during late Tertiary to Quaternary times along the western edge of the Rio Grande rift at its intersection with the Jemez Lineament (Fig. 1). To the west volcanic rocks of the Jemez Mountains overlie Precambrian basement and Paleozoic to Mesozoic sedimentary rocks whereas to the east they overlie and are interbedded with Tertiary graben fill sediments of the Rio Grande rift (Doell et al.,1968; Aldrich, 1986). The Valles Caldera, formed upon eruption of the Tshirege Member of the Bandelier Tuff (or upper Bandelier Tuff), is a subcircular depression which is from 23 km (E-W) to 19 km (N-S) in diameter and ranges from approximately 90 to 650 meters in depth. The center of the caldera is dominated by a resurgent structural dome whose high point, Redondo Peak, rises to 3,430 meters above sea level and has over 950 meters of local relief (Smith et al., 1970). In the moat formed between the central dome and the topographic rim of the caldera there are 15 rhyolite domes, flows, and associated pyroclastic rocks that were erupted on or near ring fracture vents after

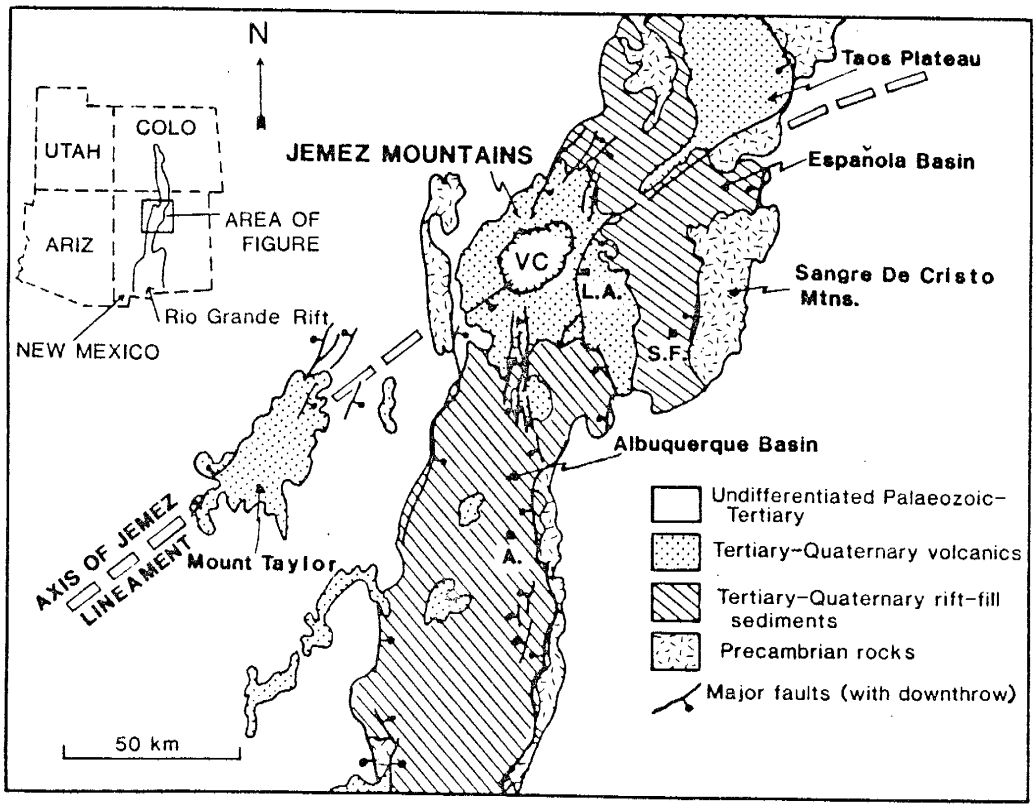

Figure 1. Map showing location of the Jemez Mountains Volcanic Field and the Valles Caldera (VC) in relation to the Rio Grande Rift and the Jemez Lineament (from Self et al., 1986).

caldera collapse and subsequent resurgence. These eruptive units, all members of the Valles Rhyolite Formation of the Tewa Group (Griggs, 1964; Bailey et al., 1969), represent the most recent volcanic activity in the Jemez Mountains and are the subject of this study (Fig. 2).

Objectives

The purpose of this study is to examine the evolution of the post-Bandelier magma system through systematic petrographic and geochemical analysis of the Valles Rhyolite Formation. In particular the Valle Grande Member is examined in detail and compared and contrasted with earlier and later erupted units. Specific problems to be addressed include:

1) Are systematic petrographic and geochemical trends observable within the Valle Grande Member?
2) If trends are seen then what processes can be called upon to explain them?
3) Are eruptive units within the Valle Grande Member a co-magmatic suite?
4) Are all members of the Valles Rhyolite Formation a co-magmatic suite?

Previous Work

The Jemez Mountains Volcanic Field and the Valles

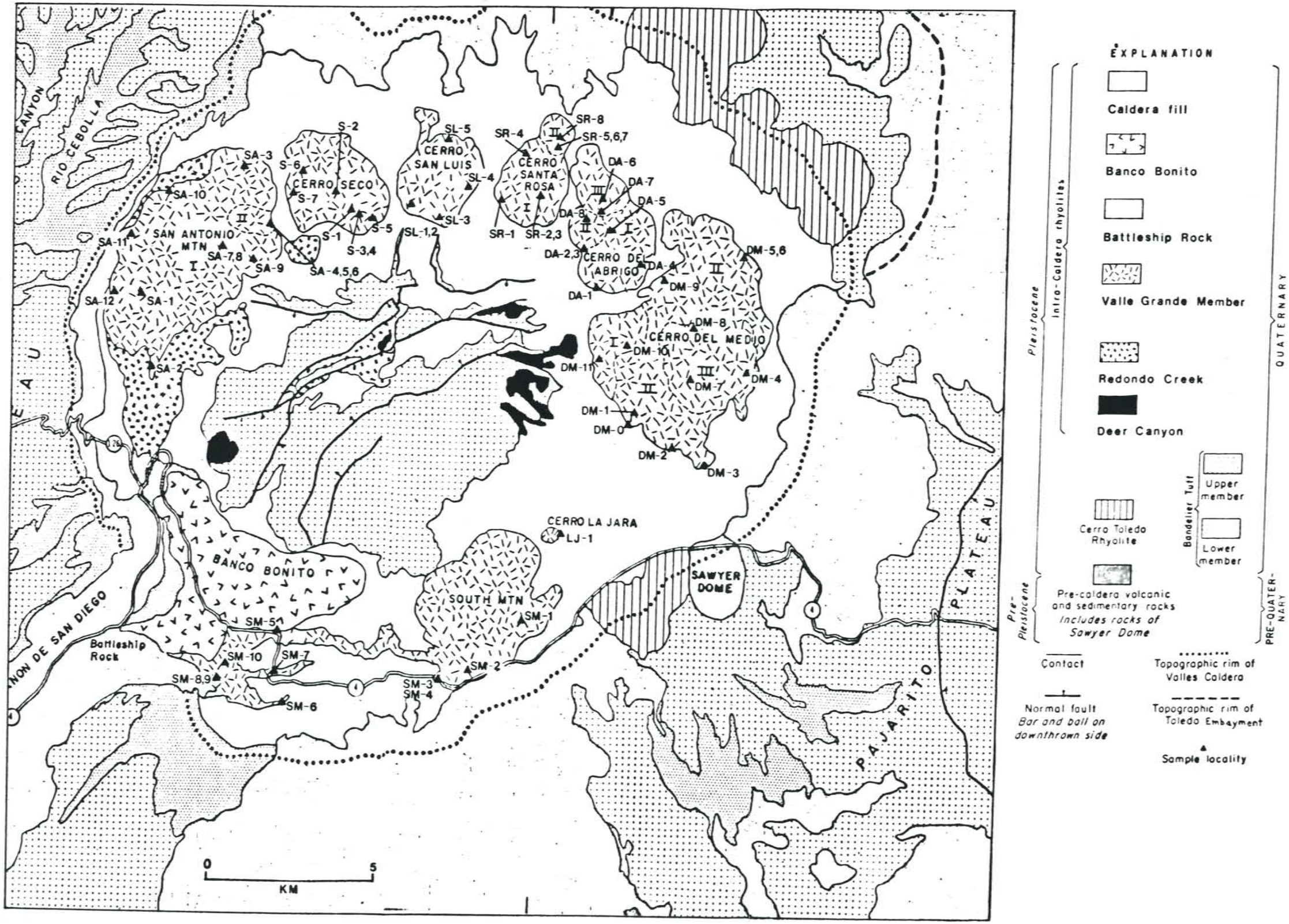

Figure 2. Geologic map of the Valles Caldera showing sample locations (after Doell et al., 1968).

Caldera are best known from the early work of R.A. Bailey, C.S. Ross, and R.L. Smith (Smith et al., 1961; Smith and Bailey, 1968; Bailey et al., 1969; Smith et al., 1970) along with other geologists of the U.S. Geological Survey (Doell et al., 1968). Due to the efforts of these workers the Valles Caldera is generally known today as the "type" resurgent caldera. The work of Doell et al. (1968) was the first to provide chronologic control on the various members of the Valles Rhyolite Formation in the form of K-Ar dating. Various members of the Valles Rhyolite Formation that were unsuitable for radiometric age dating due to hydrothermal alteration were assigned relative ages based on stratigraphy (Doell et al., 1968; Bailey et al., 1969).

Doell et al. (1968) first pointed out that the Valles Rhyolite Formation is petrographically a very heterogenous group. Later workers (Bailey et al., 1969; Prigmore, 1978) confirmed and elaborated on these initial observations. Bailey et al. (1969) suggested that the progressive changes in phenocryst types and abundances seen in the Valle Grande Member with time indicates that it is a coherent group of petrologically related domes.

Smith (1979) gave evidence of systematic changes in Nb concentration with time in the Valles Rhyolite, made some preliminary interpretations, and suggested that similar (and antithetic) patterns for other elements exist. Gardner et al. (1986) note that the Valles

Rhyolite can be divided into two groups based on chemistry with the Deer Canyon, Redondo Creek, and Valle Grande members generally being of a high silica type whereas the younger members are characterized by lower silica but higher Fe, Mg, Ca, Ti, and P.

Methods

The various eruptive units of the Valle Grande Member were located using U.S.G.S. 7.5 minute topo sheets (Redondo Peak, Valle San Antonio, Seven Springs, Jemez Springs, Valle Toledo, and Bland) in conjunction with Plate 1 of Doell et al. (1968) showing the locations of the different sections of composite domes. Samples for geochemical and petrographic analysis were collected during June, 1986. Sample locations are shown on Figure 2. Brief descriptions of sample locations and hand specimens are given in Appendices A and B. Care was taken to collect only fresh glassy rhyolite for analysis, therefore samples showing extensive oxidation, hydration, and/or devitrification were avoided and wherever possible samples were taken from the cores of boulders. All whole rock chemical analyses were performed at New Mexico Tech by X-ray flourescence and instrumental neutron activation analysis. Analyses of phenocryst phases was made by electron microprobe at Los Alamos National Laboratories. Detailed descriptions of analytical methods are given in Appendix D.

DEVELOPMENT OF THE VALLES CALDERA

Volcanism at the site of the present day Jemez Mountains Volcanic Field began in mid-Miocene time in response to renewed tectonic activity along the Rio Grande rift following an apparent lull in activity from 21 to 17 Ma (Gardner and Goff, 1984; Aldrich et al., 1986). The initial eruptive activity is represented by a sequence of alkali basalts found interbedded with rift related sediments of the Santa Fe Group on the eastern edge of the Jemez Mountains. A single K-Ar age on a basanite from this sequence indicates that these basalts were erupted ~16.5 Ma (Gardner and Goff, 1984).

On the basis of stratigraphy and radiometric dating volcanic rocks of the Jemez Mountains were formally assigned to three major groups; the Keres Group, the Polvadera Group, and the Tewa Group by Bailey et al. (1969) (Fig. 3).

Keres Group volcanism ranged from >13 Ma to 6 Ma (Fig. 3) and consisted of a range of compositions from olivine tholeiite through high-silica rhyolite but dominated volumetrically by andesites of the Paliza Canyon Formation. These andesites represent approximately 1,000 Km^3 of magma which is roughly half the volume of the entire Jemez Mountains Volcanic Field (Gardner and Goff, 1984; Gardner et al., 1986).

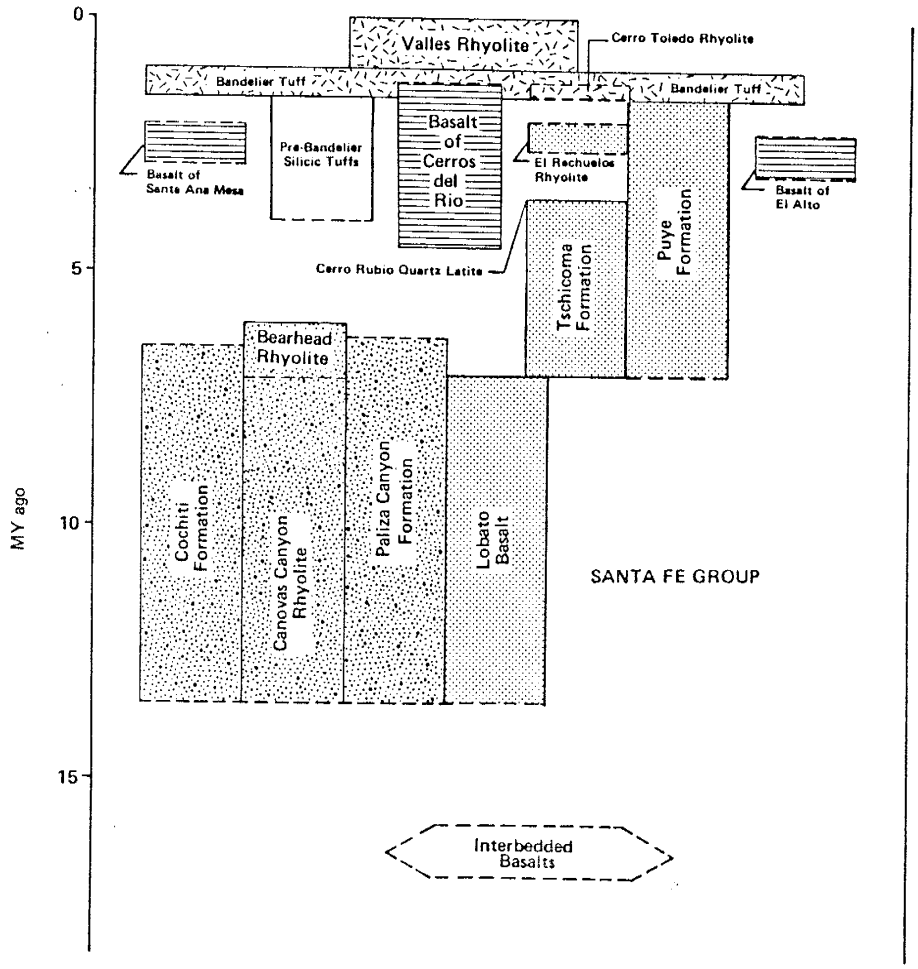

Figure 3. Generalized stratigraphy of major eruptive units in the Jemez Mountains Volcanic Field. Irregular stipple, Keres Group; regular stipple, Polvadera Group; random dash, Tewa Group; horizontal ruling, other eruptives (from Gardner et al., 1986).

Volcanic rocks of the Keres Group overlap temporally with those of the Polvadera Group which were erupted between >13 Ma to <3 Ma (Fig. 3). The Polvadera Group consists of a range of compositions from olivine tholeiite through rhyolite as does the Keres Group. However, the approximately 500 Km^3 of magma erupted to form the Polvadera Group is dominated volumetrically by dacites of the Tschicoma Formation (Gardner and Goff, 1984; Gardner et al., 1986). Basalts of the Lobato Formation are contemporaneous with those of the Paliza Canyon Formation (Fig. 3) and recent work (Gardner et al., 1986) indicates that they are similar in petrography, chemistry, and petrogenesis. Thus, distinctions for reasons other than geographic location may be artificial

Volcanic rocks of the Tewa Group represent the culminating phase of volcanism in the Jemez Mountains. Earlier eruptions of Tewa Group volcanics overlap with waning Polvadera Group volcanism (Fig. 3). As originally defined by Griggs (1964) and Bailey et al. (1969) the Tewa Group includes all volcanics erupted from the time of the Otowi Member of the Bandelier Tuff (or lower Bandelier Tuff) to the present. Recent workers (Kite et al., 1982; Self et al., 1984; Self et al., 1986), however, have recognized several pre-Bandelier ignimbrites in the southwestern Jemez Mountains and have thus extended the age of Tewa Group volcanism back to

~3.6 Ma. Tewa Group volcanism has been almost entirely rhyolitic and is dominated volumetrically by the Bandelier Tuff which represents nearly 600 Km^3 of high-silica rhyolite.

Eruption of the Otowi Member of the Bandelier Tuff (or lower Bandelier Tuff) at 1.40 $\pm$ 0.04 Ma (Izett et al., 1981) was associated with the formation of the Toledo Caldera. Early workers in the area (Doell et al., 1968; Smith and Bailey, 1968; Bailey et al., 1969; Smith et al., 1970) had interpreted the arcuate shaped depression located on the northeast side of the Valles Caldera as being part of the Toledo Caldera (Fig. 2). However, recent workers have redefined the position of the Toledo Caldera ring fracture as being nearly coincident with that of the later formed Valles Caldera (Goff et al., 1984; Heiken et al., 1986).

Eruption of the Tshirege Member of the Bandelier Tuff (or upper Bandelier Tuff) at 1.12 $\pm$ 0.03 Ma (Izett et al., 1981) resulted in formation of the Valles Caldera. Caldera collapse was followed by the formation of a caldera lake, eruption of the Deer Canyon Rhyolite, and accumulation of thick sequences of caldera fill. This was followed by resurgence and doming of the caldera floor along with contemporaneous eruption of the Redondo Creek Rhyolite. This complete sequence of events took place within 100,000 years of caldera collapse (Smith et al., 1961; Doell et al., 1968; Smith and Bailey, 1968).

Rhyolite domes and flows of the Valle Grande Member as well as younger members of the Valles Rhyolite Formation were erupted after structural uplift of the resurgent dome as evidenced by the fact that they are undeformed and untilted (Smith and Bailey, 1968).

Doell et al. (1968) assigned relative ages for the Deer Canyon Rhyolite and the Redondo Creek Rhyolite on the basis of stratigraphy because extensive hydrothermal alteration made accurate radiometric dating impossible.

The Valle Grande Member was found to be free of alteration and dates ranging from 1.18 $\pm$ 0.03 to 0.45 $\pm$ 0.02 Ma (Table 1) were obtained for these rhyolites (Doell et al., 1968). Domes, composite domes, and flows of the Valle Grande Member were erupted on or near ring fracture vents encircling the caldera. There is a general progression of decreasing age when starting with the oldest dome, Del Medio, in the eastern half of the caldera and going counterclockwise (Table 1, Fig. 2).

The younger members of the Valles Rhyolite Formation have since been assigned relative ages both on the basis of stratigraphy and radiometric dating. As a result of the VC-1 drilling project (completed in September of 1984) a previously unknown porphyritic obsidian flow (named the VC-1 Rhyolite) was found which lies stratigraphically above the intracaldera facies of the upper Bandelier Tuff and underlies the Battleship Rock Member in the southwest moat zone of the caldera. The VC-

Table 1. Age relations of the Valles Rhyolite Formation based on stratigraphy and radiometric dating.

Member	Unit	Age (Ma)	Reference
Banco Bonito		0.13 ± 0.10	3
El Cajete		?	2
Battleship Rock		?	"
VC-1 Rhyolite		0.356 ± 0.061	5
	San Antonio II	0.447 ± 0.015*	1
	South Mountain	0.507 ± 0.015*	"
	La Jara	0.516 ± 0.015*	"
	San Antonio I	0.549 ± 0.015*	"
	San Luis	0.711 ± 0.015*	"
	Santa Rosa II	0.726 ± 0.019*	"
Valle Grande	Seco	0.746 ± 0.015*	"
	Santa Rosa I	0.908 ± 0.028*	"
	Del Abrigo III	0.910 ± 0.019*	"
	Del Abrigo II	?	"
	Del Abrigo I	?	"
	Del Medio III	?	"
	Del Medio I	1.068 ± 0.05*	"
	Del Medio II	1.181 ± 0.03*	"
Redondo Creek		?	"
Deer Canyon		?	"
Upper Bandelier		1.12 ± 0.03	4

Unit Abbreviations:
San Antonio II -- SA-II
South Mountain -- SM
La Jara --------- LJ
San Antonio I --- SA-I
San Luis -------- SL
Santa Rosa II --- SR-II
Seco ------------ S
Santa Rosa I ---- SR-I
Del Abrigo III -- DA-III
Del Abrigo II --- DA-II
Del Abrigo I ---- DA-I
Del Medio III --- DM-III
Del Medio I ----- DM-I
Del Medio II ---- DM-II

Note: Units without dates are placed according to stratigraphy as indicated in the reference cited.

* Dates converted using new decay constants after Dalrymple (1979).

References:
1. Doell et al. (1968), 2. Bailey et al. (1969), 3. Marvin and Dobson (1979), 4. Izett et al. (1981), 5. Goff et al. (1986)

1 Rhyolite was subsequently dated by K-Ar and found to be ~0.36 M.Y. old (Goff et al., 1986). The Battleship Rock Member, composed of partly to densely welded ignimbrite, postdates the VC-1 Rhyolite due to its stratigraphic position exposed in the VC-1 drill core. The El Cajete Member, composed of pyroclastic surge, flow, and fall out deposits, is considered to be younger than the Battleship Rock Member due to the fact that it contains numerous inclusions of the Battleship Rock ignimbrite (Bailey et al., 1969). Neither the El Cajete nor the Battleship Rock members have been dated. The last unit to be erupted in the Valles Caldera is the porphyritic obsidian flow of the Banco Bonito Member. This unit overlies the El Cajete Member and has been dated at ~0.13 Ma by the zircon fission track method (Marvin and Dobson, 1979), therefore the Battleship Rock and El Cajete Members are bracketed in age between approximately 0.36 and 0.13 Ma. The later units from the VC-1 Rhyolite to the Banco Bonito Member all seem to have been erupted from vents very near to each other in the southern part of the Valles Caldera (Bailey et al., 1969; Prigmore, 1978). Table 1 summarizes the age relations of all members of the Valles Rhyolite Formation based both on stratigraphy and radiometric dating.

PETROGRAPHY

A total of 31 thin and polished sections representative of the Valle Grande Member were examined. Point counts were taken on 10 thin sections the results of which are shown in Table 2.

Lithologies of the Valle Grande Member range from the aphyric obsidians characteristic of the oldest dome, Del Medio, to the coarsely porphyritic and pumiceous lithologies characteristic of the younger domes, San Antonio, La Jara, and South Mountain. Many of the domes show fresh glass with varying amounts of hydration as evidenced by the perlitic cracks seen in some thin sections examined. Rarely devitrification is seen in the form of spherulites in obsidians and the conversion of glassy rhyolites to dense felsites. Phenocryst assemblages include sanidine + quartz + plagioclase + biotite + hornblende + Fe-Ti oxides (titanomagnetite and ilmenite) $\pm$ zircon $\pm$ allanite $\pm$ apatite $\pm$ clinopyroxine $\pm$ orthopyroxene. Quartz + sanidine + plagioclase always account for >95 % of the mode. Sanidine usually dominates the phenocryst assemblage although quartz may equal or exceed it in abundance (Fig. 11, Table 2). Other phenocrysts are usually found in the relative order listed as far as abundance is concerned.

Sanidine phenocrysts range from 0.2 to 5.0 mm and

Table 2. Modal analyses of selected samples from the Valle Grande Member.

Sample	DM-1	DA-6	SR-1	S-5	SR-7
Dome	DM-III	DA-III	SR-I	S	SR-II
Age (Ma)	~1.181	~0.910	~0.908	~0.746	~0.726
Points					
Glass	599	488	489	481	520
Quartz	6	52	64	45	43
Sanidine	2	53	90	42	55
Plagioclase	0	15	15	6	10
Biotite	0	1	4	0	0
Hornblende	0	0	0	0	0
TOTAL	607	609	662	574	628
% Phenos	1.3	19.9	26.1	16.2	17.2
Mode					
Quartz	75.0	43.0	37.0	48.4	39.8
Sanidine	25.0	43.8	52.0	45.2	50.9
Plagioclase	0.0	12.4	8.7	6.5	9.3
Biotite	0.0	0.8	2.3	0.0	0.0
Hornblende	0.0	0.0	0.0	0.0	0.0
Ave. Size (mm)					
Quartz	0.38	0.71	0.93	1.18	1.19
Sanidine	0.55	0.72	1.13	1.04	1.42
Plagioclase	0.20	0.68	0.53	0.50	0.63
Biotite	0.10	0.49	0.53	0.43	0.56

Table 2. (continued)

Sample	SL-1	SA-2	LJ-1	SM-5	SA-6
Dome	SL	SA-I	LJ	SM	SA-II
Age (Ma)	~0.711	~0.549	~0.516	~0.507	~0.446
Points					
Glass	523	557	528	533	347
Quartz	43	45	72	33	97
Sanidine	68	74	79	53	53
Plagioclase	12	41	35	37	34
Biotite	1	5	6	5	7
Hornblende	0	2	0	0	0
TOTAL	646	724	720	661	538
% Phenos	19.0	23.1	26.7	19.4	35.5
Mode					
Quartz	34.7	26.9	37.5	25.8	50.8
Sanidine	54.8	44.3	41.1	41.4	27.7
Plagioclase	9.7	24.6	18.2	28.9	17.8
Biotite	0.8	3.0	3.1	3.9	3.7
Hornblende	0.0	1.2	0.0	0.0	0.0
Ave. Size (mm)					
Quartz	1.61	1.29	1.74	1.60	1.58
Sanidine	1.26	1.51	1.92	1.95	1.86
Plagioclase	0.68	0.93	1.30	1.13	1.12
Biotite	0.78	0.49	0.53	0.63	0.57

average ~1.3 mm in size. They are found both as isolated euhedral to subhedral crystals and in glomerocrysts with quartz, plagioclase, and rare biotites and Fe-Ti oxides. Rarely sanidines are found as inclusions in plagioclase phenocrysts. Often phenocrysts of sanidine are broken and occasionally they show signs of resorption, although never to the extent that quartz phenocrysts do. Carlsbad twinning is common and a few sector zoned sanidines are often present (Fig. 4).

Quartz is present as anhedral to subhedral phenocrysts ranging from 0.1 to 4.4 mm and averaging ~1.2 mm in size. It is often found as a constituent of glomerocrysts with sanidine and plagioclase. Quartz phenocrysts are often broken and fractured and usually show resorption textures with some crystals being strongly resorbed (Fig. 4). More rarely hexagonal cross sections giving centered optic axis figures and pyramidal terminations are seen. Small (< 0.1 mm) glass inclusions are seen in some crystals.

Plagioclase phenocrysts are usually euhedral, more rarely subhedral, range from 0.2 to 3.8 mm, and average ~0.8 mm in size. They are found both as isolated crystals and in glomerocrysts as described for quartz and sanidine. Rarely plagioclase phenocrysts are broken and even more rarely they may show signs of resorption. They are occasionally found as inclusions in sanidines. Plagioclase almost always shows polysynthetic twinning

Figure 4. Euhedral sanidine exhibiting sector zoning, top left center. Resorbed quartz, lower right. Cross polarized light, field of view = 4.0mm.

and commonly shows oscillatory zoning and core-rim zoning (Fig. 5).

Phenocrysts of biotite are euhedral, range from 0.1 to 1.4 mm, and average ~0.5 mm in size (Fig. 6). They are brown to reddish brown, strongly pleochroic, and often show the characteristic "birds-eye" mottling under cross polarized light. Biotites are fresh and unaltered except in the few samples which were totally devitrified. Often small biotites are found as inclusions in sanidine or plagioclase and they are commonly associated in glomerocrysts with other mafic phases such as hornblende, allanite, and Fe-Ti oxides.

Hornblende is present as euhedral to subhedral phenocrysts, ranging from 0.1 to 1.0 mm, and averaging ~0.4 mm in size (Fig. 7). They are usually brown and pleochroic although a few examples are green in color. Some hornblendes show simple twinning. Although present as isolated crystals, they commonly are found associated with other mafic phases as described for biotite. A few rare examples of hornblende forming as a late magmatic alteration product of the pyroxenes are also seen (Fig. 8).

Fe-Ti oxides (titanomagnetite and ilmenite) occur as anhedral to subhedral phenocrysts and microphenocrysts, ranging from 0.02 to 0.6 mm, and averaging ~0.2 mm in size. They commonly show signs of exsolution; only rarely are unexsolved and unaltered examples seen. The Fe-Ti

Figure 5. Euhedral plagioclase showing oscillatory and core-rim zoning (with hornblende inclusions). Cross polarized light, field of view = 1.3mm.

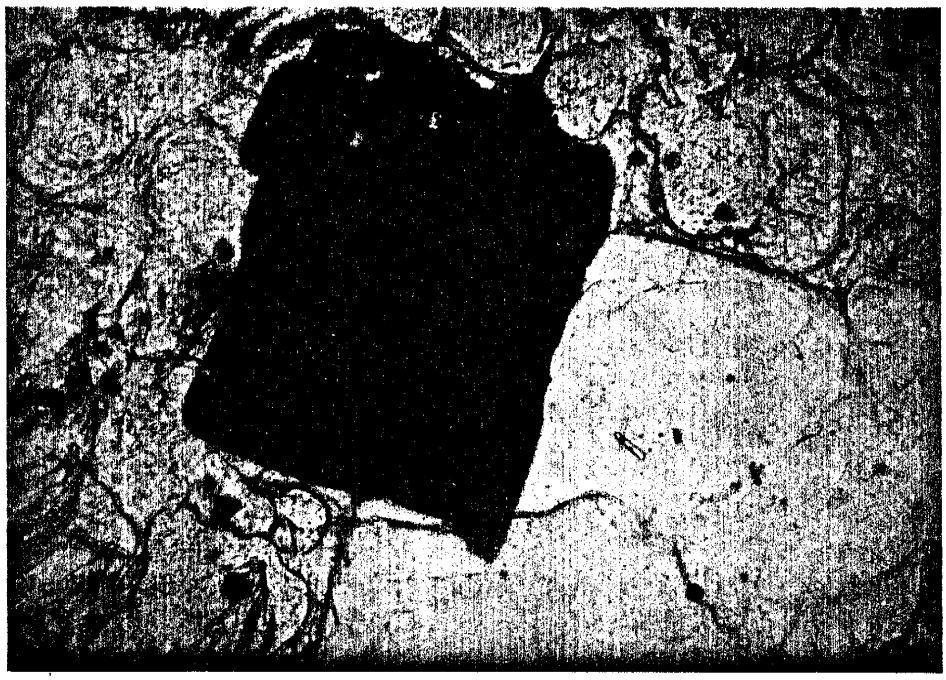

Figure 6. Euhedral biotite (with oxide inclusion) set in glassy, vesicular groundmass, with poorly developed perlitic cracks. Plane polarized light, field of view = 1.3mm.

Figure 7. Euhedral hornblende with included and associated oxides. Plane polarized light, field of view = 1.3mm.

Figure 8. Hornblende forming as an alteration product of clinopyroxene. Cross polarized light, field of view = 1.3mm.

oxides do occur as isolated phenocrysts, but commonly are associated with other mafic phases in small glomerocrysts. They are also common as inclusions in biotite, hornblende, zircon, and more rarely in allanite, sanidine, plagioclase, and clinopyroxene.

Zircon occurs as euhedral to subhedral phenocrysts and microphenocrysts, ranging from 0.02 to 0.6 mm, and averaging ~0.1 mm in size. Most zircons are clear in plane polarized light, although a few show a light greenish color. They are most commonly associated with Fe-Ti oxides and biotite and are found as inclusions in biotite, Fe-Ti oxides, and rarely hornblende, although some are found as discrete phenocrysts. One example seen shows simple twinning.

Non-metamict allanite is present as euhedral to subhedral phenocrysts, ranging from 0.06 to 0.6 mm, and averaging ~0.3 mm in size (Fig. 9). Allanites are light brown to brown to reddish brown in plane polarized light and display a distinct pleochroism. They are found both as discrete phenocrysts and associated with other mafic phases in glomerocrysts.

Apatite occurs as rare euhedral inclusions in biotite and Fe-Ti oxides and even more rarely as microphenocrysts associated with these phases. Apatites range from 0.01 to 0.08 mm, and average ~0.03 mm in size.

Clinopyroxene occurs in only 5 of the 31 thin sections studied. It is subhedral to anhedral, ranging

Figure 9. Non-metamict allanite (with associated Fe-Ti oxides and zircon) set in a glassy, pumiceous groundmass. Plane polarized light, field of view = 0.8mm.

from 0.2 to 0.4 mm, and averaging ~0.3 mm in size. Clinopyroxenes often show alteration rims of hornblende as previously mentioned (Fig. 8).

Orthopyroxene occurs in 2 of the 31 thin sections studied. Two phenocrysts of orthopyroxene were 0.2 and 0.2 mm in size, anhedral, and were altering to fine grained opaques and hornblende.

As was first noted by Doell et al. (1968) and later confirmed by Bailey et al. (1969) and Prigmore (1978) there is a general increase in phenocryst percentages as well as an increase in the abundance of plagioclase and mafic phases going from the older to the younger domes of the Valle Grande Member. This study has both confirmed and provided further documentation of these trends. The total phenocryst content varies from 1.5% to 35.5% when going from the oldest dated dome (Del Medio II at 1.18 Ma) to the youngest (San Antonio II at 0.45 Ma) (Fig. 10). The sample providing the data point for Del Medio II (DM-1) is a pumiceous rhyolite and is sparsely porphyritic. However, some obsidian samples from Del Medio II are totally aphyric. There is also an increase in the percent of plagioclase in the mode going from older to younger domes (Fig. 11). Beginning with Del Medio II (at 1.18 Ma) there is only a trace of plagioclase present which increases until reaching a high of 28.9% with eruption of the next to the youngest unit (South Mountain at 0.51 Ma). Biotite shows an increase in

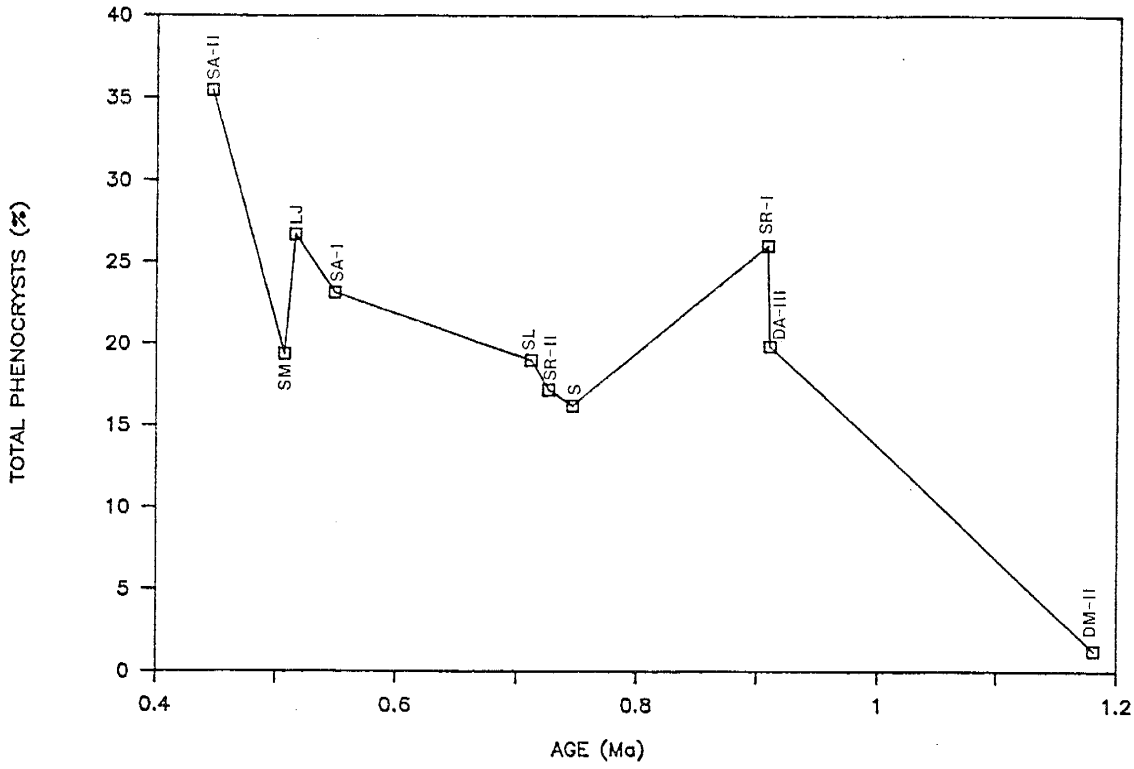

Figure 10. Plot of total phenocryst content vs age for the Valle Grande Member.

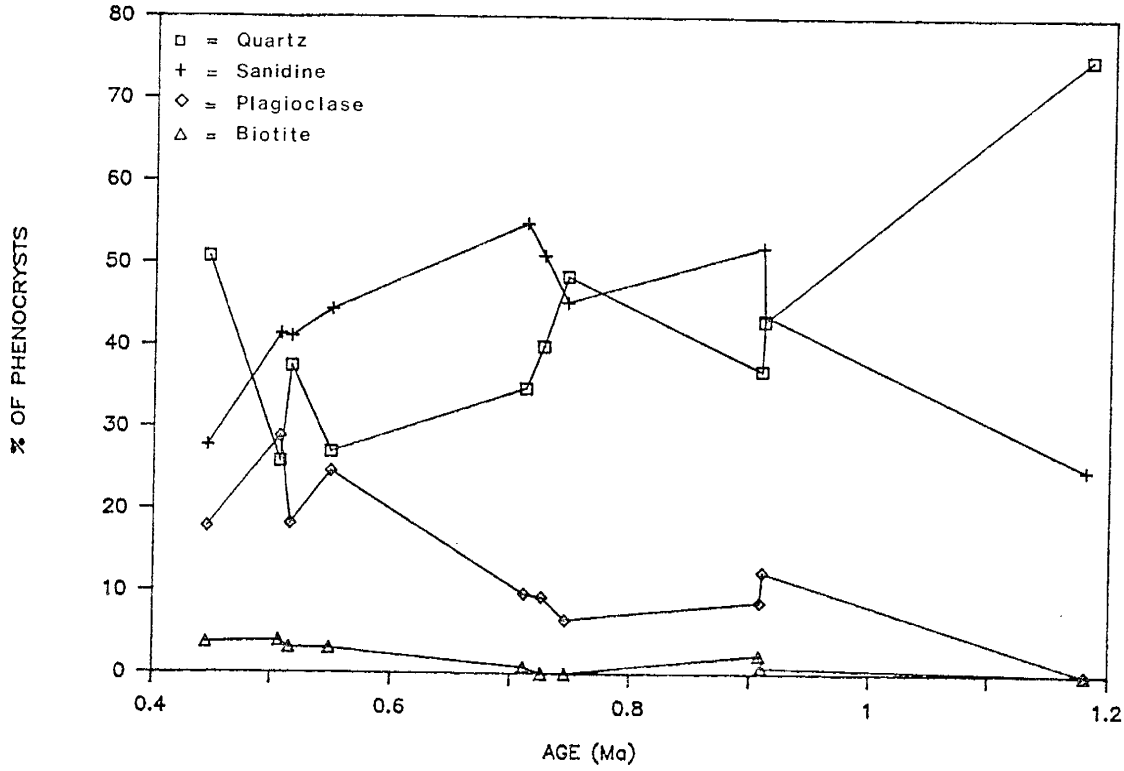

Figure 11. Plot of relative abundances of phenocryst species vs age for the Valle Grande Member.

abundance with decreasing age of the domes ranging from trace amounts to 3.9% (Fig. 11). Hornblende and the Fe-Ti oxides also show a general increase in abundance with decreasing age similar to biotite. Abundances of quartz and sanidine show an inverse relationship (Fig. 11).

Average phenocryst size also increases with decreasing age of eruptive units in the Valle Grande Member (Fig. 12). Quartz, sanidine, plagioclase, and biotite all show a 2 to 3 fold increase in average size going from the oldest to the youngest domes. Hornblende, Fe-Ti oxides, and allanite exhibit the same trend.

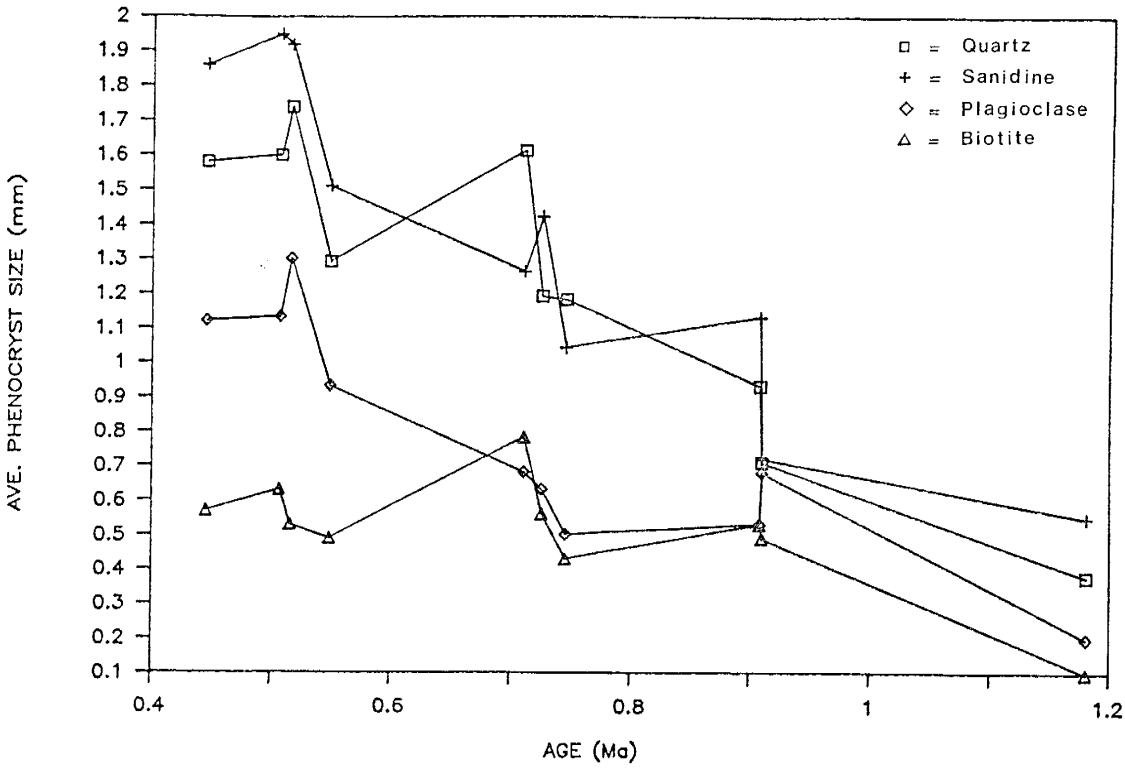

Figure 12. Plot of average phenocryst sizes vs age for the Valle Grande Member.

MINERAL CHEMISTRY

Introduction

Phenocrysts in 8 polished sections were analyzed by electron microprobe (analytical methods are described in Appendix D). The 8 sections chosen represent all dated eruptive units of the Valle Grande Member with the exception of Del Medio I, La Jara, and San Antonio II (Table 1). Phenocryst phases analyzed include sanidine, plagioclase, biotite, hornblende, titanomagnetite, and ilmenite. Complete data tables for mineral analyses are given in Appendix E.

Sanidine

All potassium feldspars analyzed plot as sanidine on the Or-Ab-An ternary feldspar diagram with the exception of one rim composition which plots as anorthoclase (Fig. 13). Systematic core-rim zoning is absent and most sanidines are relatively homogenous.

The total range of compositions seen for sanidines (omitting the one anorthoclase rim) is $Or_{44.4 - 61.2}$. Sanidines from units 0.71 Ma and older show a range of rim compositions from $Or_{44.4}$ to $Or_{54.6}$ with the more sodic sanidines belonging to the oldest units. Sanidines from the younger units (< 0.71 Ma) have sanidine rim compositions ranging from $Or_{58.4}$ to $Or_{61.2}$. Although

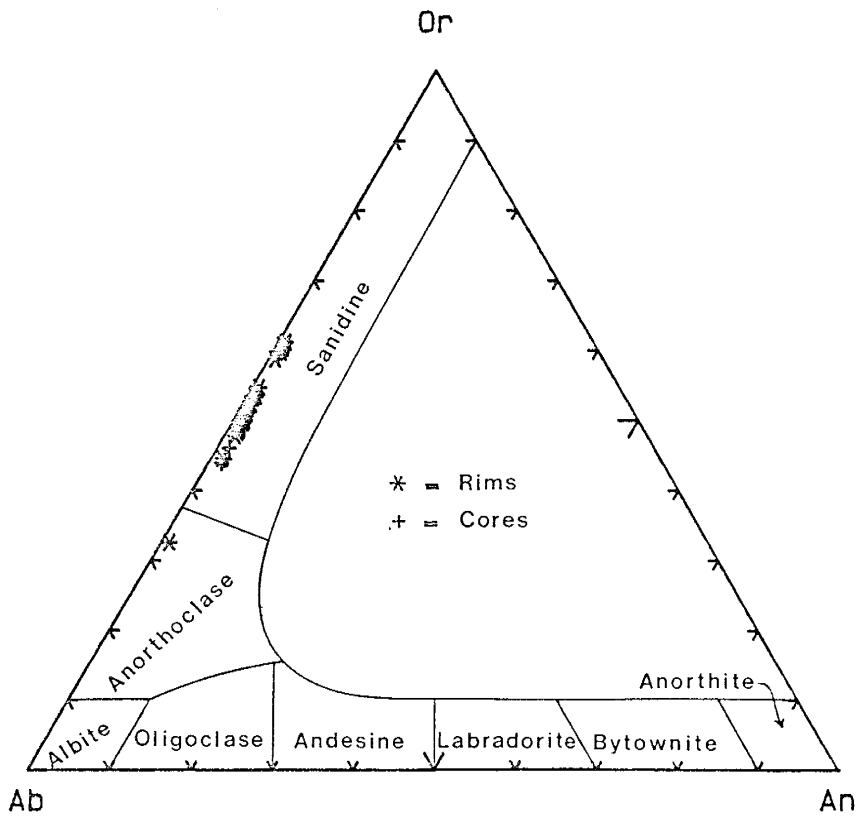

Figure 13. Or-Ab-An ternary feldspar diagram showing compositions of K-feldspars analyzed during this study (classification after Deer et al., 1982).

there was no petrographic evidence for vapor phase overgrowths in any of these rhyolites this possibility cannot be ruled out as an explanation for the one anorthoclase rim composition. No systematic variations in the compositions of sanidines with age other than the relative amounts of Na_2O and K_2O are seen.

Plagioclase

Plagioclase feldspars are chemically more complex than sanidines. The majority plot in the oligoclase field on the Or-Ab-An ternary feldspar diagram (Fig. 14). Most samples fall in the sodic end of the oligoclase field. A few samples plot in the corner of the albite field and a very small number actually plot in the anorthoclase field. One core was more calcic than the rest of the population and plots in the andesine field. This marked difference in composition suggests that it may be xenocrystic in origin.

The total range of plagioclase compositions is $An_{7.1}$ to $An_{37.4}$. Overall plagioclase phenocrysts become more potassic as Na increases (Fig. 14). Plagioclase from units 0.71 Ma and older has rim compositions ranging from $An_{7.1}$ to $An_{10.6}$ with samples from Del Abrigo III (0.91 Ma) showing more analyses at the high end of the range. Plagioclase from San Antonio I (0.55 Ma) has rim compositions of $An_{12.4}$ to $An_{18.7}$ whereas plagioclase from South Mountain (0.51 Ma) is the most calcic analyzed with

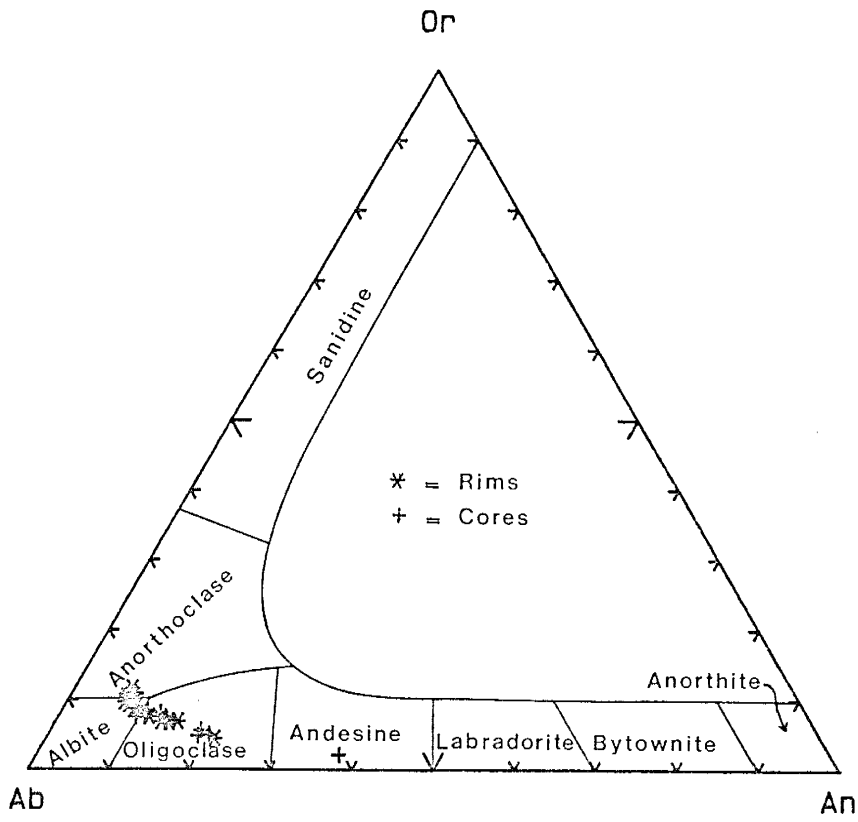

Figure 14. Or-Ab-An ternary feldspar diagram showing compositions of plagioclase phenocrysts analyzed during this study (classification after Deer et al., 1982).

rim compositions ranging from $An_{18.7}$ to $An_{20.1}$. Both normal and reverse zoning are common with normal zoning being slightly more prevalent. The only other compositional variation seen in plagioclase feldspars is a small but irregular increase in the Fe content when going from older to younger eruptive units.

Biotite

Biotites were analyzed in only 4 domes owing to their relative scarcity. Analyses were obtained from Seco (0.75 Ma - 1 analysis), San Luis (0.71 Ma - 2 analyses), San Antonio I (0.55 Ma - 3 analyses), and South Mountain (0.51 Ma - 1 analysis).

On a cation plot of Fe/Fe + Mg vs Al showing ideal end members (Fig. 15) biotites analyzed fall towards the low Al side and show roughly equal proportions of the annite and phlogopite molecule. Biotites from the youngest domes show the highest Al content and are displaced away from the annite-phlogopite boundary. Other changes in biotite chemistry with time include lower Fe and Mn along with higher Ti, Mg, and K with decreasing age of the eruptive unit.

Fluorine contents of biotites were surprisingly high. Almost all analyses show some fluorine and many show amounts in excess of 3 wt. %. One analysis showed 3.89 wt. % (sample S1-B1, Appendix E). All biotites analyzed also contain a small amount of Cl. Unfortunately

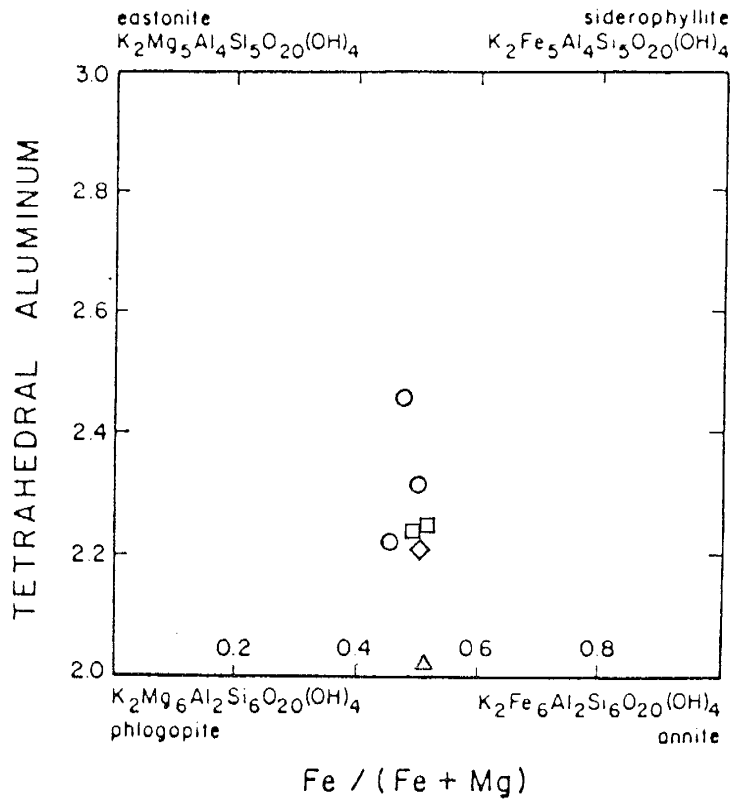

Figure 15. Compositions of biotites analyzed during this study. Cations calculated on the basis of 22 oxygens (classification after Speer, 1984).
Triangle = Seco
Squares = San Luis
Circles = San Antonio I
Diamond = South Mountain

Cl levels were at or just below detection limits (~0.1 wt.%) and thus are not reported in the data tables.

Hornblende

Hornblende was analyzed in samples from Santa Rosa I (0.91 Ma - 2 analyses), Santa Rosa II (0.73 Ma - 1 analysis), and San Luis (0.71 Ma - 1 analysis).

On a cation plot of Fe/Fe + Mg vs Si samples plot in several different fields (Fig. 16). Two samples plot as ferro-edenite, one as edenite, and one as edenitic hornblende. All have Fe/Fe + Mg ratios of approximately 0.5, however, Si decreases with decreasing age. No other systematic variations in composition with age for these four samples are seen.

As with the biotites, hornblendes contain large amounts of fluorine. All hornblendes show some fluorine with a few examples ranging up to ~2.5 wt. %.

Titanomagnetite

Three grains of titanomagnetite were analyzed (Appendix E), two from Santa Rosa II (0.73 Ma) and one from South Mountain (0.51 Ma). Compositions ranged from $Usp_{25.6}Mt_{74.4}$ to $Usp_{15.6}Mt_{84.4}$ with the magnetite from the youngest dome being more deficient in the Usp component. Other variations seen between the older and younger domes represented by these samples include higher Al, Cr, and Mg in magnetites from the younger dome.

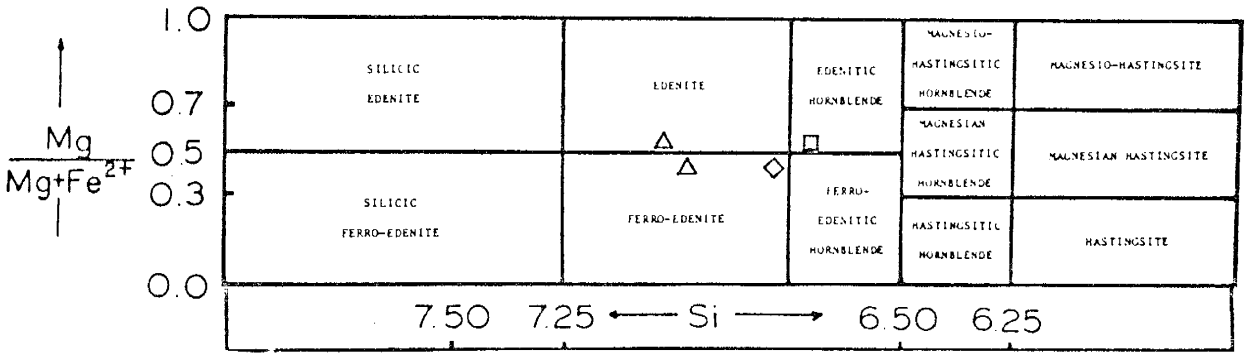

Figure 16. Compositions of amphiboles analyzed during this study. Cations calculated on the basis of 23 oxygens (classification after Hawthorne, 1981).

Triangles = Santa Rosa I
Square = Santa Rosa II
Diamond = San Luis

Ilmenite

One grain of ilmenite gave an acceptable analysis (Appendix E). This ilmenite (from SA-8) had a composition of Il_{86} and was characterized by high Mn content (5.77 wt.%).

Others

One grain of allanite was analyzed by microprobe confirming the existence of allanite in these rocks which, up to this point, had been based purely on petrographic evidence. Semiquantitative analysis gave a Ce content of 8.8 wt.%.

Seven analyses of glass co-existing with the phenocryst assemblage seen in these rocks were made. They are reported in Appendix E and will not be discussed here.

Geothermometry-Geobarometry

It was hoped that co-existing pairs of magnetite and ilmenite would be found so that the Fe-Ti oxide geothermometer (Buddington and Lindsley, 1964) could be used to estimate a temperature of formation and oxygen fugacity for these magmas. This did not prove to be possible, however, due to the relative scarcity of these phases, unacceptably low totals on most analyses, and since both phases were never analyzed for in the same

sample. The fact that most mineral analyses were of co-existing sanidine and plagioclase, however, provides the option of using a geothermometer based on feldspar equilibrium.

Until the work of Green and Usdansky (1986) two feldspar geothermometers have been based solely on the distribution of the albite component between co-existing k-feldspar and plagioclase (e.g., Stormer, 1975). These earlier formulations of the geothermometer did not take into account the fact that in natural feldspar pairs there is limited solution of the Or component in plagioclase and the An component in k-feldspar. Thus, these earlier versions were attempting to model a ternary solution system as two separate binary systems which introduced serious shortcomings into the thermodynamic basis upon which they were built (Brown and Parsons, 1981). One of the problems involved in the development of a true ternary feldspar geothermometer has been the fact that there is limited experimental and thermodynamic data on mixing relations in the An-Or binary system. Until recently it has been assumed that the limitations imposed by this lack of data preclude the development of a ternary geothermometer (Brown and Parsons, 1985). Green and Usdansky (1986), however, have reviewed the existing data and have derived the necessary thermodynamic parameters for mixing relations in the An-Or binary. This data has been combined with the existing data on the

Ab-Or and the Ab-An binary systems to develop a two feldspar thermometer which takes into account the ternary behavior of natural feldspar pairs.

Previous feldspar geothermometers required that a pressure of equilibration be estimated so that a unique temperature could be solved for (e.g., Stormer, 1975). A geothermometer which takes into account ternary behavior, however, will theoretically give a unique solution for both temperature and pressure. On a plot of temperature versus pressure each end member component (Or, Ab, and An) will define a equilibrium curve all of which should intersect at one point assuming perfect equilibrium conditions. Non equilibrium feldspar pairs would be expected to give multiple intersections (Green and Usdansky, 1986). Thus the closure of these intersections will define both temperature and pressure (with their associated errors) and should also give some indication as to how closely the ideal of equilibrium was approached. Other factors which can influence the effectiveness of this "thermobarometer" include analytical errors in estimating the Or in plagioclase and the An in k-feldspar as well as any errors in the calculated thermodynamic properties for the An-Or binary (Green and Usdansky, 1986).

Rim compositions of co-existing sanidine and plagioclase were taken from each sample analyzed and used to calculate temperatures and pressures for the Valle

Grande Member rhyolites (Table 3) using the ternary feldspar thermobarometer of Green and Usdansky (1986). Temperature estimates range from 724 - 808 °C and average around 755 °C. It appears possible that the feldspars from Del Medio III, San Antonio I, and South Mountain equilibrated at slightly higher temperatures than those from the other domes, however, due to the errors in the estimates this cannot be discerned with certainty. The temperatures obtained in this study are identical (within limits of error) to those obtained by Prigmore (1978) using an older version of the two feldspar geothermometer, although they tend to be slightly higher on the average. Pressure estimates show a much greater variability and range of error than do temperature estimates (Table 3). Pressure estimates range from 3.3 - 7.7 kb, however, the range of error is often as high as $\pm$100 % and thus not much confidence can be placed in these numbers.

The generally larger errors for the temperatures calculated using the ternary feldspar thermobarometer in this study as compared to typical errors of $\pm$50 °C for the Fe-Ti Oxide geothermometer (Buddington and Lindsley, 1964) are difficult to attribute to any one factor in particular. Analytical errors in the microprobe data are one possibility due to the fact that molecular proportions of An in sanidines are often <1 %. There is also the probability of varying amounts of disequilibrium

Table 3. Calculated ternary feldspar temperatures and pressures using the method of Green and Usdansky (1986).

Temperatures (°C)

Sample	Dome	Age (Ma)	Mean Temp.	Temp. Range
DA-6	DA-III	~0.910	777 ± 95	756 - 792
SR-4	SR-I	~0.907	724 ± 72	715 - 759
S-1	S	~0.746	726 ± 47	707 - 740
SR-8	SR-II	~0.726	740 ± 64	724 - 757
SL-4	SL	~0.711	724 ± 52	711 - 749
SA-8	SA-I	~0.549	787 ± 68	734 - 874
SM-4	SM	~0.507	808 ± 111	746 - 854

Pressures (kb)

Sample	Dome	Age (Ma)	Mean Press.	Press. Range
DA-6	DA-III	~0.910	7.1 ± 5.9	5.4 - 8.4
SR-4	SR-I	~0.907	4.9 ± 4.8	4.5 - 5.2
S-1	S	~0.746	3.9 ± 3.0	2.8 - 5.2
SR-8	SR-II	~0.726	4.1 ± 4.1	3.6 - 5.6
SL-4	SL	~0.711	3.3 ± 3.4	2.7 - 4.6
SA-8	SA-I	~0.549	6.6 ± 3.6	4.5 - 9.3
SM-4	SM	~0.507	7.7 ± 5.9	5.7 - 9.7

being represented by the feldspar pairs used in these calculations since resorption textures are common in many of the thin sections studied (see Petrography and Appendix C). Pressure estimates could be influenced by the same source of errors. Tests conducted by varying the proportions of Or in plagioclase and An in sanidine have indicated that the pressure estimate is much more sensitive to these parameters than is the temperature estimate.

Work begun by Hammarstrom and Zen (1986) and later confirmed and refined by Hollister et al. (1987) has shown a linear correlation of total Al (cation proportion) in hornblende with pressure. The resulting hornblende geobarometer allows the direct use of microprobe data to calculate a pressure of crystallization. This geobarometer was developed through studies of calc-alkaline granitic plutons and has subsequently been applied only to plutonic rocks. The basic assumption is that the hornblende is in equilibrium with the mineral assemblage and remaining melt at the time of crystallization of the pluton and thus upon final solidification the pressure is reflected in the Al content of hornblende rims (Hollister et al., 1987). It is considered here that the application of this geobarometer to volcanic rocks such as these is justified since equilibrium between hornblende and melt + phenocryst assemblage is in effect instantly "frozen in"

upon eruption. In fact this situation probably more closely reflects equilibrium conditions than slow plutonic cooling. Other conditions for application of this geobarometer as outlined by Hollister et al. (1987) are for the most part met by its use here with few exceptions. Thus, pressure estimates obtained by its use are considered good approximations for the final equilibration of phenocryst assemblages prior to eruption.

Unfortunately only 4 analyses of hornblendes were obtained during this study. The four analyses give a similar pressure of about 1 kilobar (Table 4). Hollister et al. (1987) suggest an error in these calculations of $\pm$1 kb and thus all estimates shown in Table 4 indicate equilibration pressures of <2 kb maximum. This is probably a much more accurate indication of pressure than those obtained using the feldspar thermobarometer for several reasons. The Al content of hornblende is well above detection limits whereas some components in the feldspar analyses which are vital to the calculations using that geobarometer are present in very low abundances (ie: Ca in sanidines). The sensitivity of the feldspar pressure estimates to analytical errors has already been discussed. Also, pressure estimates of <2 kb are in agreement with data from plots of normative compositions in the Q-Ab-Or ternary minimum system. This is treated in more detail in the Discussion section.

Table 4. Pressures calculated by the hornblende geobarometer of Hollister et al. (1987).

Sample	Dome	Age (Ma)	Pressure (kb)
SR-4	SR-I	~0.907	0.98 ± 1.0
SR-4	SR-I	~0.907	0.95 ± 1.0
SR-8	SR-II	~0.726	1.04 ± 1.0
SL-4	SL	~0.711	1.03 ± 1.0

WHOLE ROCK CHEMISTRY

General

The samples collected for this study were plotted on various diagrams commonly in use for classification purposes. One of the more recent classification schemes proposed for fresh volcanic rocks is that of the IUGS Subcommission on the Systematics of Igneous Rocks as summarized by LeBas et al. (1986). This classification uses a total alkali ($Na_2O + K_2O$) vs SiO_2 diagram divided into 15 separate fields representing various rock types. All samples of the Valle Grande Member plot in the rhyolite field on this diagram (Fig. 17). On a K_2O vs SiO_2 classification diagram from Ewart (1979), which divides the rhyolite field into high-K rhyolite, rhyolite, and low-K rhyolite, all samples plot in the high-K rhyolite field. If 75% SiO_2 (calculated anhydrous) is taken as dividing rhyolite from high-silica rhyolite (Hildreth, 1981) then all samples with the exception of one (SA-3 at 74.77% SiO_2) can be classified as high-silica rhyolites. All samples are metaluminous to weakly peraluminous as indicated by small amounts of corundum in the norm of approximately half the samples. In summary, all samples of the Valle Grande Member may be refered to as high-silica, high-K, metaluminous to weakly peraluminous rhyolites. They are simply refered to as rhyolites in the following pages. Complete tables of

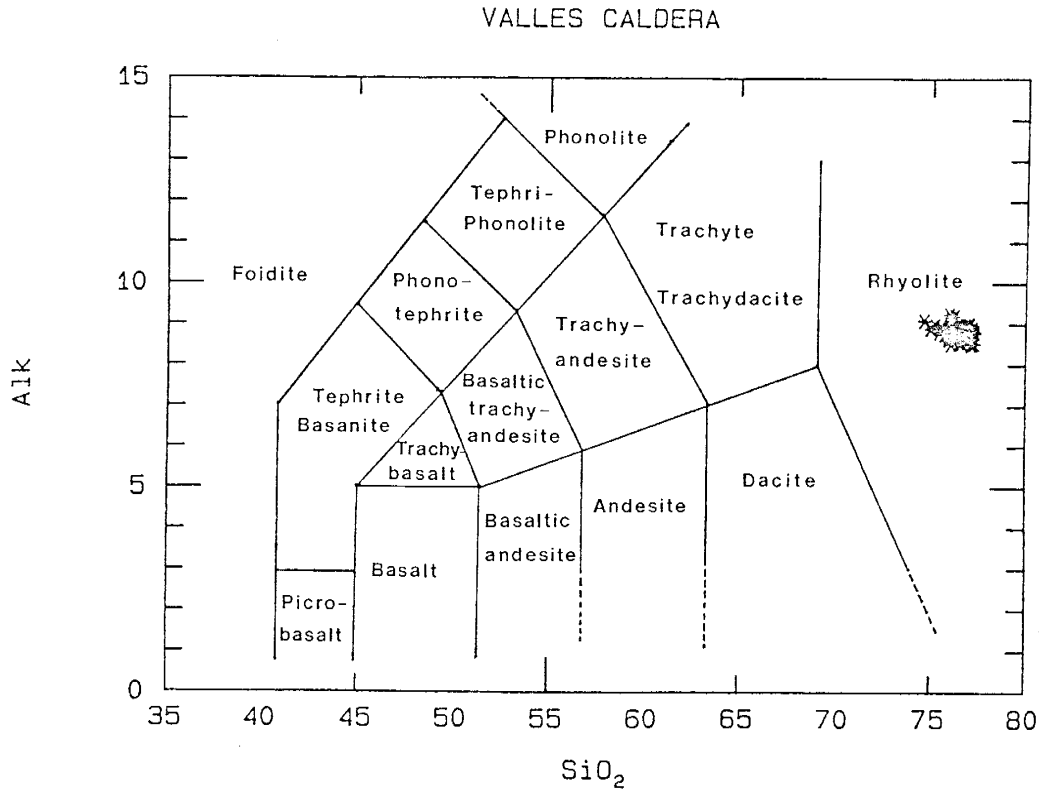

Figure 17. Total alkalis ($Na_2O + K_2O$) vs SiO_2 classification diagram for the Valle Grande Member (classification after LeBas et al., 1986). All analyses recalculated to 100% anhydrous and expressed in wt.%.

analyses are given in Appendix F.

Eight of the 55 analyzed samples from the Valle Grande Member were from undated parts of composite domes (Del Medio III, Del Abrigo I, Del Abrigo II) (Fig. 2, Table 1). Since much of the presentation and interpretation of geochemistry that follows is based upon the age of samples these 8 are not plotted. However, a discussion of their relative ages based on trace element geochemistry and how well this compares to relative ages assigned to them by Doell et al. (1968) is given under the Undated Domes section of the Discussion.

Variation diagrams for suites of rocks presumed to be co-magmatic are usually plotted as a function of silica content. This was not possible because all samples have similar major element composition. It was therefore necessary to choose a trace element which increases with differentiation (decreasing age), is easily and accurately analyzed, and is unaffected by secondary processes such as hydration. Cs, Rb, and Nb all show large increases in abundance with differentiation and have good analytical precision. Nb was chosen since it is unlikely to be mobilized during hydration and devitrification. Thus, in the following sections plots of major and trace elements versus Nb serve to show compatible or incompatible behavior of the element in question. As will be shown, Valle Grande Member rhyolites can be divided into three separate groups based on

elements versus age plots. These groups are plotted as three separate symbols on Nb co-variation diagrams.

Variation Within Age Groups

Before discussing changes in major and trace element abundances with age it is appropriate to address the variation seen in these elements within age groups. Although both major and trace elements exhibit variability within age groups the major elements generally show much larger variability. Often with the major elements the variability within each age group is nearly as great as the total variability seen in all the samples. Whereas some trace elements may show significant variability within age groups, usually the variability between age groups is much greater.

Variations with Age

Plots of major and trace element abundances as a function of age show definite patterns. The patterns are much more pronounced for trace elements.

Major Elements vs Age

The range in major element compositions is restricted. Compared to trace elements abundances which may vary 2-3 fold (see Trace Elements vs Age) the major element variations are relatively minor. There are, however, discernable trends on many plots.

SiO_2 abundances vary little with age (Fig. 18), ranging from 74.8 to 77.4 wt. % (calculated anhydrous). Commonly the range of values for SiO_2 at any given age is nearly as much as this total variation. The only appreciable change in silica seen is the slightly lower values at 0.55 Ma.

No significant variations with age are shown by Al_2O_3, Na_2O, and K_2O (Fig. 18). As with SiO_2 the range of values for these oxides at any given age is almost as large as the total variation that they show.

TiO_2, Fe_2O_3, CaO, and P_2O_5 display definite variations with age (Fig. 19). From 1.18-0.71 Ma Fe_2O_3 and P_2O_5 decrease slightly in abundance whereas TiO_2 and CaO show relatively constant abundances. All four show a sharp increase in abundance with the next eruption at 0.55 Ma, a decrease in abundance from 0.55 to 0.51 Ma, and another increase in abundance with the youngest eruption at 0.45 Ma. It should be pointed out here that, although definite changes in the abundance of these oxides are seen on these diagrams, they are for the most part rather small. Also it should be kept in mind that some of these oxides are present in exceedingly small amounts and in some cases may be at or near detection limits.

MnO and MgO show much less well defined variations with age (Fig. 20). MnO shows a general increase with decreasing age and then declines back to base levels with

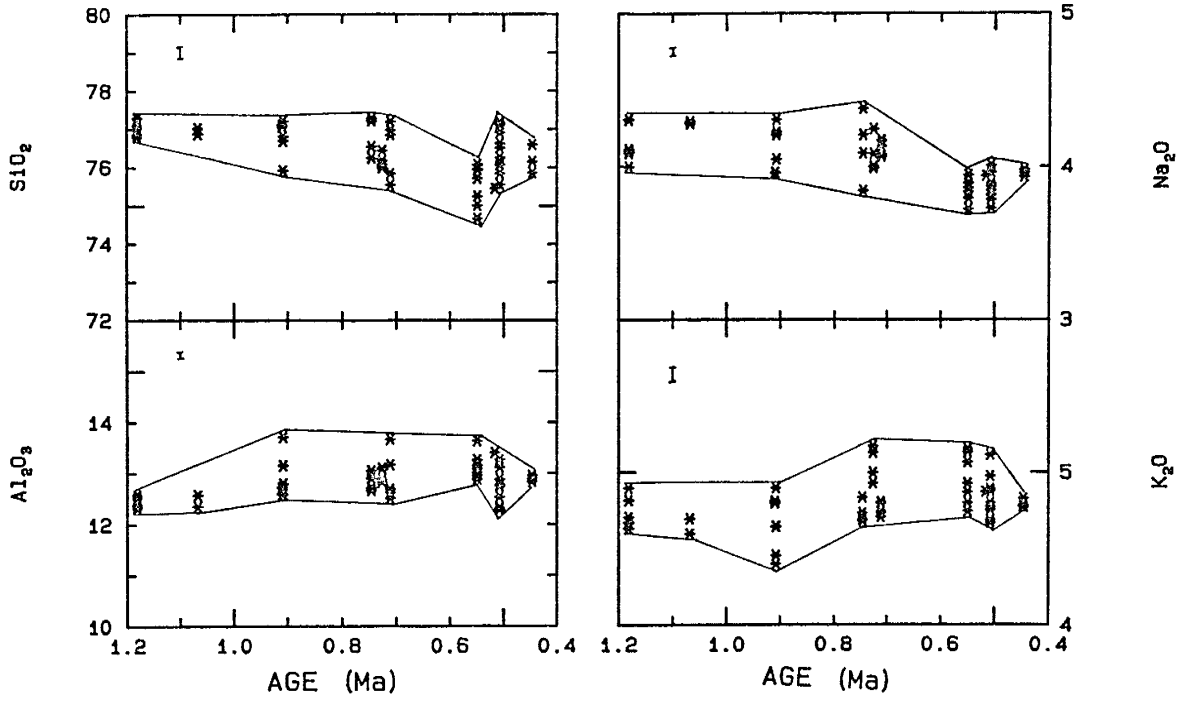

Figure 18. Major elements SiO_2, Al_2O_3, Na_2O, and K_2O plotted as a function of age. All oxides recalculated to 100% anhydrous and expressed in wt.%. Error bars show analytical precision.

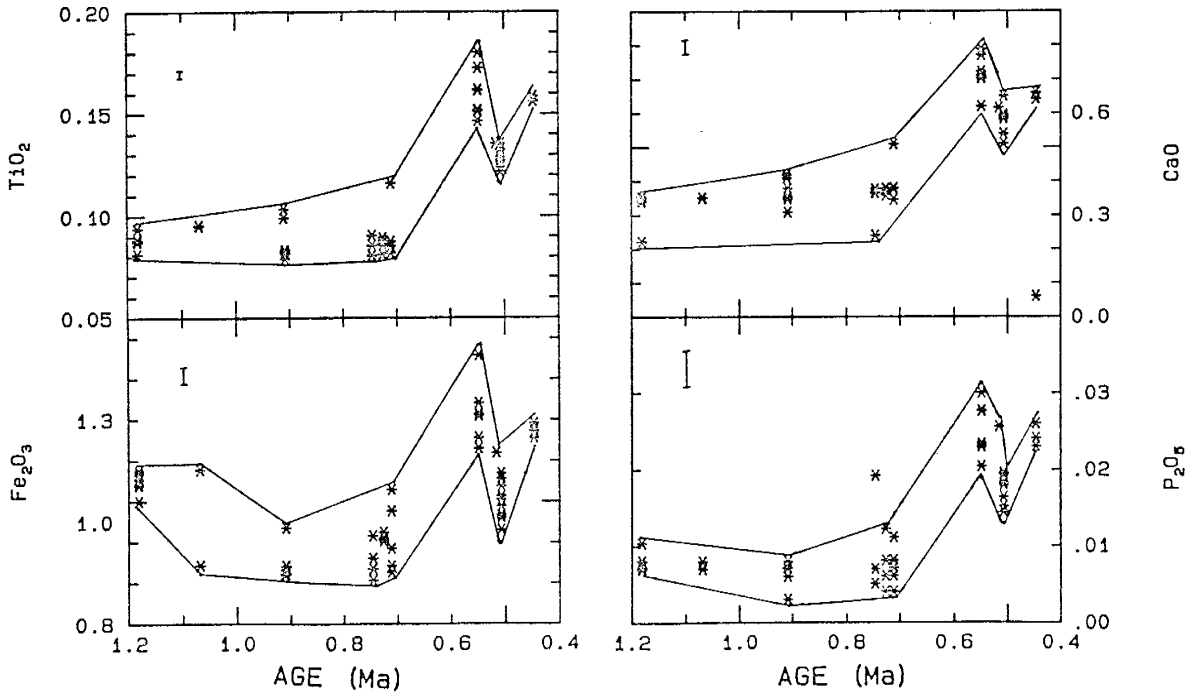

Figure 19. Major elements TiO_2, Fe_2O_3, CaO, and P_2O_5 plotted as a function of age. All oxides recalculated to 100% anhydrous and expressed in wt.%. Error bars show analytical precision.

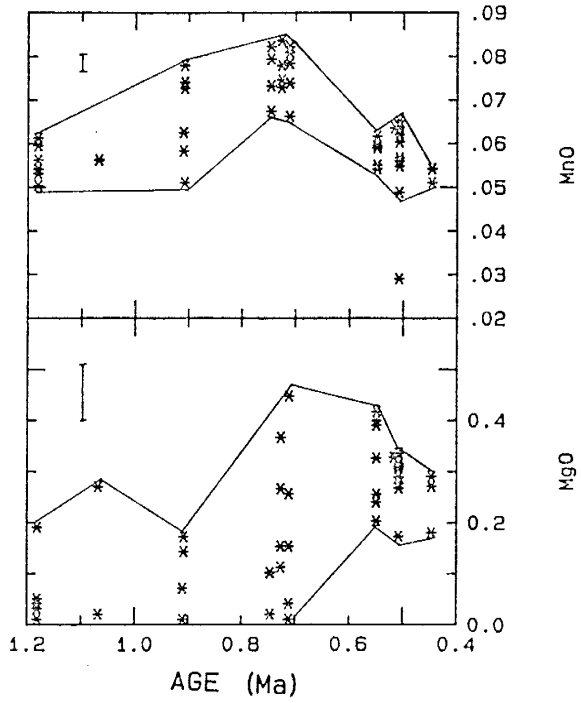

Figure 20. Major elements MnO and MgO plotted as a function of age. All oxides recalculated to 100% anhydrous and expressed in wt.%. Error bars show analytical precision.

the younger eruptions. It is difficult to visualize any systematic variations for MgO due to the large amount of scatter in the data. There may be an increase in the abundance of this oxide with the more recent eruptions (0.55-0.45 Ma).

Trace Elements vs Age

Plots of trace elements vs age can be divided into those that do or do not show variations with age.

Rb, Cs, Ta, Nb, Y, Th, and U (Figs. 21 and 22) all show increases in abundance (positive slopes) from 1.18-0.71 Ma and from 0.55-0.51 Ma. Decreases in abundances (breaks in the slopes) occur during the interval 0.71-0.55 Ma and with the final eruption at 0.45 Ma. Abundances may increase more than 2 fold from their base levels during the intervals 1.18-0.71 and 0.55-0.51 Ma.

Zr shows poorly defined variations with age (Fig. 23) compared to those seen in Figures 21 and 22. Overall, Zr shows the opposite pattern with a decrease in abundance (negative slope) from 1.18-0.91 Ma and then a relatively flat pattern from 0.91-0.71 Ma. There is an increase in abundance with the next eruption at 0.55 Ma. Abundance decreases from 0.55-0.51 Ma and then increases again with the youngest eruption at 0.45 Ma.

Plots of Sr and Ba vs age (Fig. 23) show variations very much like those seen for TiO_2, CaO, and P_2O_5 (Fig. 19). There is very little variation from 1.18-0.71 Ma

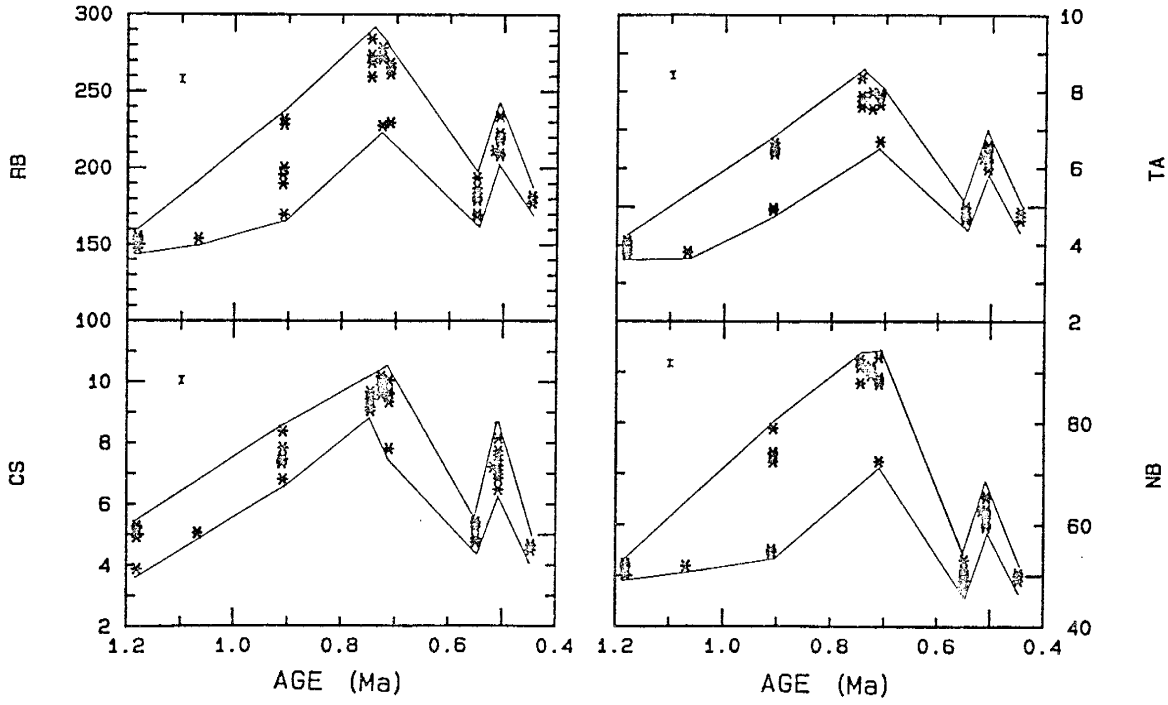

Figure 21. Plots of Rb, Cs, Ta, and Nb (in PPM) vs age. Error bars show analytical precision.

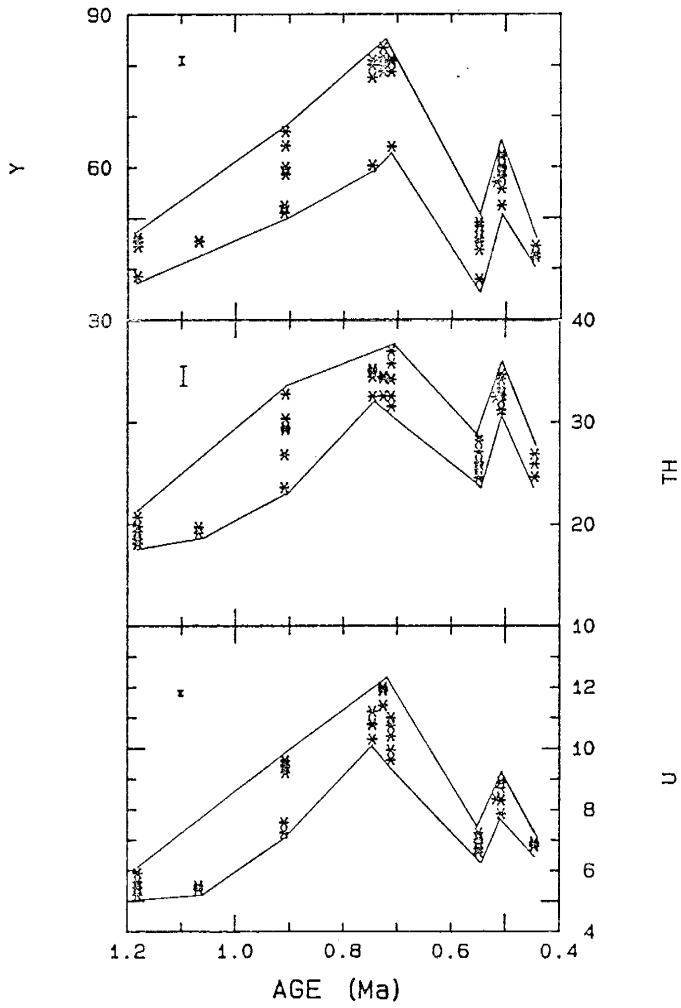

Figure 22. Plots of Y, Th, and U (in PPM) vs age. Error bars show analytical precision.

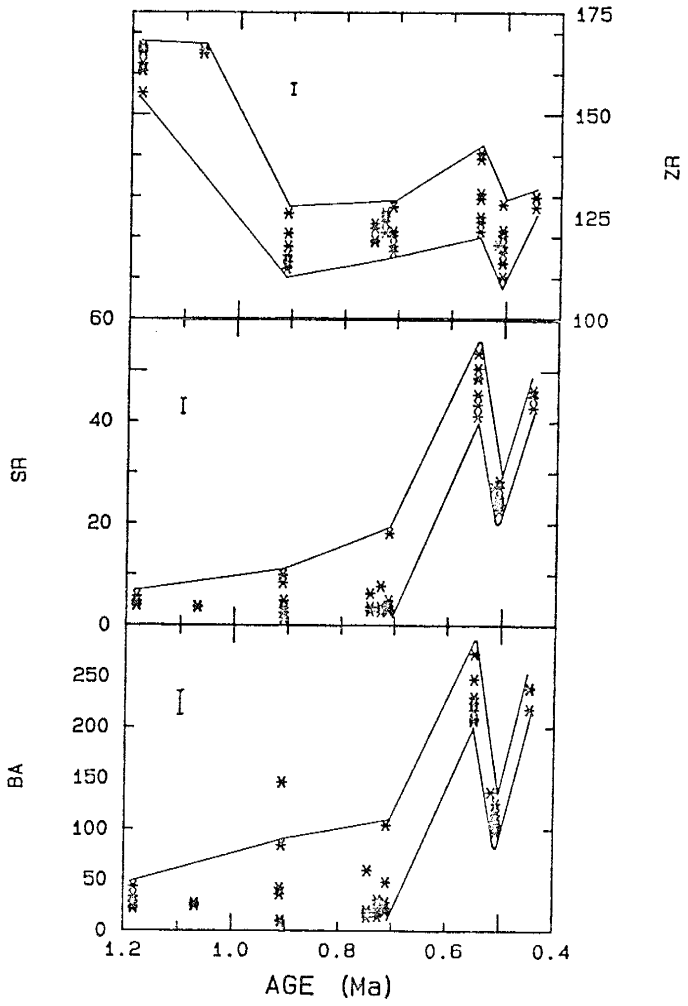

Figure 23. Plots of Zr, Sr, and Ba (in PPM) vs age. Error bars show analytical precision.

then a sharp increase in abundances with the next eruption at 0.55 Ma. There is a decrease in abundances from 0.55-0.51 Ma, and finally an increase with the last eruption at 0.45 Ma.

The light rare earth elements (LREE's), La and Ce, show decreasing abundances with time (negative slopes) and breaks in slopes (Fig. 24) similar to those decribed for Zr (Fig. 23) only much better defined. Nd and Sm (not plotted) show similar variations, but with much greater scatter, especially in the case of Sm. Plots of the heavy rare earth elements (HREE's) Yb and Lu vs age (Fig. 24) show well defined variations similar to those described for Rb, Cs, Ta, and Nb (Fig. 21). Tb (not plotted) displays exactly the same pattern as Yb and Lu. Eu (Fig. 25) shows variation with age almost exactly identical to that shown by La and Ce (Fig. 24).

Other trace elements not shown on these diagrams either show no well defined variations with age (Sc, As, Se, Mo, Sb, Hf, Pb) or have such large analytical uncertainties associated with them that they show a great deal of scatter (Cr, Zn, Br).

Co-Variation Diagrams

An examination of the diagrams just presented reveals that rhyolites of the Valle Grande Member naturally fall into three groups based on plots of elements versus age. Group 1 samples range in age from

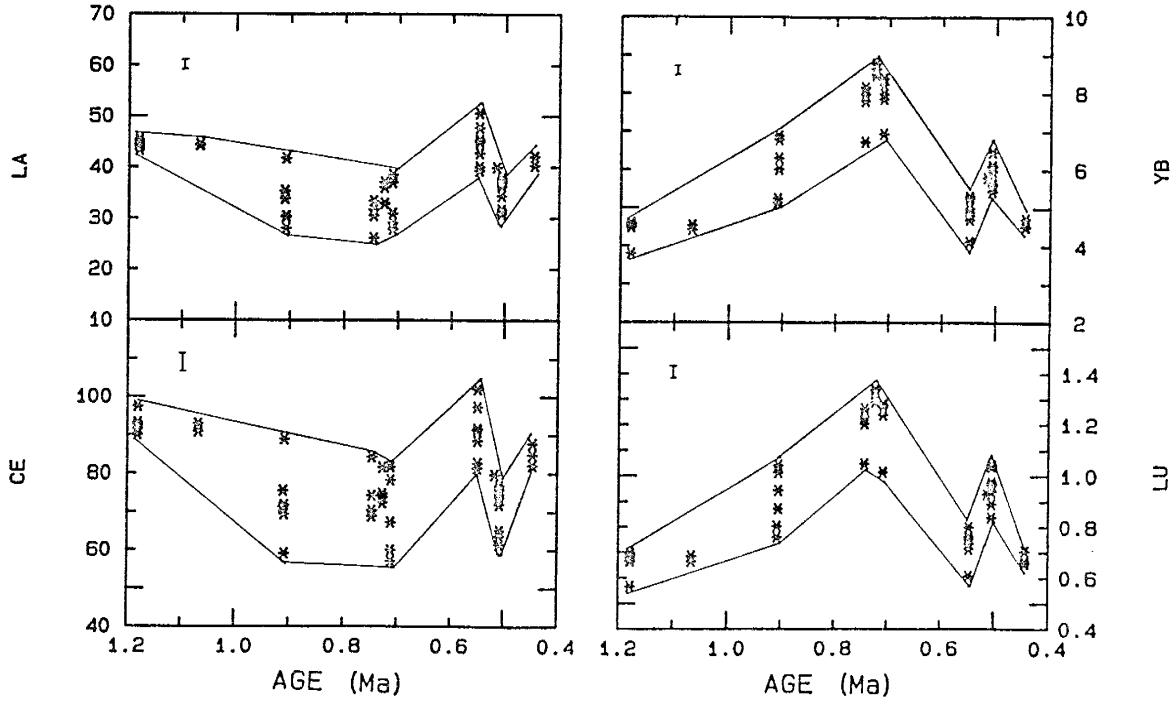

Figure 24. Plots of La, Ce, Yb, and Lu (in PPM) vs age. Error bars show analytical precision.

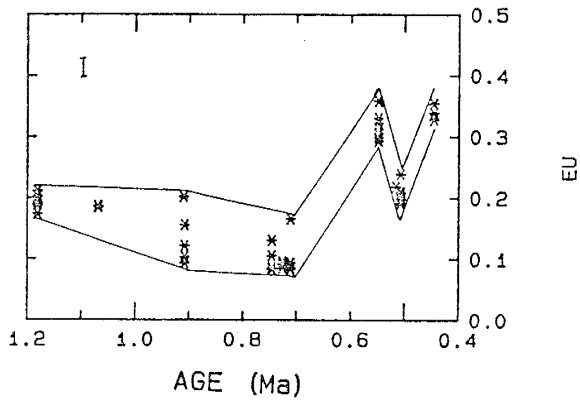

Figure 25. Plot of Eu (in PPM) vs age. Error bar shows analytical precision.

1.18-0.71 Ma, group 2 samples from 0.55-0.51 Ma, and group 3 samples plot at 0.45 Ma. Elements generally considered to be incompatible in most differentiation sequences (Rb, Cs, Ta, Nb, etc:) show increases with decreasing age in both group 1 and 2 samples, whereas elements considered to be compatible (TiO_2, P_2O_5, Sr, Ba, etc:) show decreases with decreasing age. Breaks in the trends thus defined occur between groups 1 and 2 and between groups 2 and 3. On the following co-variation diagrams these three groups of samples are plotted as three separate symbols. Although group 3 samples are plotted on the following diagrams they are not discussed in any detail since they represent only one point in time and are not part of a sequence of eruptions as rocks from groups 1 and 2.

Major Elements vs SiO_2

Most major elements show some correlation with SiO_2. Plots of Al_2O_3, Fe_2O_3, CaO, and K_2O vs SiO_2 (Fig. 26) show the best correlations, with Al_2O_3 showing the most well defined trend. All four oxides decrease in abundance with increasing SiO_2. Group 2 samples range to higher values of Al_2O_3, Fe_2O_3, CaO, and K_2O but lower values of SiO_2.

P_2O_5, TiO_2, and MgO also decrease with increasing SiO_2 (Fig. 27), however the trends are scattered. Group 2 samples range to higher values of P_2O_5, TiO_2, and MgO,

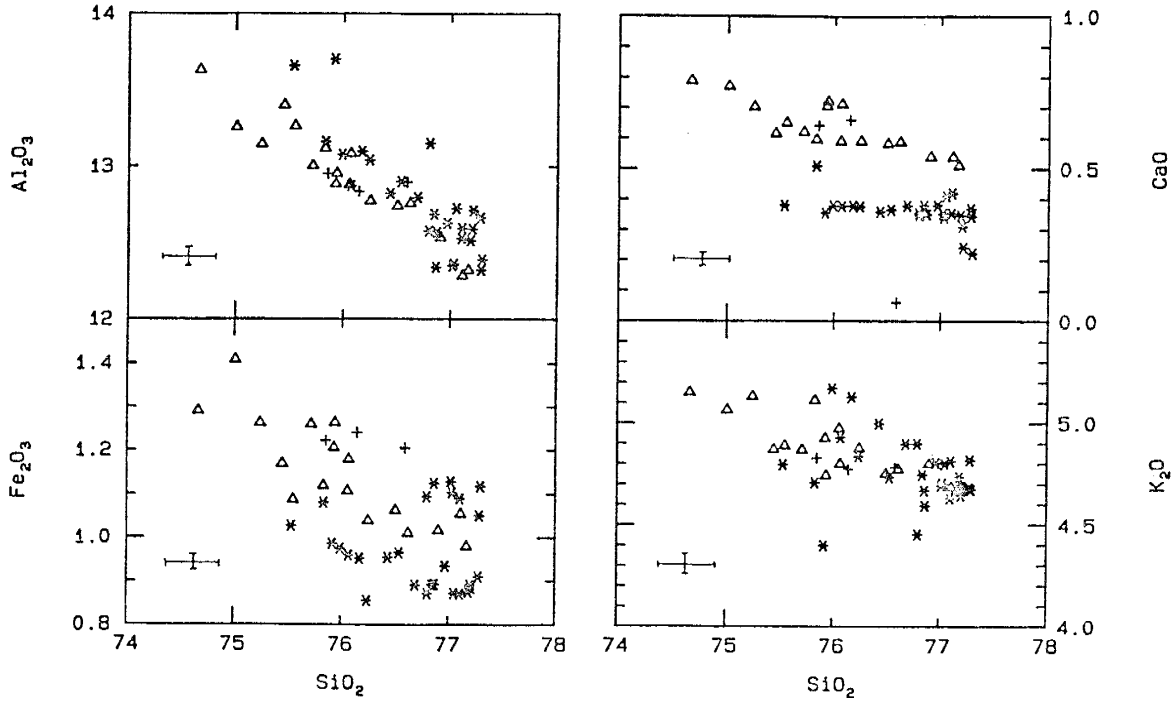

Figure 26. Plots of Al_2O_3, Fe_2O_3, CaO, and K_2O vs SiO_2. All oxides recalculated to 100% anhydrous and expressed as wt.%. Error bars show analytical precision.
Stars = group 1 samples.
Triangles = group 2 samples.
Pluses = group 3 samples.

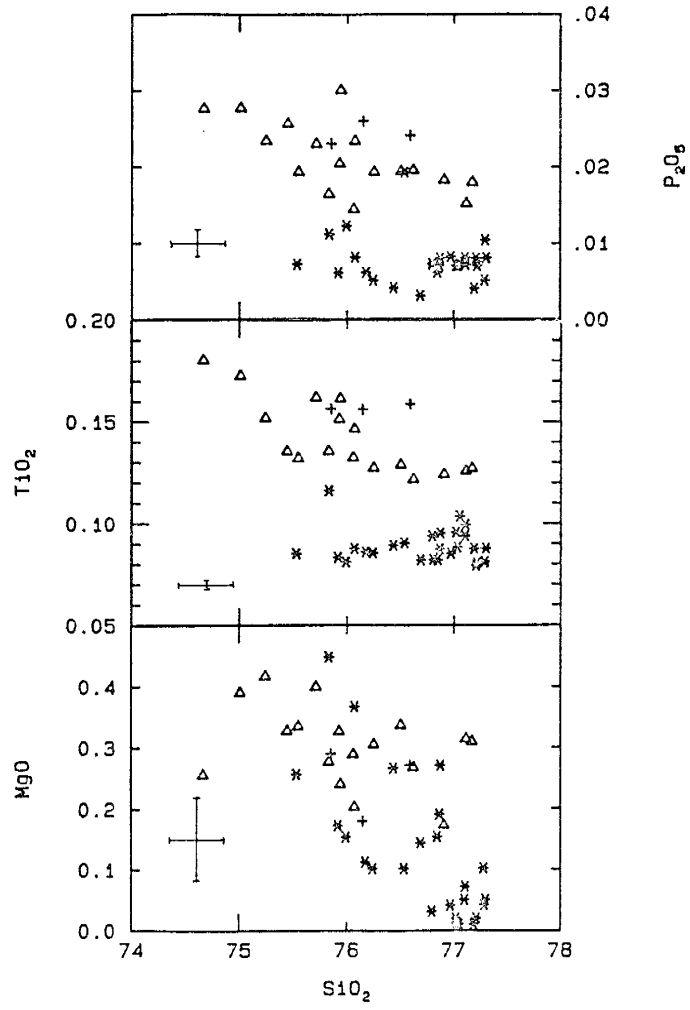

Figure 27. Plots of P_2O_5, TiO_2, and MgO vs SiO_2. All oxides recalculated to 100% anhydrous and expressed in wt.%. Error bars show analytical precision. Symbols as in Figure 26.

but lower values of SiO_2.

Na_2O and MnO show no correlation with SiO_2 (Fig. 28). Group 1 samples show higher values of Na_2O and MnO whereas group 2 samples have lower values of SiO_2.

Major Elements vs Nb

Nb is used as an index of differentiation since it increases more than two fold through the Valle Grande Member eruptive sequence. Plots of major elements vs Nb can be divided into those that increase, decrease, or show no change with increasing Nb.

SiO_2, Al_2O_3, Na_2O, and K_2O show no variation with increasing Nb (Fig. 29) with the exception of a small increase in SiO_2 for Group 2 samples.

On plots of TiO_2, CaO, Fe_2O_3, and P_2O_5 vs Nb (Fig. 30) group 1 samples show no variation with increasing Nb with the exception of Fe_2O_3 which has a slight negative correlation. In group 2 all four oxides decrease with increasing Nb abundance.

MnO behaves incompatibly in both groups 1 and 2 and correlates positively with increasing Nb (Fig. 31). MgO shows no systematic variation (Fig. 31) due to scatter in the data, which is due to the large analytical error associated with magnesium (see Appendix G).

Trace Elements vs Nb

Plots of trace elements vs Nb can be divided into

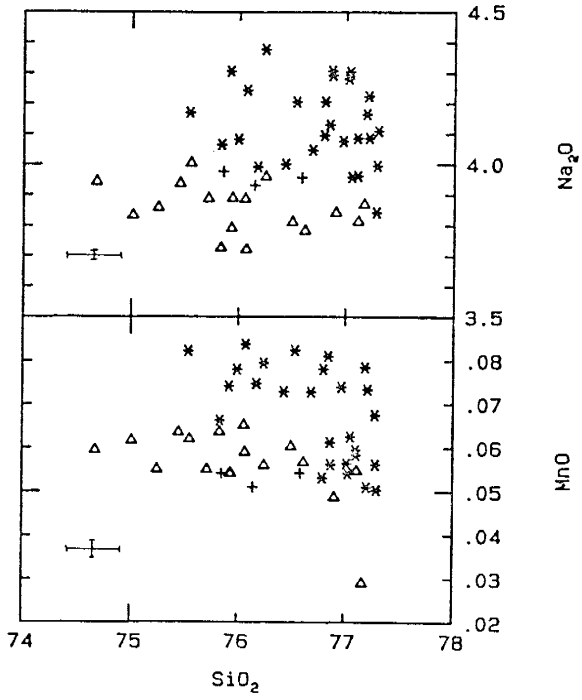

Figure 28. Plots of Na_2O and MnO vs SiO_2. All oxides recalculated to 100% anhydrous and expressed in wt.%. Error bars show analytical precision. Symbols as in Figure 26.

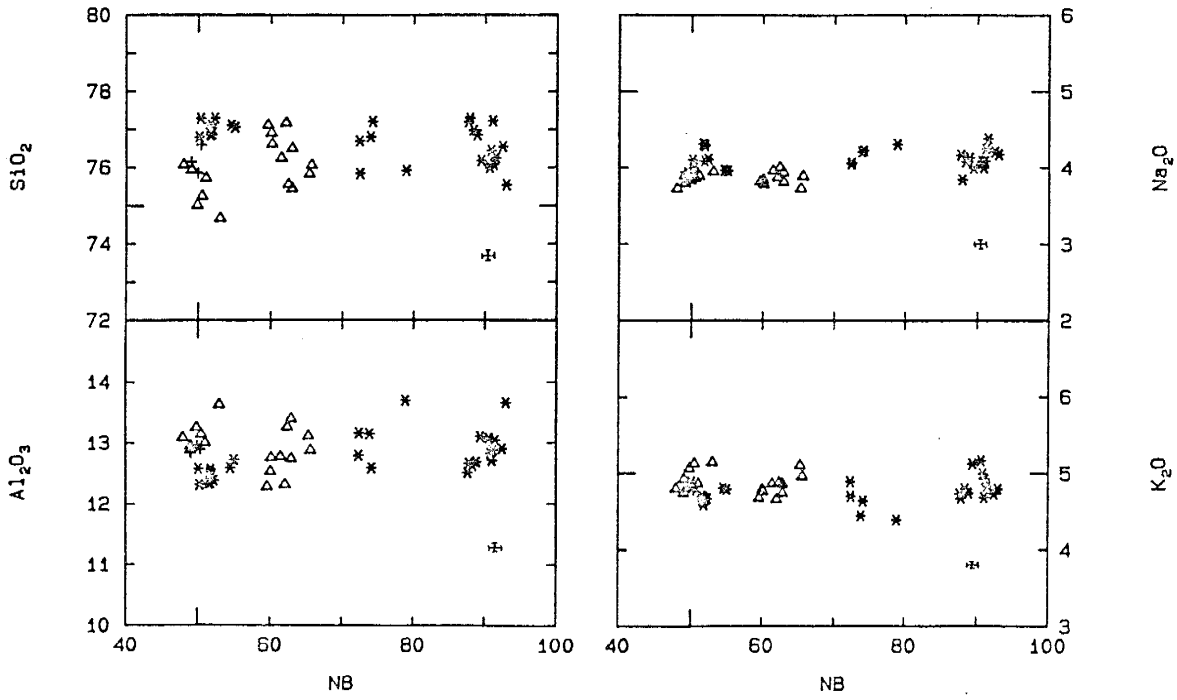

Figure 29. Plots of SiO_2, Al_2O_3, Na_2O, and K_2O (in wt.%) vs Nb (in PPM). Error bars show analytical precision. Symbols as in Figure 26.

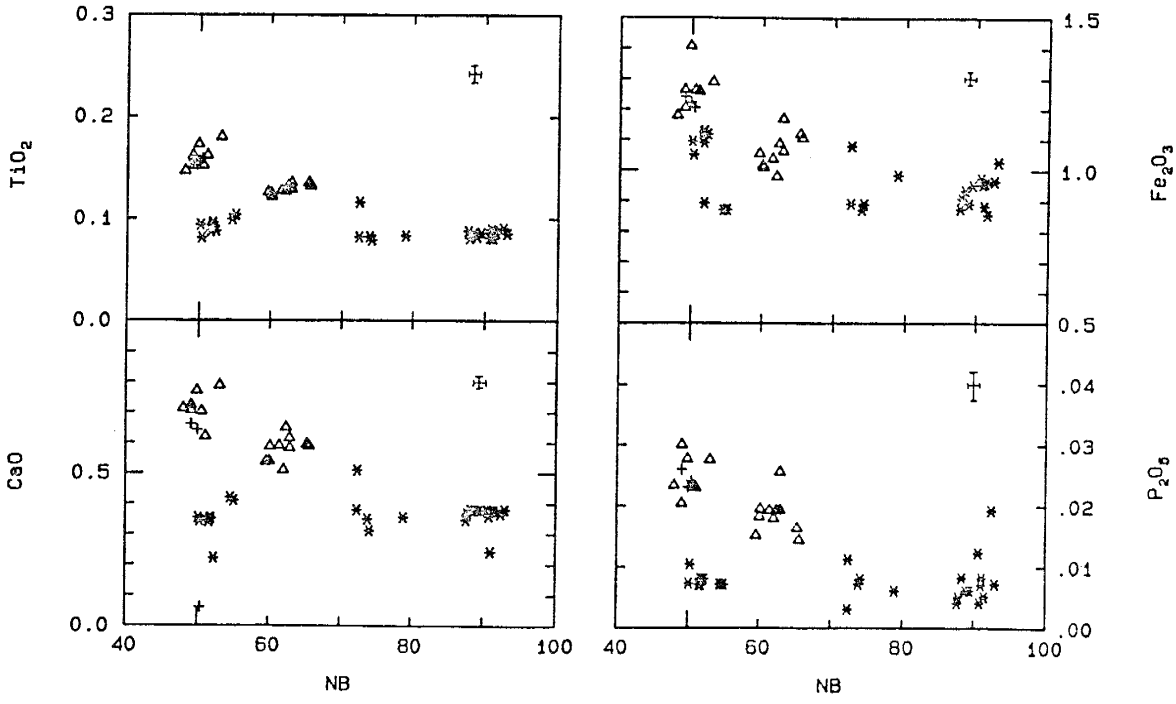

Figure 30. Plots of TiO_2, CaO, Fe_2O_3, and P_2O_5 (in wt.%) vs Nb (in PPM). Error bars show analytical precision. Symbols as in Figure 26.

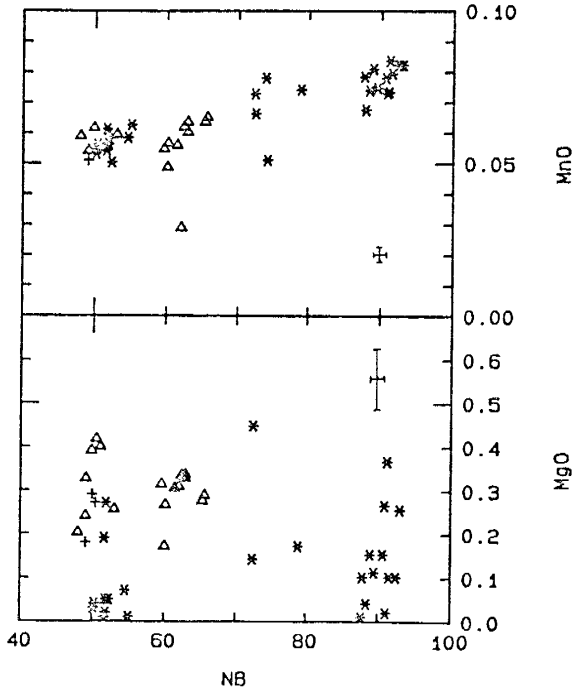

Figure 31. Plots of MnO and MgO (in wt.%) vs Nb (in PPM). Error bars show analytical precision. Symbols as in Figure 26.

three general groups; those that increase with increasing Nb, those that decrease with increasing Nb, and those that show no definite variation.

Plots of Rb, Cs, Y, and Ta vs Nb (Fig. 32) all show well defined positive correlations although there are a few samples which fall off of the main trend for the Rb, Cs, and Y plots. Groups 1 and 2 show roughly coincident trends on all plots except for the Rb vs Nb plot on which the trend defined by group 2 falls above the trend defined by group 1. Plots of U and Th vs Nb (Fig. 33) show the same positive correlation as those shown in Figure 32. On the plot of Th vs Nb group 2 samples are displaced above the trend defined by group 1 samples.

Mo, Sb, and Pb all show a positive correlation with Nb (Fig. 34). The trend defined on the Sb vs Nb plot is much better constrained than the other two which show a great deal of scatter.

On a plot of Hf vs Nb (Fig. 35) there is no correlation observable except that group 1 samples are displaced to higher Hf values than group 2 samples.

Plots of Sc, Sr, and Ba vs Nb (Fig. 35) all show similar patterns. Group 1 samples define a trend of increasing Nb with no change in abundance of the other element whereas group 2 samples show a negative correlation with Nb. Cr, Zn, As, Se, and Br show no correlation with Nb.

La, Ce, Nd, and Eu show negative correlations with

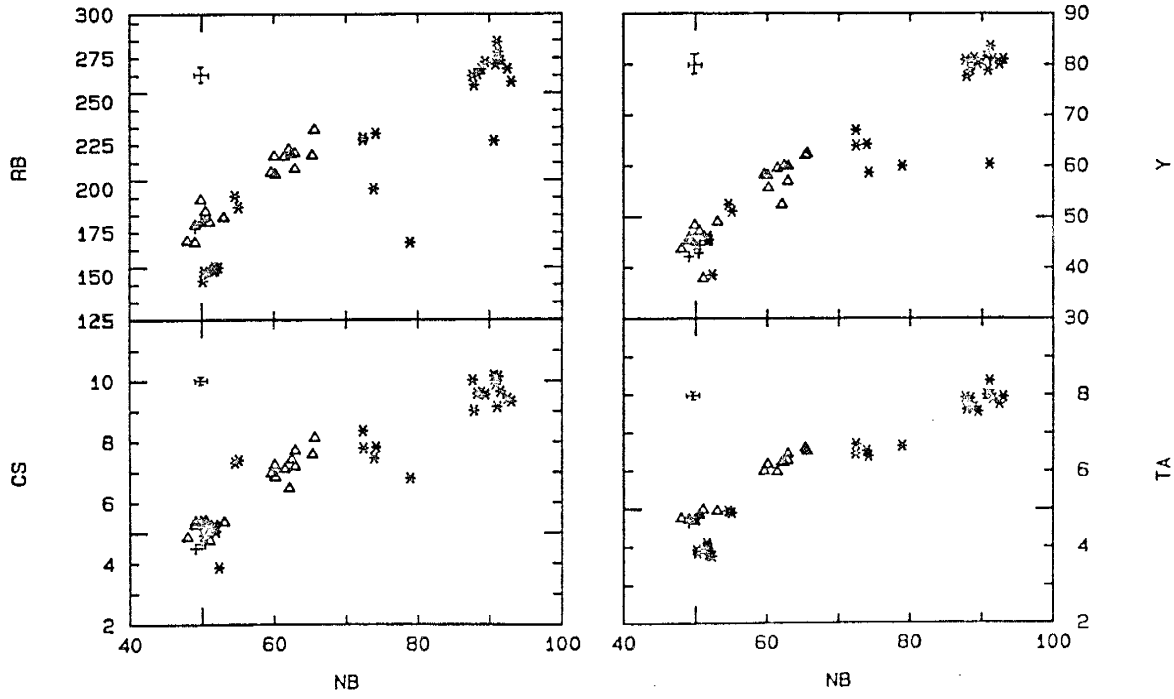

Figure 32. Plots of Rb, Cs, Y, and Ta vs Nb (all in PPM). Error bars show analytical precision. Symbols as in Figure 26.

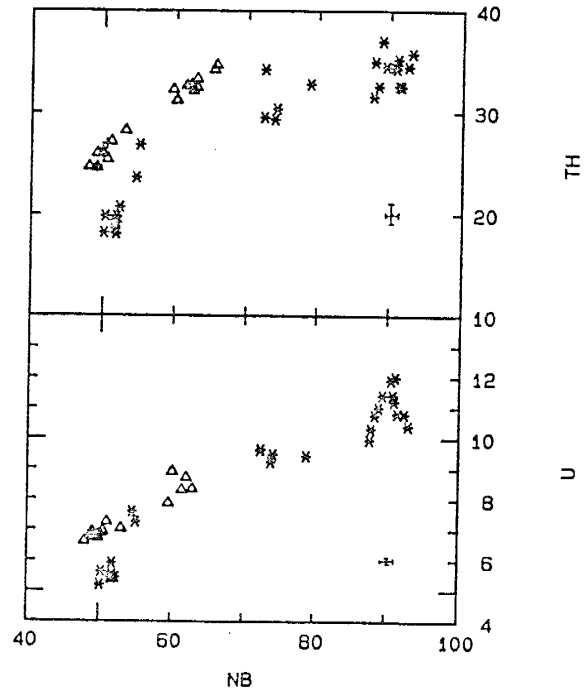

Figure 33. Plots of Th and U vs Nb (all in PPM). Error bars show analytical precision. Symbols as in Figure 26.

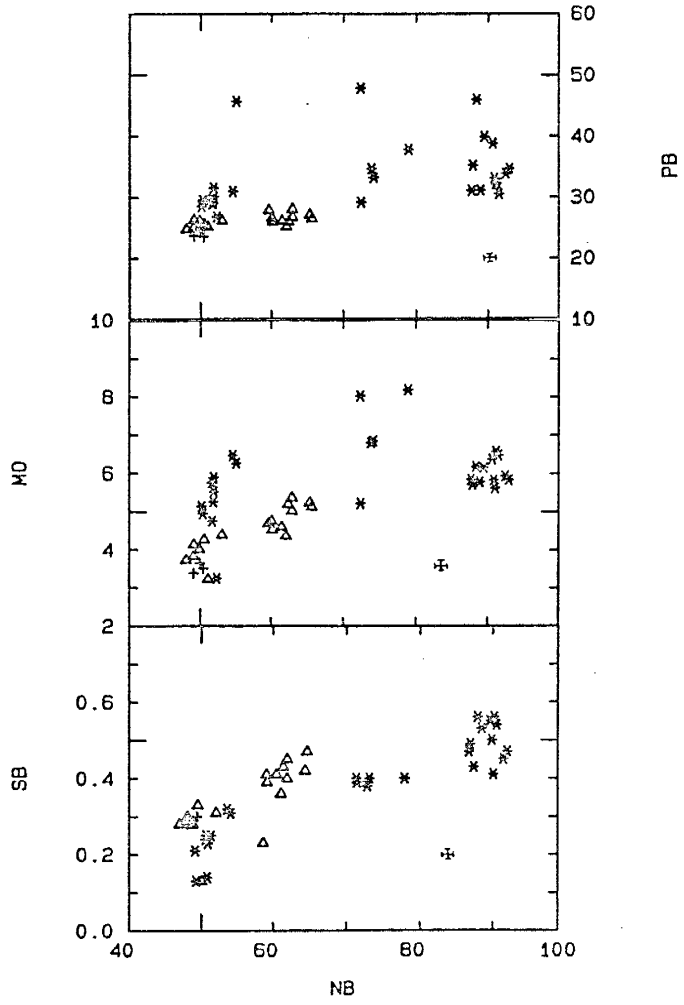

Figure 34. Plots of Mo, Sb, and Pb vs Nb (all in PPM). Error bars show analytical precision. Symbols as in Figure 26.

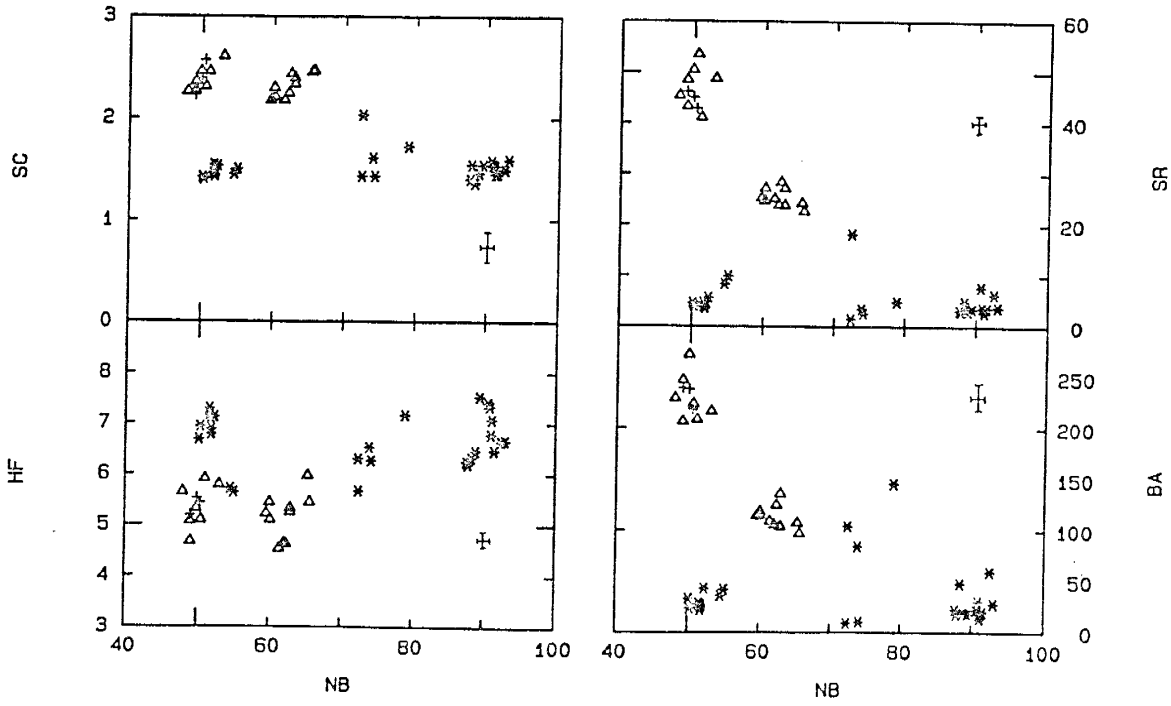

Figure 35. Plots of Sc, Hf, Sr, and Ba vs Nb (all in PPM). Error bars show analytical precision. Symbols as in Figure 26.

increasing Nb (Fig. 36 and 37), with group 2 samples showing a much greater overall decrease than group 1 samples. For Sm group 1 samples have a positive correlation with Nb whereas group 2 samples show no correlation.

Plots of Tb, Yb and Lu vs Nb (Fig. 37) all show a similar well defined positive correlation. Generally group 1 and 2 trends overlap.

REE/Chondrite Diagrams

Chondrite normalized REE plots also show differences between group 1 and 2 samples as well as trends with time within each group. Samples from group 1 (1.18-0.71 Ma) show deep negative Eu anomalies, enriched LREE's, and relatively flat HREE patterns (Fig. 38). With decreasing age there is a general trend of decreasing LREE's, increasing Eu anomaly, and increasing HREE's. La/Yb varies from 10 to 3.5, Ce/Sm varies from 13 to 9, and Eu/Eu* varies from 0.08 to 0.03 going from oldest to youngest. REE plots for group 2 (0.55-0.51 Ma) (Fig. 39) show the same general features as those for group 1. La/Yb varies from 10 to 5, Ce/Sm varies from 15 to 10.5, and Eu/Eu* varies from 0.15 to 0.09 going from oldest to youngest. REE plots for group 3 samples (not shown) are virtually identical to the plot shown in Fig. 38 for sample SA-3.

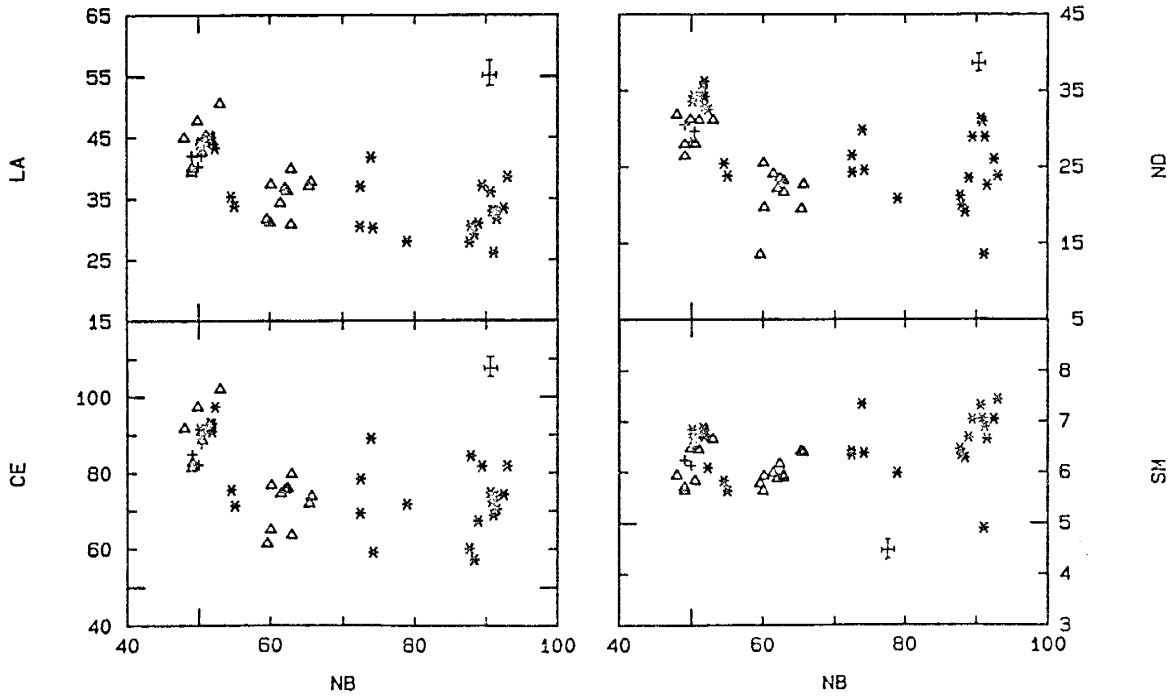

Figure 36. Plots of La, Ce, Nd, and Sm vs Nb (all in PPM). Error bars show analytical precision. Symbols as in Figure 26.

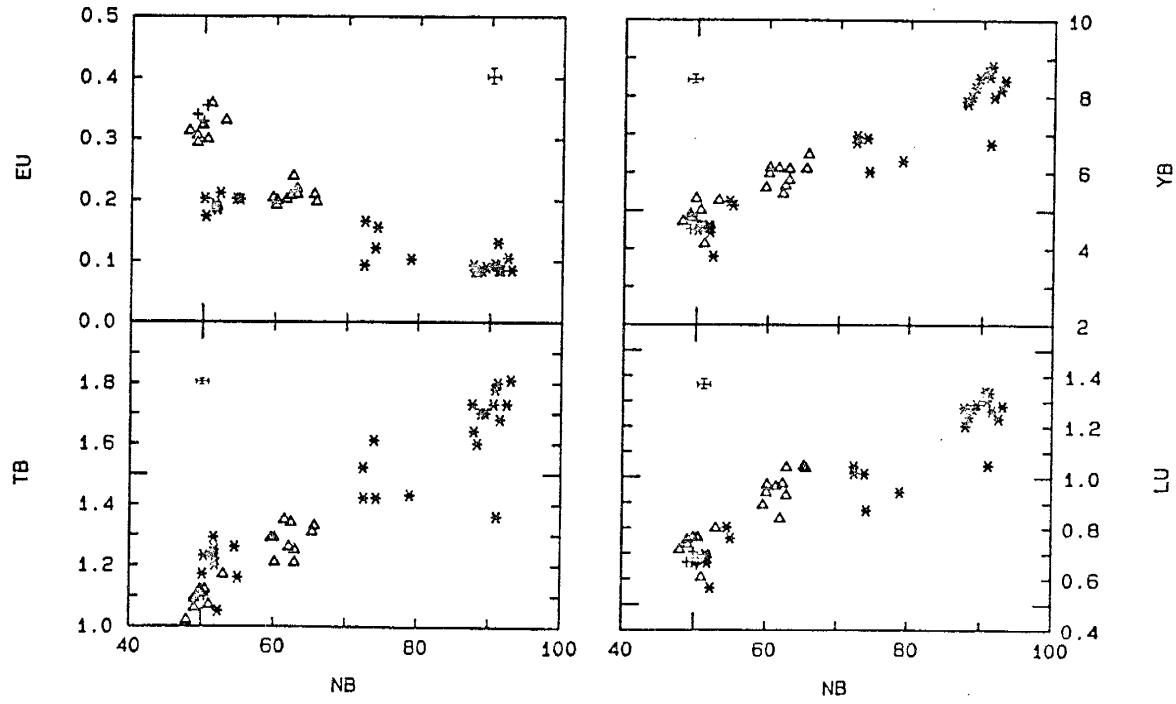

Figure 37. Plots of Eu, Tb, Yb, and Lu vs Nb (all in PPM). Error bars show analytical precision. Symbols as in Figure 26.

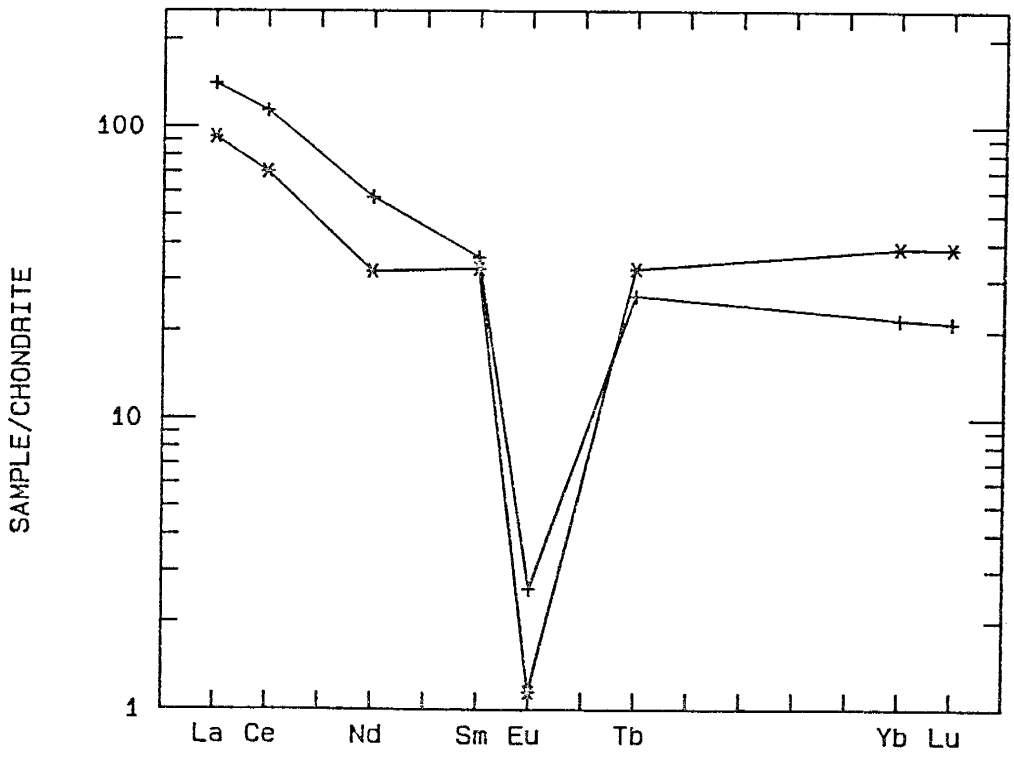

Figure 38. Representative REE/Chondrite plots for group 1 samples selected to bracket the range seen. Normalizing values are those of the Leedy chondrite divided by 1.20 (Taylor and Gorton, 1977). Pluses = sample DM-0 (1.18 Ma), Stars = sample SL-5 (0.71 Ma).

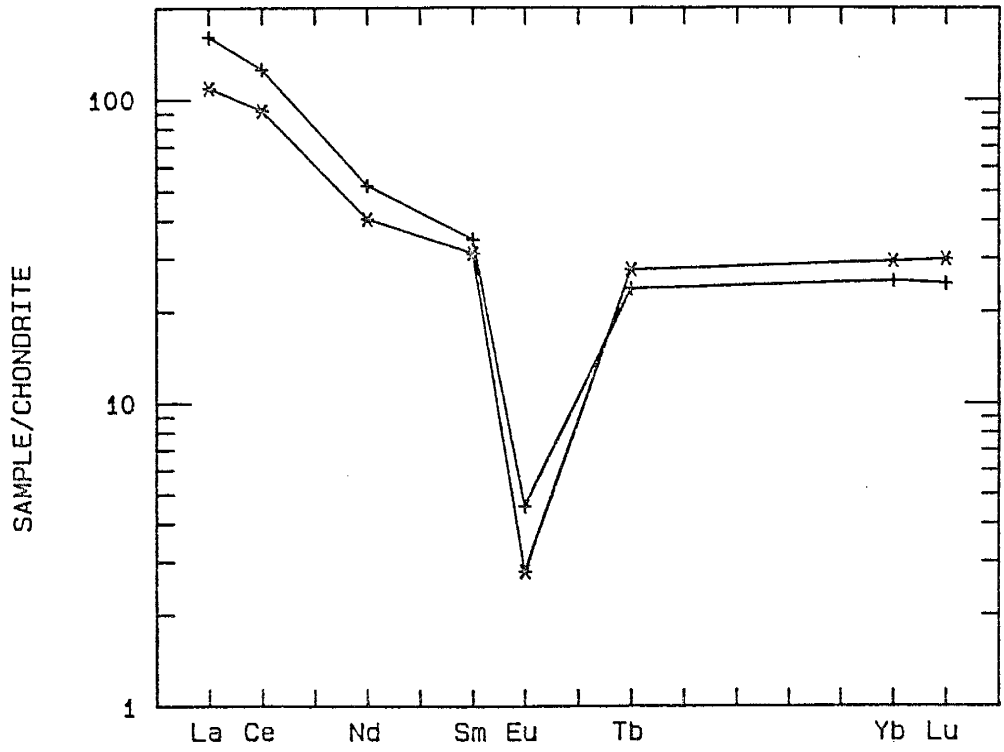

Figure 39. Representative REE/Chondrite plots for group 2 samples selected to bracket the range seen. Normalizing values are those of the Leedy chondrite divided by 1.20 (Taylor and Gorton, 1977). Pluses = sample SA-3 (0.55 Ma), Stars = sample SM-2 (0.51 Ma).

Summary

Rhyolites of the Valle Grande Member can be divided into three groups based upon geochemistry. As will be shown later in the Discussion, the samples making up groups 1 and 2 seem to define two separate and coherent differentiation trends with group 3 samples appearing to represent magmas unrelated to any of these earlier eruptives. For ease of discussion group 1 samples are here defined as comprising trend 1 (1.18-0.71 Ma) whereas group 2 samples are defined as comprising trend 2 (0.55-0.51 Ma). The breaks in these trends occurring at 0.71-0.55 and 0.51-0.45 Ma are refered to as reversals 1 and 2 respectively.

DISCUSSION

Introduction

In this section interpretations of the geochemical data presented under Whole Rock Chemistry are given. The Valle Grande Member of the Valles Rhyolite Formation is the focus of this (and previous) sections. There are several reasons for using the Valle Grande Member rhyolites as a monitor of the evolution of the post-Bandelier Tuff magma system. Post-Bandelier Tuff eruptives span an age range from ~1.18 Ma to ~0.13 Ma (Doell et al., 1968; Goff et al., 1986). Rhyolites of the Valle Grande Member range in age from ~1.18 to ~0.45 Ma (Table 1) and thus represent approximately 70% of the period of post-Bandelier Tuff volcanism. Of the 13 age dates (Table 1) obtained on the Valles Rhyolite Formation 11 were done on rhyolites of the Valle Grande Member and thus it is well constrained chronologically. There have been at least 20 discrete rhyolitic eruptions in the Valles Caldera since the eruption of the Upper Bandelier Tuff. The Valle Grande Member rhyolites account for 14 of these eruptions. Finally, Valle Grande Member rhyolites dominate the post-Bandelier Tuff eruptives volumetrically. Thus the following interpretations and mechanisms proposed for the evolution of the post-Bandelier Tuff magma system are based strictly on the geochemistry of rhyolites of the Valle Grande Member.

Some preliminary interpretations of the relationship of the Valle Grande Member rhyolites to older and younger members of the Valles Rhyolite Formation based on available geochemical analyses will be given towards the end of this section.

Trends and reversals in trends as defined in the previous section, Whole Rock Chemistry, are treated separately in this section. This is because separate and totally different mechanisms are required to explain these changes in chemistry with age. Thus trends 1 and 2 are referred to under Differentiation Trends whereas reversals 1 and 2 are discussed under Reversals in Trends.

Alteration

Many studies have been undertaken to assess the effect of hydration and devitrification on the major and trace element abundances of rhyolitic obsidians (Lipman, 1965; Ewart, 1971; Kochnar, 1977; Zielinski et al., 1977; Jezek and Noble, 1978). The samples collected for this study show a wide variation in hydration with total LOI's ranging from 0.17 to 3.74 wt.% (see Appendix F). In addition a few samples were observed to have undergone varying amounts of devitrification. Thus it is necessary to examine the possibility that the chemistry of the samples may have been variably altered by addition or removal of elements during such secondary processes.

Of the major elements those which are the most affected by hydration are Na_2O and K_2O. Increasing hydration causes progressive loss of sodium and gain of potassium (Kochnar, 1977; Jezek and Noble, 1978). Some studies have indicated that highly porous vitric rocks such as tuffs may lose as much as 3 wt.% Na_2O (Kochnar, 1977) although most studies suggest considerably smaller losses (Jezek and Noble, 1978). Another major element affected during hydration is iron which tends to undergo oxidation (Zielinski et al., 1977).

Several studies have been undertaken to determine the effects of devitrification on major elements (Lipman, 1965; Ewart, 1971). Results published by Lipman (1965) suggest that Na_2O is lost and K_2O is gained during this process. Ewart (1971) suggests that the growth of spherulites decreases the Na_2O/K_2O ratio of the remaining glass, but that the whole rock composition is unchanged.

Trace elements which may be affected by hydration include Li, F, Sr, Ba, and U (Zielinski et al., 1977). Of these the ones of interest in this study are Sr and Ba since they important in petrogenetic modelling. Samples collected for this study were not analyzed for Li and F. Generally U shows depletions whereas Sr and Ba show enrichments with increasing hydration (Zielinski et al., 1977).

Unfortunately the trace element study by Zielinski et al. (1977) dealt with the effects of primary

crystallization and not secondary crystallization (spherulitic devitrification) and thus their results are not applicable to this study.

The data set for the samples in this study was examined with these possible alteration effects in mind.

The effects of hydration were relatively easy to assess since, by chance, a sample of relatively unhydrated obsidian (DM-0 - 0.46 wt.% LOI) and co-existing hydrated pumiceous rhyolite (DM-1 - 3.50 wt.% LOI) were collected from the same flow lobe approximately 50 meters apart. If these samples are assumed to have had the same original magmatic composition then any changes in major or trace element chemistry can probably be attributed to the difference in hydration between the two. Major elements for these two samples (calculated anhydrous) are identical within analytical error except for MgO, Na_2O, and K_2O. The difference in MgO can probably be attributed to the fact that this oxide is close to detection limits for XRF and thus has poor analytical precision (see Appendix G). Na_2O and K_2O show the expected changes with hydration. Na_2O decreases by 0.21 wt.% whereas K_2O increases by 0.23 wt.%. These values are well above analytical uncertainty and thus represent real differences. Other samples from the same dome or flow lobe show the same general decreases in Na_2O and increases in K_2O with increasing hydration. Examination of the trace element abundances for this pair

of samples (and several other pairs of relatively unhydrated and hydrated samples) show no systematic variations with degree of hydration.

A few pairs of samples collected near each other which represent hydrated and devitrified examples of presumably identical original composition show no systematic variations in either major or trace element abundances.

Thus, it appears that, with the exception of small changes in Na_2O and K_2O abundances, the effects of hydration and devitrification have not chemically altered the samples used in this study to any appreciable extent. The lack of alteration observed is most likely due to the relatively young age of these rocks compared to those used in the studies mentioned above, most of which range in age from 10-30 Ma.

Normative Compositions

Due to the relatively constant major element composition of these rhyolites, normative mineralogies plot in a very restricted area on the Q-Ab-Or diagram (Fig. 40). All samples plot in a tightly clustered group between the minimas for 1 and 2 kb total P_{H_2O} (assuming $P_{H_2O} = P_{Total}$).

Crystallization at a minima or eutectic would be consistent with the relatively fixed major element abundances but widely varying trace element abundances

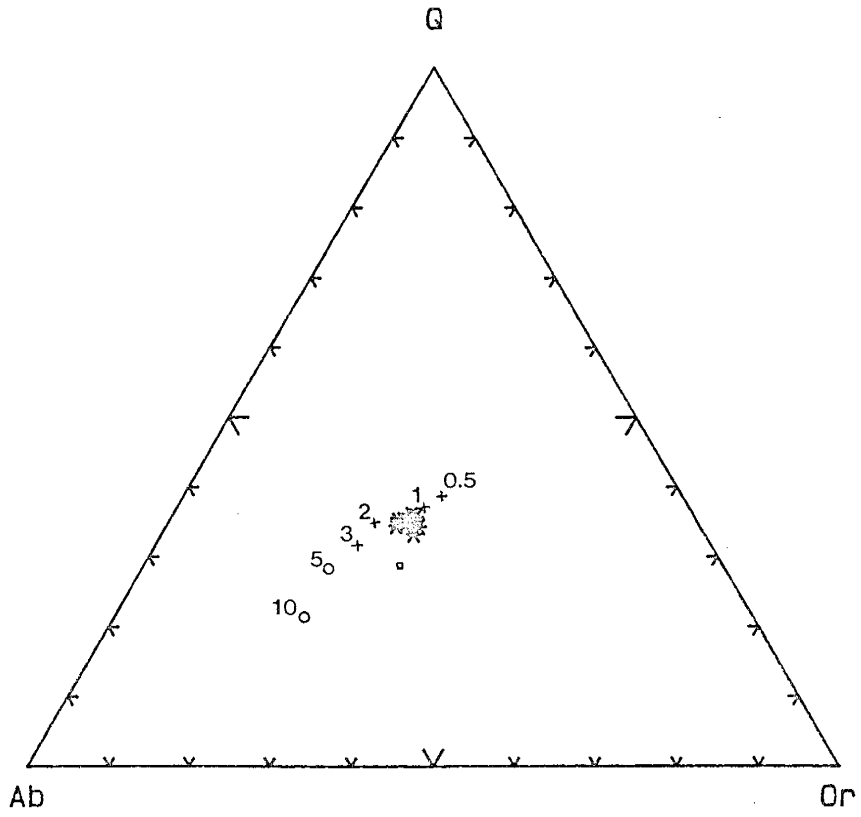

Figure 40. Q-Ab-Or ternary diagram for Valle Grande Member rhyolites. Pluses = minima, open circles = eutectics, square = minimum for system with 1 wt.% fluorine. All pressures in kb (from Tuttle and Bowen, 1958; Luth et al., 1964; Manning, 1981).

seen in these rhyolites. Once a crystallizing melt has reached the minimum (or thermal low) in the system the composition of the major crystallizing phases (in this case quartz, sanidine, and plagioclase) will be very near, or identical, to that of the remaining melt and thus the major element composition of the system will be fixed. Trace element abundances, however, will be controlled by their compatibility or incompatibility with minor crystallizing phases such as zircon, allanite, and apatite and would thus be expected to vary greatly during continued crystallization.

If it is assumed that $P_{H_2O} = P_{Total}$ then Figure 40 suggests that these magmas last equilibrated at a depth corresponding to 1-2 kb pressure (2.5-7.5 km) immediately prior to eruption. This is supported by several lines of evidence. Estimates from the hornblende geobarometer (Table 4) indicate that the phenocryst assemblage in units with hornblende analyzed had equilibrated at a pressure of <2 kb (<7.5 km) prior to eruption. Pressures calculated by the ternary feldspar thermobarometer (Table 3) do not conflict with this interpretation within the limits of errors calculated (with the one exception of SA-1). As previously mentioned (see Geothermometry-Geobarometry) the hornblende geobarometer is considered to be the more reliable of the two. Finally, temperatures calculated by the feldspar thermobarometer (Table 3) average 755 °C for these rhyolites. With increasing P_{H_2O}

in the Q-Ab-Or system the minimum shifts toward the Ab apex and temperatures at the minimas or eutectics decrease (Tuttle and Bowen, 1958; Luth et al., 1964). Minimum temperatures for 1 and 2 kb pressure are 730 and 690 °C respectively (Tuttle and Bowen, 1958). At a P_{H_2O} of 10 kb the minimum temperature is depressed to 625 °C (Luth et al., 1964). Thus, the temperatures calculated for these magmas correspond more closely to the experimentally determined temperatures for the minimum in the granitic system at pressures of ~1 kb than at greater pressures.

The high fluorine contents of biotites and amphiboles analyzed in this study (Appendix E) raises the possibility that the f_{HF}/f_{H_2O} of these magmas may have been high enough to have had some effect on their crystallization behavior. Topaz rhyolites of the western United States, which may contain several wt.% fluorine, typically have up to 5 wt.% fluorine in their biotites (Christiansen et al., 1986). Although none of the rhyolites of the Valle Grande Member have been analyzed for fluorine the fact that biotites found in them may contain up to ~3.9 wt.% fluorine may indicate that they have significant concentrations of this volatile. Studies by Manning (1981) have indicated that even small amounts of fluorine in granitic melts can have significant effects on phase relationships and liquidus temperatures. Generally the addition of fluorine has the effect of

lowering the minimum temperature and displacing the miniumum away from the trend for the fluorine free system and towards the Or apex (Manning, 1981). Normative compositions for the Valle Grande Member rhyolites are displaced slightly off the trend for the fluorine free system and towards the minimum for the system with 1 wt.% fluorine (Fig. 40). This could be interpreted as being the effect of small (<0.5 wt.%) amounts of fluorine in these rhyolites although confirmation of this idea would require analyses for fluorine in unhydrated obsidian samples.

Differentiation Trends

This section deals with mechanisms or processes which could explain the elemental enrichments and depletions referred to in Whole Rock Chemistry as trends 1 and 2. Although the reader may be referred to diagrams in that section, the data are recast here in a more easily visualized form (Figs. 41, 42). In these diagrams the abundances of elements in the more evolved dome (youngest) is divided by the abundances of elements in the least evolved dome (oldest) for each trend. Thus, elements which are enriched with time have values >1 whereas those which are depleted with time have values <1 The magnitude of the enrichments or depletions are proportional to the variance from 1.

Mechanisms which have been considered or tested to

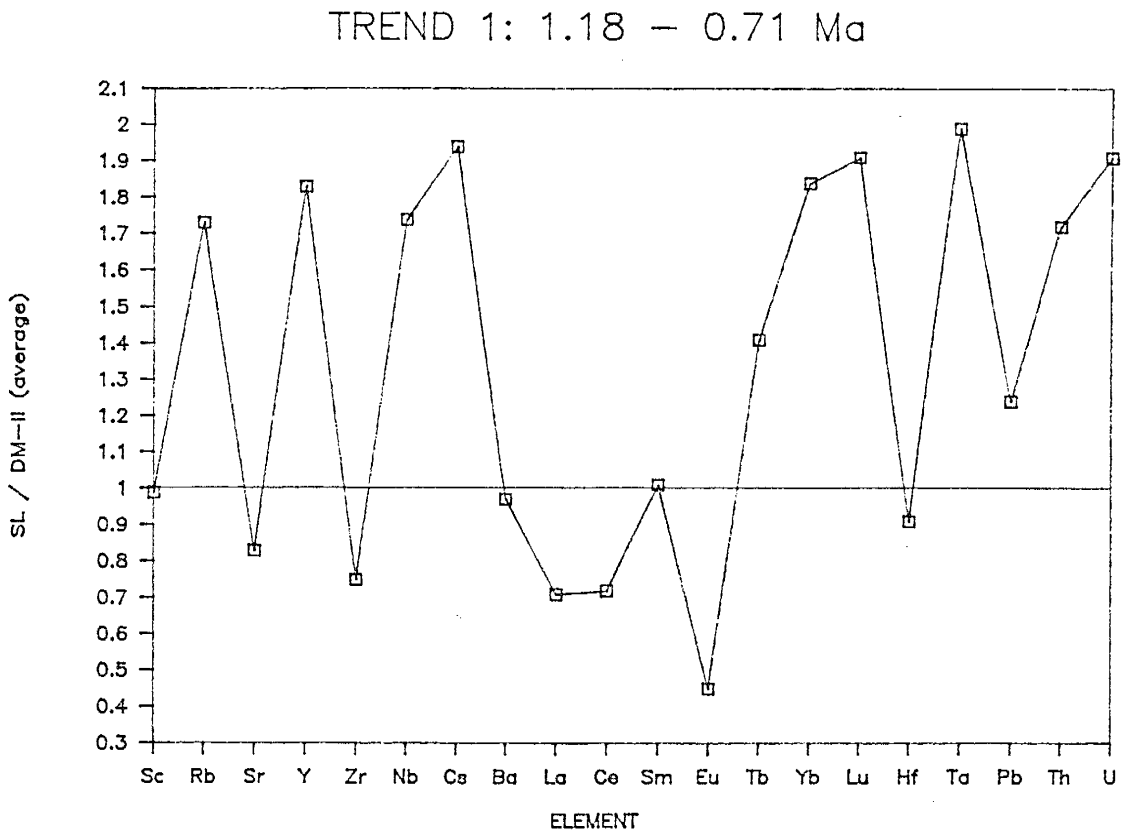

Figure 41. Enrichment/depletion diagram for trend 1. Numbers on y-axis obtained by dividing average composition of San Luis samples (most evolved) by average composition of Del Medio II samples (least evolved). Elements listed in order of increasing atomic number.

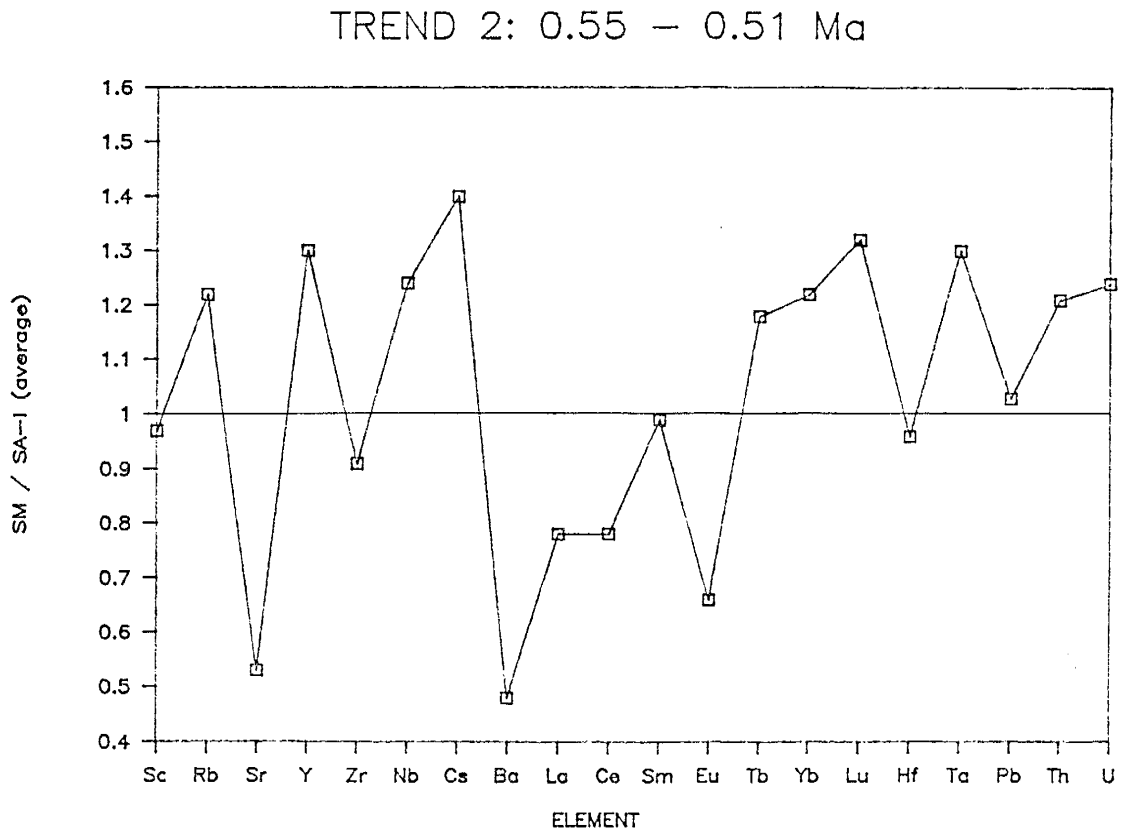

Figure 42. Enrichment/depletion diagram for trend 2. Numbers on Y-axis obtained by dividing average composition of South Mountain samples (most evolved) by average composition of San Antonio I samples (least evolved). Elements listed in order of increasing atomic number.

account for the differentiation trends seen in the Valle Grande Member rhyolites include silicate liquid immiscibility, volatile complexing, Soret (thermal) diffusion, progressive partial melting of a source area, country rock contamination, and crystal-liquid fractionation.

Silicate Liquid Immiscibility

Probably the least likely mechanism to have produced the geochemical trends seen in these rhyolites is silicate liquid immiscibility. This process cannot have produced the progressive enrichments and depletions seen by separation of a more silicic rhyolite from a more mafic rhyolite for several reasons. A review of the literature on natural occurances of silicate liquid immiscibility by Roedder (1979) shows no known cases of felsic liquids separating from felsic liquids, only cases of felsic liquids separating from mafic liquids are reported. Experimental evidence shows the same results in that miscibility gaps are only seen between mafic and felsic melts (Watson, 1976; Ryerson and Hess, 1978). Even if immiscibility did occur between felsic melts there would remain the difficulty of separating two liquids of approximately equal density.

If these rhyolites were formed as immiscible liquids from a basaltic source represented by any of the basalts erupted in the Jemez Mountains then experimental work on

trace element distribution between mafic and felsic liquids (Watson, 1976; Ryerson and Hess, 1978) indicates that the trace element composition of the rhyolites thus formed would not resemble those seen. The most obvious problem is that REE abundances of the Valle Grande Member rhyolites are equal to or greater than the REE abundances seen in basalts of the Jemez Mountains (Gardner et al., 1986) whereas experimental data indicates strong partitioning of the REE into the more mafic liquid.

Volatile Complexing

Complexing of trace elements with halogens in a roofward migrating volatile phase is a process that presumably could produce or influence the differentiation trends seen. The transport of trace elements as halogen complexes in a volatile phase is considered important in the differentiation of many rhyolitic magmas (Hildreth, 1979, 1981; Mahood, 1981; Taylor et al., 1981; Christiansen et al., 1983, 1984). These rhyolite compositions span a range from peralkaline to metaluminous to mildly peraluminous.

Peralkaline rhyolites tend to be Cl dominated systems (low F/Cl) whereas the metaluminous to peraluminous rhyolites are usually F dominated systems (F/Cl > 3) (Christiansen et al., 1984). The ratio of fluorine to chlorine is very important since each halogen tends to complex with different trace elements.

Experimental data indicates that fluorine complexes preferentially with the HREE's (Mineyev et al., 1966) and empirical observations show that fluorine dominated rhyolitic systems such as topaz rhyolites show enrichments in HREE's, U, Th, Rb, Cs, Ta, and Nb. These observations have been taken as suggesting that fluorine may form complexes with these other elements also (Christiansen et al., 1983, 1984).

Although actual fluorine analyses on the Valle Grande Member rhyolites have not been done at this point they are assumed here to be fluorine dominated systems since biotites contain high fluorine contents, they are metaluminous to weakly peraluminous, and in many other respects such as mineralogy and geochemistry they are very similar to topaz rhyolites as summarized by Christiansen et al. (1986). An examination of Figures 41 and 42 reveals that those elements thought to complex with fluorine are enriched in both differentiation trends. Thus, it is possible that a roofward migrating volatile phase relatively rich in fluorine could carry these particular trace elements along as stable complexes progressively enriching the roof zone of the magma chamber with time. Successively younger eruptions would tap this roof zone thus producing the trends seen.

A major difficulty in calling upon this process to produce enrichments in elements such as HREE's, U, Th, Rb, and Cs is that these same trace elements would be

incompatible with a fractionating phenocryst assemblage made up of minerals seen in the mode. It may therefore be difficult to distinguish between the effects of these two processes if they were acting simultaneously. The fact that crystal-liquid fractionation alone can generally account for the enrichments seen in these elements (see Crystal-Liquid Fractionation), however, suggests that volatile complexing is not an important process, although it cannot be totally discounted.

Soret Diffusion

Soret, or thermal, diffusion is the process of chemical migration in response to an imposed thermal gradient. This mechanism has been proposed to explain roofward enrichments and depletions in major and trace elements in the magma chamber of the Bishop Tuff (Hildreth, 1979, 1981), enrichments and depletions with time in the Coso Volcanic Field (Bacon et al., 1981), and has been suggested in many other instances (Smith, 1979; Mahood, 1981). Soret diffusion has been suggested to operate both in horizontal convection cells where a thermal gradient is imposed between the cooler roof zone of the magma chamber and the hotter, underlying magma (Hildreth, 1979) and at the vertical walls of a magma chamber where the gradient is between a cooler rising boundary layer and the convecting, hotter magma of the interior of the chamber (Carrigan and Cygan, 1986).

Implicit in the operation of the Soret effect to produce differentiation in magmas is that certain elements will be concentrated towards the cold end and others towards the hot end of the system. Until recently actual experimental data on Soret diffusion has been lacking. Work by Lesher and Walker (1983) and Lesher (1986) has now shown that in high-silica rhyolite melts Si is concentrated towards the hot end of the system whereas Fe, Ti, Mg, Mn, K, Na, Rb, Ba, Sr, Nd, Y, and the REE's are concentrated towards the cold end. Whether Soret diffusion is operating in a magma chamber between horizontal convection cells (as in a stably stratified roof zone) or at an upflowing boundary layer along the chamber walls (or both), the effect would be the same in that the roof zone would be progressively enriched in all elements concentrated towards the cold end whereas deeper levels would be enriched in Si. Thus, this process, were it the dominant control on differentiation, would generally produce opposite trends to those observed both in large ash flow sheets (e.g., Smith, 1979; Hildreth, 1981; Kuentz, 1986), in rhyolite domes of the Coso Volcanic Field (Bacon et al., 1981), and in the Valle Grande Member rhyolites. For major elements Soret diffusion would produce enrichments in Fe, Ti, Mg, Mn, K, and Na, along with depletion of Si with time, Although Mn (Fig. 20) does indicate possible enrichment with time, Fe, Ti, Mg, K, and Na either show no change in abundance

or actually show depletions with time (Figs. 18, 19), and Si shows no change in abundance (Fig. 18). Also, Soret diffusion cannot account for the depletion of Ba and Sr with time and the opposite behavior of the LREE's and HREE's (Figs. 41, 42).

Progressive Partial Melting

Progressive melting of a lower crustal granulitic source was considered as a possible model to account for the trends in trace element chemistry seen in the Valle Grande Member rhyolites. In this model successive melt increments could be envisaged as either collecting in a mid to upper crustal magma chamber before eruption or making their way to the surface and erupting as they are produced. Both of these possibilities introduce serious shortcomings to this model even before partial melting calculations are undertaken.

If successive melt increments were collected in a magma chamber before eruption to produce a stable stratified body it would be likely that other processes operating in the magma chamber itself would obscure the original trace element characteristics produced by partial melting before the magmas were erupted. Calculations suggest that even highly viscous rhyolitic magmas will possess sufficiently high thermal Rayleigh numbers ($>10^6$) that they will be undergoing vigorous turbulent convection (Shaw, 1965; Rice, 1981; Sparks et

al., 1984). Other processes which could work to destroy any trace element characteristics imparted by progressive partial melting include crystallization, wall rock reactions, and volatile complexing and diffusion (Hildreth, 1979). The idea of producing a silicic melt batch in the mid to lower crust and getting it to the surface without it ponding in a magma chamber somewhere along the way is probably geologically unreasonable.

Consideration of the trace element enrichments and depletions seen in these rhyolites raises other objections to progressive partial melting as a means of producing the differentiation trends seen. Virtually any source that could be chosen as a parent material in partial melting calculations (granulite, tonalite, amphibolite, etc:) would contain feldspar. Thus, it would be reasonable to expect that the bulk D for such trace elements as Eu, Sr, and Ba would be greater than one (and possibly as high as 2-4) for the expected mineral assemblage in such rocks. In any case of partial melting, those elements with bulk D's >1 will be retained in the source until higher degrees of melting (Arth, 1976; Hanson, 1978). This would produce trends opposite to those observed for Eu, Sr, and Ba in that progressive melting would cause increases with time, not decreases as is seen (Figs. 23, 25, 41, 42). The behavior of elements of the first transition series, Sc, Ti, Mn, and Fe, provide further evidence against direct partial melting

as a mechanism to produce the geochemical trends seen. These elements would be expected to be strongly compatible with any ferromagnesian phases present in the source and thus should show behavior similar to that suggested for Eu, Sr, and Ba. Although Mn does seem to show enrichments with time (Fig. 20), Sc, Ti, and Fe all tend to show slight depletions (Figs. 19, 41, 42). Elements such as Cs which would be incompatible with virtually any mineral assemblage (bulk D $<<1$) would be expected to greatly enriched in the first melts to be generated at low degrees of melting (Arth, 1976). Thus, with progressive melting Cs would be expected to concentrate greatly in the first melts produced with successive melts having lesser abundances. Once again, this is opposite to the actual trends observed in the Valle Grande Member rhyolites since the abundance of Cs actually increases with time (Figs. 21, 41, 42).

Taken as a whole the objections to progressive partial melting outlined above seem to rule out this mechanism as a way to produce the geochemical trends seen in these rhyolites. Other workers dealing with rhyolitic systems having differentiation trends similar to those seen here have voiced much the same objections to progressive partial melting as a viable petrogenetic model (Hildreth, 1979, 1981; Mahood, 1981; Christiansen et al., 1984).

Roof Rock Contamination

Another mechanism considered to produce the geochemical trends documented during this study is that of roof rock contamination. If these magmas had remained in a relatively shallow magma chamber, as is indicated by normative compositions and mineral equilibria, then Proterozoic granitic rocks exposed in the Nacimiento Uplift 15 km west of the caldera would be likely compositions to represent roof rocks for the magma chamber. An examination of the trace element compositions for the oldest (least evolved) and the youngest (most evolved) domes of trends 1 and 2 along with the average composition of Proterozoic granitic rocks of the Nacimiento Uplift (Condie, 1978) reveals that progressive contamination of the least evolved rhyolites in each trend by these compositions cannot account for the chemical variations seen (Table 5). In particular, opposite trends to those seen would be produced for Rb, Sr, Zr, Ba, Eu, Tb, Yb, and Lu.

Admittedly this model suffers from the fact that the actual composition of the roof rock(s) is unknown. Were they more mafic, as is suggested by lithologies found during drilling at the Fenton Hill site (Heiken and Goff, 1983), the contrast would be even greater for elements such as Sr, Zr, Ba, and Eu which tend to be present in greater abundances in mafic rocks than in felsic rocks. In summary, the highly evolved nature of these rhyolites

Table 5. Average composition of Proterozoic granitic rocks exposed in the Nacimiento Uplift (from Condie, 1978) used as possible roof rocks for contamination.

	Trend 1		Trend 2		
Element	DM-II	SL	SA-I	SM	Roof Rocks
Rb	153	265	180	219	159
Sr	4.4	3.7	47	25	197
Zr	163	122	130	118	190
Ba	30	29	229	111	740
Cs	4.9	9.6	5.2	7.3	7.1
La	44.4	31.6	44.4	34.8	30.7
Ce	92.9	66.6	90.7	71.0	74.0
Sm	6.7	6.7	6.1	6.0	7.2
Eu	0.19	0.09	0.32	0.21	1.20
Tb	1.2	1.7	1.1	1.3	1.0
Yb	4.4	8.1	4.9	5.9	3.3
Lu	0.66	1.27	0.73	0.97	0.57

Note: Data for DM-II, SL, SA-I, and SM are averages of all samples from each respective dome.

(e.g., low Sr, Ba, Eu, etc:) precludes roof rock contamination by any reasonable lithology as a mechanism to produce the differentiation trends seen.

Crystal-Liquid Fractionation

Many workers seeking to explain the extreme variations in trace element abundances but relatively constant major element abundances seen in high-silica rhyolites have discounted crystal fractionation as a viable petrogenetic process (Shaw et al., 1976; Hildreth, 1979, 1981; Smith, 1979; Bacon et al., 1981; Mahood, 1981; Mahood and Hildreth, 1983). Objections against crystal fractionation have included low Stokes settling velocities of the observed phenocrysts in a rhyolitic melt (Hildreth, 1979; Mahood, 1981), the high yield strength of rhyolitic magmas (Hildreth, 1981), the fact that many of these magmas are virtually aphyric (Shaw et al., 1976; Hildreth, 1979; Bacon et al., 1981; Mahood, 1981), and the fact that trace elements vary greatly whereas major elements remain relatively constant (Hildreth, 1979; Mahood, 1981). Recently, however, a large body of evidence has begun to accumulate which suggests that crystal-liquid fractionation processes are responsible for the major and trace element differentiation trends seen in high-silica rhyolites.

One factor involved in this return of crystal-liquid fractionation to favor is the recent experimental data on

the Soret effect (Lesher and Walker, 1983; Lesher, 1986) which indicates that it produces opposite trends to those observed. The Soret effect was central to Hildreth's (1979) thermogravitational model for zoning produced in the magma chamber of the Bishop Tuff. Data on the Bishop Tuff has now been re-interpreted by several workers as being consistent with fractionation of the observed phenocryst phases (Cameron, 1983; Michael, 1983; Cameron, 1984). The evolution of topaz bearing high-silica rhyolites of the western United States has been interpreted as consistent with fractionation of the observed phenocrysts (Christiansen et al., 1983, 1984, 1986). Similar differentiation trends in granitic plutons (Mittlefehldt and Miller, 1983), in both high and low silica rhyolites from the Sierra Madre Occidental in Mexico (Cameron and Hanson, 1982), as well as in highly alkalic magmas (Wolff and Storey, 1983, 1984) have been accounted for by fractionation of crystalline phases present in these rocks.

Fractional crystallization in the classical sense of crystal settling is probably geologically unreasonable when dealing with rhyolitic magmas mainly due to the fact that the calculated convective velocities greatly exceed settling velocities of phenocrysts and thus crystal settling will be severely inhibited (Sparks et al., 1984; Marsh and Maxey, 1985). Recent theoretical and experimental work, however, has shown that a more

probable mechanism for crystal-liquid fractionation is that of side wall crystallization, the rise of a bouyant boundary layer, and collection of differentiated liquids as a stable, density stratified, roof zone (Nash and Crecraft, 1981; Rice, 1981; Turner and Gustafson, 1981; Huppert and Sparks, 1984; Sparks et al., 1984; McBirney et al., 1985; Nilson et al., 1985; Baker and McBirney, 1985). In a magma body cooling from the top and sides, as would be the case for an upper crustal intrusion, much of the crystallization would be expected to occur along the margins of the chamber where the largest degree of undercooling exists and nucleation sites are abundant (Huppert and Sparks, 1984; Sparks et al., 1984). This idea is supported by field observations of granitic plutons which show evidence of having solidified from the margins inward (Bateman and Chappell, 1979; McCarthy and Groves, 1979; Atherton, 1981). The magma immediately adjacent to the crystallizing margin of the chamber will be selectively depleted in those elements which have an affinity for the growing crystals. In all magmas except for tholeiitic basalts (which undergo Fe enrichment) the residual melt density decreases during fractionation, thus a boundary layer of more differentiated melt will form and begin to rise towards the roof of the magma chamber (Sparks et al., 1984; McBirney et al., 1985). Collection of these more evolved melts at the roof of the magma chamber can form a stable, density stratified, roof

zone in which the most differentiated liquids will be progressively concentrated towards the uppermost layers (Fig. 43). Spera et al. (1984) have presented arguments against crystal-liquid fractionation by this process, however, in light of our present knowledge it is considered the most probable mechanism.

Rayleigh fractionation models were tested for the production of the most evolved (youngest) rhyolites in each differentiation trend from the least evolved (oldest) rhyolites based on the assumption that crystal-liquid fractionation by side wall crystallization is a viable mechanism. For major element abundances analytical errors (Appendix G) and variation within an eruptive unit (see Whole Rock Chemistry) are often as large as variations between eruptive units. Therefore major element fractionation modelling is not practical. As previously mentioned (see Normative Compositions), crystallization at a minima (or eutectic) will tend to fix major element composition whereas the enrichment or depletion of trace elements will be controlled by minor crystallizing phases which concentrate those elements (Baker and McBirney, 1985; McBirney et al., 1985). Examination of Figures 41 and 42 reveals that trace elements depleted in the Valle Grande Member rhyolites are those which would be expected to be compatible (Kd's >1) with phenocrysts seen in the mode. Sr and Eu are strongly partitioned into plagioclase. Ba, Eu, and to

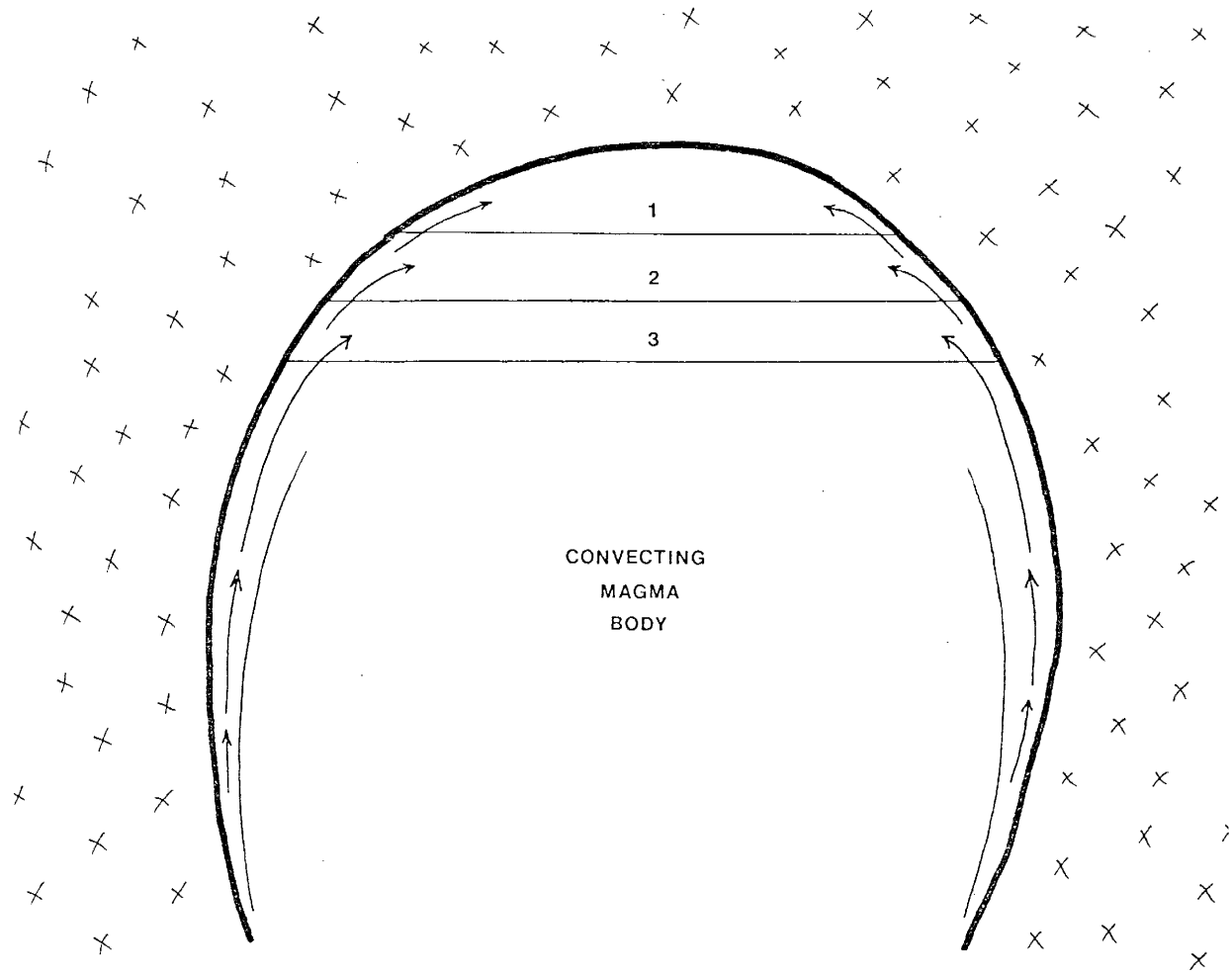

Figure 43. Generalized cartoon diagram of magma chamber depicting side wall crystallization, rise of bouyant boundary layer (upward pointing arrows), and collection of differentiated magma as stratified roof zone (1 indicating most evolved magma, 2 and 3 successively more primitive).

a lesser extent Sr, are concentrated in sanidine. Zr and Hf are compatible with crystallizing zircon. The LREE's are preferentially concentrated in allanite. Rb is compatible with fractionating biotite, Nb with biotite, zircon, and hornblende, and the HREE's with hornblende reflecting the fact that they are not as enriched as Cs and Ta (Figs. 41, 42) which are not concentrated in any crystallizing phases to an appreciable extent.

Huppert and Sparks (1984) and Sparks et al. (1984) have suggested that when modelling crystal-liquid fractionation by side wall crystallization that an additional degree of freedom exists in that crystals accreted to the margins of the chamber control the chemical evolution of the magma and not the phenocrysts seen in the erupted products. The two mineral assemblages may or may not be the same. In the Rayleigh fractionation models tested it was assumed first that phenocrysts were separated in modal proportions and that only those minerals seen in the mode were removed from the magma. Slight adjustments eventually had to be made to the modes used in the calculations in order to obtain the best fit for the data, therefore in some cases the final model suggests fractionation of phases in slightly greater or lesser quantities than they appear modally. A perfectly acceptable model, however, was obtained using only phenocrysts actually present in the erupted rhyolites.

One final difficulty in applying a crystal-liquid

fractionation model to these rhyolites involves the selection of appropriate partition coefficients (Kd's). It is known that Kd's for high-silica rhyolites may vary greatly between eruptive centers and in general tend to be higher than Kd's in less siliceous magmas (Leeman and Phelps, 1981; Mahood and Hildreth, 1983; Nash and Crecraft, 1985). Due to the large number of phenocryst phases present in the Valle Grande Member rhyolites and the scarcity of data for high-silica rhyolites, Kd's had to be amassed from a number of sources. Wherever possible data was taken from rhyolites geochemically as close to the ones in this study as possible (e.g., Bishop Tuff). A complete list of Kd's used as well as sources is given in Appendix H.

Considering the above mentioned uncertainties the closeness of fit of the model calculations to the observed compositions is remarkable (Tables 6, 7; Figs. 44, 45).

The model calculated for trend 1 (Table 6; Fig. 44) shows a good fit of the calculated daughter (C_L) composition to the actual daughter composition (SL) for all trace elements considered except Sr, Ba, Sm, and Hf. When analytical errors and variation within eruptive units are taken into account all elements except those just mentioned fit the model very well and the discrepancy for those that do not fit is reduced substantially. The much greater depletions of Sr and Ba

Table 6. Rayleigh fractionation model for trend 1.

	Trend 1 - 1.18-0.71 Ma		
Element	C_o (DM-II)	Obs. C_L (SL)	Calc. C_L
Sc	1.5	1.5	1.5
Rb	153	265	255
Sr	4.4	3.7	1.6
Y	44.1	80.5	80.6
Zr	162.7	121.7	121.9
Nb	51.3	89.5	90.9
Cs	5.0	9.6	10.0
Ba	30	29	15
La	44.4	31.6	31.0
Ce	92.9	66.6	74.5
Sm	6.65	6.71	8.91
Eu	0.19	0.09	0.10
Tb	1.21	1.71	1.99
Yb	4.43	8.13	7.77
Lu	0.66	1.27	1.16
Hf	7.04	6.43	8.34
Ta	3.94	7.85	7.69
Pb	28.7	35.6	32.0
Th	17.26	29.75	28.81
U	5.50	10.53	10.97

Mineral	Mode (wt.%)	
Qtz	50.0	
San	30.0	
Plag	16.0	
Bio	1.8	
Hbl	1.1	
Cpx	0.57	F = 0.46
Ilm	0.28	
Mgt	0.12	
All	0.05	
Ap	0.03	
Zir	0.02	
Opx	0.01	

Note: Rayleigh fractionation equation, $C_L/C_o = F^{(D-1)}$

where, C_o = parent liquid, C_L = daughter liquid

F = weight fraction of melt remaining

D = bulk distribution coefficient

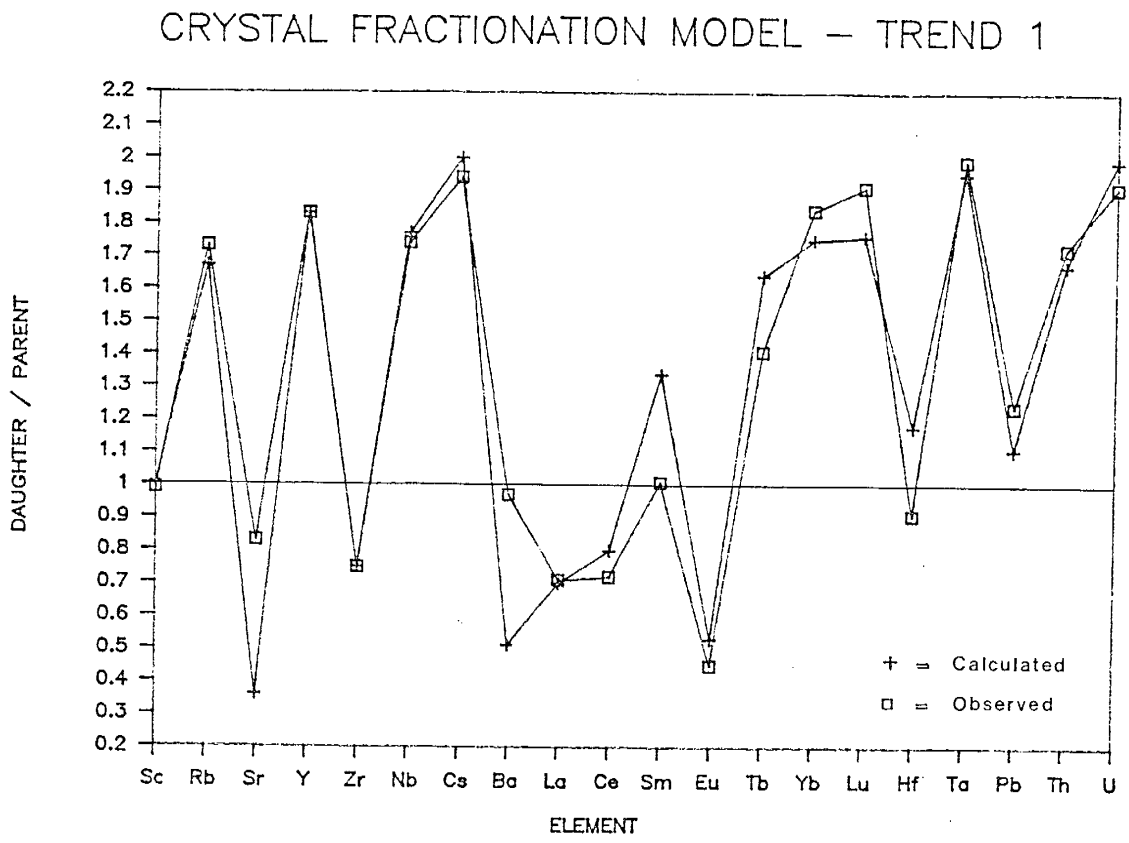

Figure 44. Comparison of observed enrichments/depletions to those calculated for trend 1.

Table 7. Rayleigh fractionation model for trend 2.

	Trend 2 - 0.55-0.51 Ma		
Element	C_o (DM-II)	Obs. C_L (SL)	Calc. C_L
Sc	2.4	2.3	2.4
Rb	180	219	217
Sr	47.3	25.0	28.3
Y	45.3	58.7	59.0
Zr	130.0	117.9	118.2
Nb	50.1	62.1	63.5
Cs	5.2	7.3	7.0
Ba	229	111	132
La	44.4	34.8	32.4
Ce	90.7	71.0	72.0
Sm	6.09	6.00	6.64
Eu	0.32	0.21	0.21
Tb	1.09	1.29	1.33
Yb	4.87	5.95	6.29
Lu	0.73	0.97	0.95
Hf	5.36	5.15	5.94
Ta	4.81	6.25	6.60
Pb	25.6	26.4	24.0
Th	24.08	29.13	29.72
U	6.88	8.54	9.45

Mineral	Mode (wt.%)	
Qtz	38.0	
San	43.0	
Plag	15.0	
Bio	2.5	
Hbl	1.3	
Cpx	0.50	F = 0.70
Ilm	0.05	
Mgt	0.03	
All	0.068	
Ap	0.017	
Zir	0.01	
Opx	0.01	

Note: Rayleigh fractionation equation, $C_L/C_o = F^{(D-1)}$

where, C_o = parent liquid, C_L = daughter liquid

F = weight fraction of melt remaining

D = bulk distribution coefficient

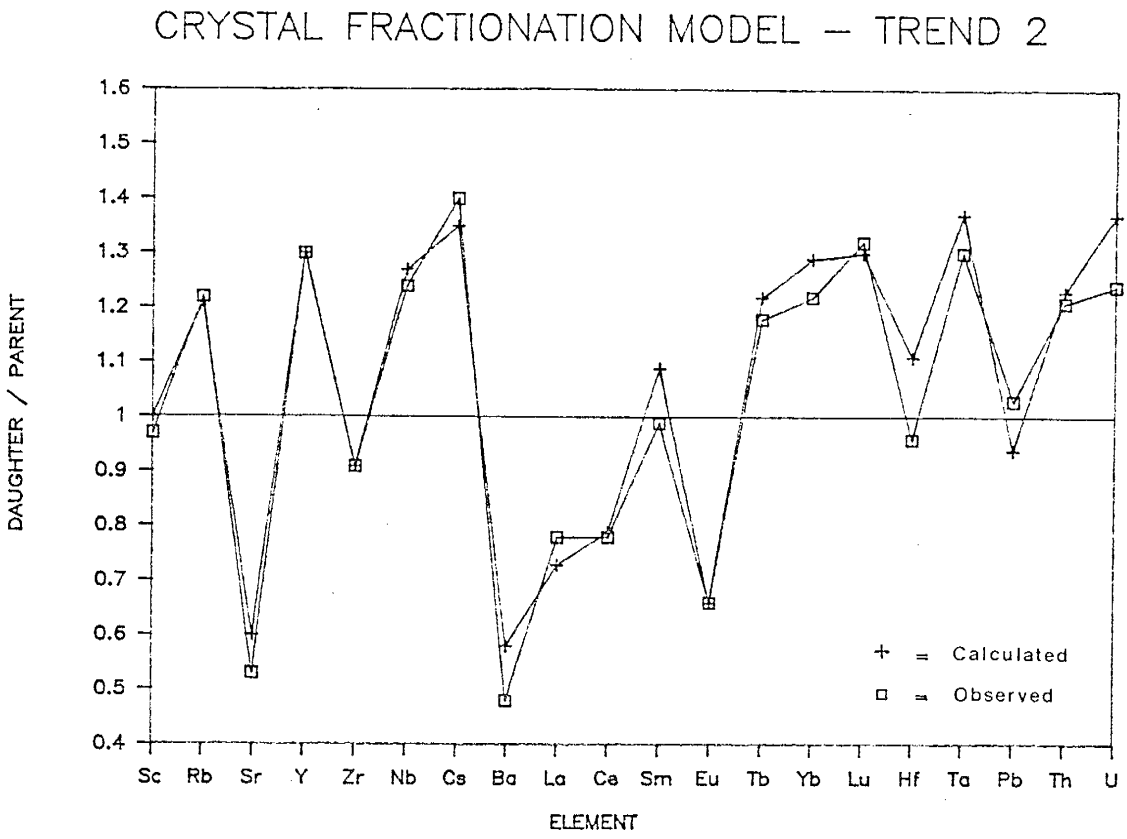

Figure 45. Comparison of observed enrichments/depletions to those calculated for trend 2.

predicted by the model suggests that the actual Kd's for those elements in sanidine and plagioclase were lower than those chosen (Appendix H). The fact that the model does not predict the slight depletion of Hf actually seen can likewise be accounted for by assuming that the Kd for Hf in zircons in these rhyolites is higher than the value chosen from the literature. The discrepancy between the observed and model abundance of Sm suggests that the actual Kd for this element in allanite is higher than the Kd used. Alternatively, the behavior of Sm could be modelled by assuming that sphene was a fractionating phase. Calculations have indicated that 0.1-0.2 wt.% sphene in the mode would bring the calculated abundance of this element in line with the observed abundance.

The model calculated for trend 2 (Table 7; Fig. 45) shows a better fit to the observed composition than the model for trend 1. The only element outside the range of analytical error and intra-unit variation is Hf. As previously suggested this probably indicates that the actual Kd for Hf in zircon is higher than the Kd chosen. The better fit of the model for trend 2 may reflect the fact that there is only ~40,000 yrs. represented whereas the time period represented by trend 1 is ~470,000 yrs. Thus, there would be a much greater chance that other minor processes may have acted to modify the variations produced by crystal-liquid fractionation in trend 1.

Reversals In Trends

This section deals with reversals 1 and 2 (at 0.71-0.55 and 0.51-0.45 Ma respectively) as defined in Whole Rock Chemistry. Both of these reversals represent breaks in the preceeding differentiation trends wherein the next erupted magmas represent less evolved compositions (e.g., higher Sr, Ba, Zr, Eu and lower Rb, Y, Nb, Cs, etc:). Mechanisms considered here to account for these reversals are the disruption of a stratified roof zone, magma mixing, and the eruption of a totally new magma batch which is genetically unrelated to previously erupted magmas.

Disruption of a Stratified Roof Zone

Examination of large ash flow sheets, which are in effect inverted pictures of the uppermost part of a high level magma chamber at one point in time, has revealed that strong vertical gradients in trace element abundances exist in many instances (e.g., Smith, 1979; Hildreth, 1981). The differentiation represented by trends 1 and 2 could be pictured as a progressive build up of a stratified cap or roof zone (e.g., Fig. 43) where the uppermost layer becomes more evolved with time. Successive eruptions would presumably tap this uppermost layer producing the trends seen. Eruption of an unusually large volume of material could deplete the uppermost

layer(s) and cause disruption of the established zoning with the next eruptive products being drawn from a deeper, less evolved layer. Such a model for producing discontinuities in geochemical trends has been proposed by Baker and McBirney (1985) based on laboratory models and theoretical considerations. Smith (1979) suggested a similar process for the pre-Toledo caldera eruptives through post-Bandelier Tuff eruptives in the Jemez Mtns. based on Nb abundances.

A test for this particular model is whether or not reversals are preceeded by unusually large volume eruptions. Rough estimates of volumes of erupted material represented by each dome (excluding any possible pyroclastics associated with vent opening) indicate that Del Medio II (1.18 Ma), San Antonio I (0.55 Ma), and South Mountain (0.51 Ma) were by far the most voluminous eruptions with others being minor in comparison. Thus this model is compatible with reversal 2 being produced by eruption of a relatively large volume of material (South Mountain) with the next eruption (San Antonio II at 0.45 Ma) representing a deeper, less evolved, layer. Reversal 1, however, could not reasonably have been produced in this manner since the preceeding eruption, San Luis, was of comparatively small volume. Also, San Antonio I represents the largest volume of magma of any of the Valle Grande Member domes and it is immediately followed by more evolved magmas (La Jara and South

Mountain) rather than by less evolved magmas as would be expected.

Magma Mixing

Another process by which the observed reversals could be produced is that of magma mixing. In this case each differentiation trend would be terminated and the reversals produced when the magma chamber is recharged by an influx of fresh magma. Alternatively, mixing between layers in a stratified roof zone could be a possible mechanism to produce the reversals seen.

The case of magma chamber recharge and subsequent magma mixing is perhaps the simplest and most obvious process. The major difficulty in calling upon this mechanism is that density contrasts between silicic and more mafic magmas will tend to inhibit mixing since the more mafic magma would tend to pond at the base of the silicic magma column (McBirney, 1980; Huppert et al., 1982a). Empirical observations (Eichelberger, 1980), theoretical considerations (Huppert et al., 1982a), and laboratory experiments (Huppert et al., 1982b), however, suggest that in certain instances of magma chamber recharge mixing is possible, even between basalt and rhyolite. Eichelberger (1980) and Huppert et al. (1982a) suggest that the mechanism involved is cooling of the hotter, denser, more mafic magma injected into the base of the magma chamber by heat transfer into the overlying

silicic magma. This cooling causes crystallization of the mafic magma, thereby reducing density, although this alone is not enough to trigger mixing. Once crystallization has proceeded far enough, and provided that there was sufficient water present, the more mafic magma could reach saturation. Subsequent vesiculation is envisioned as providing the driving force behind mixing as this would reduce the density of the mafic magma below that of the overlying silicic magma. Compositional zonation in the upper, more silicic part of the magma chamber would tend to confine mixing to lower levels unless the zonation was poorly developed and consisted of relatively few layers in which case mixing could effect the whole magma chamber (Huppert et al., 1982b).

Assuming that mixing could occur by this process, calculations were made using a variety of end members represented by more mafic volcanics erupted in the Jemez Mountains. Least squares approximations from major element compositions were made first and the proportions of end members thus calculated were used to calculate trace element compositions. Lithologies chosen as end members were Cerro Rubio Quartz Latite, Tschicoma dacite, Tschicoma andesite, Lobato Basalt (Gardner et al., 1986), and a hornblende latite pumice erupted with the upper Bandelier Tuff (J.N. Gardner, 1986, personal commun.; Self et al., 1986). Calculations were made using these end members for production of reversal 1 (San Luis + end

member = San Antonio I) and reversal 2 (South Mountain + end member = San Antonio II). Although major element least squares approximations produced acceptable fits for all the end members tested, none produced acceptable fits for trace elements. The problem encountered with any of these models was governed by the mixing proportions generated by the major element calculations. The most silicic end member chosen (Cerro Rubio Quartz Latite - 66.9% SiO_2) demanded 9.2% mixing to produce reversal 1 and only 2.4% mixing to produce reversal 2. The most mafic end member tested (Lobato Basalt - 50.51% SiO_2) required 2.9% and 0.6% mixing respectively. When these mixing proportions are applied to trace elements they cannot account for the large reductions in Rb, Cs, HREE's, Th, and U, nor can they account for the large increases in Sr, Ba, LREE's, and Eu seen at each reversal.

The failure of the calculations discussed above to identify an existing end member for mixing led to an alternate method, that of calculating hypothetical end members. This was accomplished by assuming a value for SiO_2, determining mixing proportions from this value, and then use using the mixing proportions to calculate other major and trace elements for the hypothetical end member. Initial calculations using SiO_2 values of 46 wt.% showed that absurd compositions were produced (6.22 wt.% Fe_2O_3, 8.72 wt.% K_2O, 500 ppm Ce, etc:) for some elements

whereas many others actually would require negative values to acheive proper mixing proportions. Further calculations have indicated that only mixing with another high-silica rhyolite in nearly 50:50 proportions could satisfy all major and trace element variations seen in the reversals. It is this fact that leads to consideration of the second mixing mechanism, that of mixing between layers in a stratified roof zone. Based upon laboratory studies (Huppert et al., 1982b) and theoretical considerations (Rice, 1981) it has been suggested that in a magma chamber which has developed a stable, stratified roof zone adjacent layers will often mix. This breakdown of stratification could be caused by crystallization in the lower, denser layer resulting in decreased density, release of volatiles from the upper layer resulting in increased density, or heating of the magma chamber from below (Rice, 1981; Huppert et al., 1982b).

If this mechanism were operating to produce the reversals seen then it would be expected that the mixing would take place in roughly 50:50 proportions (assuming that the adjacent layers were of roughly equal thickness) and that the end member required would be another high-silica rhyolite of less evolved composition. The compositions of the hypothetical end members calculated by the method outlined above as well as the mixing proportions required conform to these expectations

(Table 8). Examination of the major and trace element abundances of the calculated end members reveals that they are less evolved than any of the erupted magmas represented by the Valle Grande Member rhyolites (Appendix F). If these hypothetical end members do represent possible compositions for mixing then presumably they were present at a lower level in the magma chamber than any of the rhyolites actually erupted. This model suffers from the fact that it cannot be directly proven since the calculated end members, if they existed, were never erupted separately.

New Magma Batch

The models discussed above would suggest a single, long-lived magma chamber beneath the Valles Caldera as implied by Smith (1979). A large body of evidence, however, has recently begun to accumulate which suggests that rhyolitic magmas in the Jemez Mountains over the past 2-3 million years represent a series of independently generated and erupted magma batches with a variety of upper crustal, lower crustal, and mantle (basaltic) sources (Wolff et al., 1987; J.A. Wolff and P.R. Kyle, 1987, personal commun.). The data set compiled during this study is compatible with this interpretation. If this type of interpretation were correct the Valle Grande Member rhyolites could represent three separate magma batches, two of which remained closed systems for

Table 8. Calculated hypothetical end members and mixing proportions for producing reversals 1 and 2. R = calculated rhyolite end member.

Element	Reversal 1 Rhyolite	Reversal 2 Rhyolite
SiO_2	75.00	76.00
TiO_2	0.21	0.20
Al_2O_3	13.29	13.09
Fe_2O_3	1.32	1.28
MnO	0.05	0.04
MgO	0.42	0.20
CaO	0.94	0.30
Na_2O	3.67	4.08
K_2O	5.10	4.75
P_2O_5	0.03	0.02
TOTAL	100.03	99.96
Rb	126.9	134.0
Sr	75.0	67.7
Y	23.65	24.80
Zr	136.4	141.8
Cs	2.4	1.45
La	52.3	49.17
Ce	105.5	101.2
Nd	34.5	38.8
Sm	5.7	6.6
Eu	0.46	0.49
Tb	0.71	0.88
Yb	2.8	2.9
Lu	0.4	0.3
Ta	2.9	2.9
U	4.5	4.9

Mixing Proportions:

Reversal 1 - (0.405)(SL) + (0.595)(R) = SA-I

Reversal 2 - (0.540)(SM) + (0.460)(R) = SA-II

sufficient periods of time to generate highly evolved differentiates. Magmas erupted from 1.18-0.71 Ma (trend 1) would represent the first magma batch, those erupted from 0.55-0.51 Ma (trend 2) would represent the second magma batch, and finally, the last eruption of the Valle Grande Member, San Antonio II at 0.45 Ma, would represent a third magma batch.

Undated Domes

A total of 8 samples were collected from undated domes (Del Medio III, Del Abrigo I and II) and were excluded from the presentation and discussion up until this point. Doell et al. (1968) suggested that these domes fit into the Valle Grande Member sequence between Del Medio I and Del Abrigo III (~1.07 and ~0.91 Ma respectively) and have relative ages in the order listed above (see Table 1). The samples representing these undated domes are DM-4, DM-7, and DM-8 (Del Medio III), DA-1, DA-3, DA-4, DA-5 (Del Abrigo I), and DA-8 (Del Abrigo II). Complete chemical analyses of these samples is given in Appendix F.

Comparison of the trace element chemistry of the samples representing Del Medio III reveals that for the most part they are indistinguishable from Del Medio I and II samples. Compatible elements Sr, Ba, La, Ce, and Hf, along with incompatible elements Y, Nb, Cs, Yb, Lu, Ta, Th, and U are virtually identical. Slightly higher Zr and

Eu, along with slightly lower Rb are the only trace elements that would suggest that Del Medio III samples are slightly less evolved than Del Medio I and II samples. Based on the morphology of the composite dome made up of these three extrusions it seems that Del Medio III was erupted last as suggested by Doell et al. (1968). If this is the case then there must not have been sufficient time for any significant differentiation to occur between the eruption of Del Medio I, II, and III.

Comparison of the trace element chemistry of the samples representing Del Abrigo I and II to those representing Del Abrigo III presents a similar picture. There is virtually no difference between these three groups in terms of compatible elements Zr, Ba, La, Ce, Eu, and Hf, or incompatible elements Rb, Y, Nb, Yb, Lu, Ta, Th, and U. Slightly higher Sr and Cs for Del Abrigo III samples are the only differences seen. Based on the morphology of the composite dome made by Del Abrigo I, II, and III it is not immediately obvious that these units represent three separate extrusions, only that Del Abrigo III seems to be a separate event. If separate eruptions are represented by these three groups as suggested by Doell et al. (1968), then, as for Del Medio I, II, and III, there must not have been sufficient time for significant differentiation to occur between the time of eruption of Del Abrigo I, II, and III. All Del Abrigo samples, however, are significantly more evolved than any

Del Medio samples and less evolved than the next youngest eruptives, Santa Rosa I.

Comparison With Other Valles Rhyolite Members

Other members of the Valles Rhyolite Formation erupted prior (Deer Canyon, Redondo Creek) and after (VC-1 Rhyolite, Battleship Rock, El Cajete, Banco Bonito) the Valle Grande Member have, until recently, been assumed to be a part of a co-magmatic suite ranging back to, and including, the pre-Bandelier ignimbrites (Smith, 1979). Gardner et al. (1986) first indicated that the Valles Rhyolite Formation could be divided into two groups: a high-silica group consisting of the Deer Canyon, Redondo Creek, and Valle Grande Members, and a low-silica group consisting of the younger VC-1 Rhyolite, Battleship Rock, El Cajete, and Banco Bonito Bembers. Wolff et al. (1987) have produced evidence which suggests that the Valles Rhyolite Formation is geochemically distinct from the Bandelier type magmas preceeding it and that the members younger than the Valle Grande Member are a geochemically coherent group.

Only one published analysis of the Redondo Creek Member exists (Gardner et al., 1986) and there are no known analyses of the Deer Canyon Member. Comparison of the major and trace element data from the Redondo Creek rhyolite analysis to that of the first erupted unit of the Valle Grande Member, Del Medio II, reveals both

similarities and differences. Both have similar major element (SiO_2, Al_2O_3, Fe_2O_3, MnO, MgO, Na_2O, K_2O, and P_2O_5) compositions. The Redondo Creek rhyolite, however, has higher TiO_2 and CaO. Trace elements show greater differences than do major elements and generally suggest that the Redondo Creek rhyolite could be a less evolved forerunner to the Del Medio rhyolites. Significantly higher abundances of compatible elements Sc, Cr, Zr, Ba, La, Ce, and Eu, along with lower incompatible elements Rb, Cs, Yb, Th, and U bear this out. Although crystal-liquid fractionation modelling relating the Redondo Creek rhyolite to the Del Medio rhyolite was not done it appears entirely feasible that they could be related in this manner. These observations must be qualified by the fact that there exists only one analysis of the Redondo Creek rhyolite and further documentation of the relationship of this member to the Valle Grande Member rhyolites (more analyses, isotope data, etc:) may not bear out these inferences.

During the course of this study one sample of the VC-1 Rhyolite (VC1-R) and two of the Banco Bonito (BB-1, VC1-BB) were analyzed (see Appendix F). Wolff et al. (1987) have shown that the Battleship Rock, El Cajete, and Banco Bonito Members are a geochemically coherent group. Thus, the two Banco Bonito analyses done during this study are taken as being representative of that group in the following discussion. It is immediately

obvious that these younger rhyolites are not related to the Valle Grande Member rhyolites. They are significantly lower in SiO_2 and K_2O, and higher in TiO_2, Fe_2O_3, MgO, CaO, and P_2O_5. Compatible trace elements such as Sc, Cr, Sr, Zr, Ba, and Eu are present in much greater abundances whereas incompatible trace elements such as Rb, Cs, HREE's, Pb, Th, and U are much lower than those of the youngest unit of the Valle Grande Member. In some respects the VC-1 Rhyolite appears slightly more evolved than the Banco Bonito group. Major elements which suggest this are slightly higher SiO_2 and K_2O, and lower Al_2O_3, Fe_2O_3, and CaO. Compatible trace elements such as Sr, Ba, and Eu are significantly lower and incompatible trace elements such as Rb, Nb, Cs, HREE's, Pb, and Th appear to be slightly higher in the VC-1 Rhyolite. This may indicate that the VC-1 Rhyolite is genetically unrelated to the youngest group of eruptives.

CONCLUSIONS

Valle Grande Member rhyolites represent ~730,000 years of post-caldera volcanism in the Valles Caldera. Bailey et al. (1969) suggested that all eruptive units of the Valle Grande Member are part of a co-magmatic suite based upon their spatial and temporal relationships in the moat zone of the caldera as well as progressive changes in phenocryst content seen. The detailed trace element geochemistry provided by this study, however, indicates that these rhyolites may not represent a co-magmatic suite.

The Valle Grande Member appears to consist of at least 3 separate magma batches, one represented by lavas erupted from 1.18-0.71 Ma, a second by those erupted from 0.55-0.51 Ma, and a third by those erupted at 0.45 Ma. The first two magma batches remained closed systems for sufficient periods of time to generate distinctive trace element geochemical trends. Two to three fold enrichments in Rb, Y, Nb, Cs, HREE's, Ta, Pb, Th, and U, and depletions in Sr, Zr, Ba, LREE's, Eu, and Hf with decreasing age are seen during each of these trends. Major element abundances remain relatively constant in comparison.

Rayleigh fractionation models using phenocrysts present in the mode can, in both instances, account for

the differentiation trends seen. Crystallization at a minima or eutectic, which is suggested by normative compositions plotted on the Q-Ab-Or diagram, is consistent with the relatively fixed major element abundances seen in these rhyolites. The abundances of trace elements are controlled by their compatibility or incompatibility in minor liquidus phases such as zircon and allanite and thus are expected to vary widely. The mechanism by which crystal-liquid fractionation is though to occur is that of side-wall crystallization, the rise of differentiated liquids as a bouyant boundary layer, and collection of these liquids in a stable, density stratified roof zone. Geothermometry using co-existing sanidine and plagioclase rim compositions, geobarometry using Al contents of hornblende rims, and normative compositions plotted on the Q-Ab-Or diagram indicate that fractionation took place at shallow depths (<7.5 km) with liquidus temperatures averaging 755 °C.

The nature of the phenocryst assemblages seen in these rhyolites suggests a complex history of melt generation, collection in a high-level magma chamber, crystallization, and subsequent eruption. Wolff et al. (1987) have interpreted the petrographic features of younger members of the Valles Rhyolite Formation as indicating melt generation and eruption on a short time scale (within 10,000-100,000 years) with many of the "phenocrysts" actually being material from the source

area. The phenocryst assemblage of the Valle Grande Member rhyolites seems to be a mixture of mineral phases inherited from the source area and phenocrysts which actually crystallized from the magma. Much of the strongly resorbed quartz seen may actually be quartz crystals from the source area which have not been totally melted. The one andesine core composition determined by microprobe is without doubt xenocrystic in origin and suggests a mafic igneous component in the source area. The rare biotites exhibiting bent cleavages may be indicative of a metamorphic component in the source area. Most petrographic features, however, imply that the majority of the phenocrysts did crystallize from the magma. Among them are pyramidal and bi-pyramidal terminations and hexagonal cross-sections exhibited by many quartz phenocrysts along with perfectly euhedral sanidine, plagioclase, biotite, hornblende, apatite, zircon, and allanite phenocrysts.

The progressive changes in phenocryst sizes and abundances seen in the Valle Grande Member rhyolites must be considered in any model proposed. At the outset of this study it was considered that these progressive changes could reflect the cooling and crystallization of a single sub-caldera magma chamber from which all of these rhyolites were erupted. Trace element geochemistry, however, suggests that these rhyolites represent three separate magma batches. One interpretation of this

seemingly conflicting data is that the Valle Grande Member rhyolites may be magmas that were ultimately derived from a single, parental magma chamber, but that each group of samples represents magma batches which occupied separate cupolas during the period of time they were undergoing differentiation.

The results of this study have both answered many long standing questions about the nature of silicic volcanism in the Valles Caldera and shown the need for further work. The Valle Grande Member rhyolites are part of a much longer period of silicic eruptions in the Jemez Mountains ranging back to ~3 Ma. Only in the last few years has this volcanic activity truly begun to be understood. A large data base of detailed major and trace element geochemistry has now been amassed through the combined efforts of many workers. Isotope studies, however, are largely lacking at this point. A detailed isotopic study involving several isotopic systems and covering the period of rhyolitic volcanism from recent to ~3 Ma would provide much needed constraint on the "batch" nature of these magmas as well as provide information on source areas that is unobtainable through trace element geochemistry alone. Also lacking at this point is detailed age dating. Although there are many K-Ar age dates on these rhyolites they are by no means complete. Many eruptive units are constrained in age through stratigraphy alone and others are undated. The $^{40}Ar/^{39}Ar$

dating technique has been refined in recent years and is a powerful tool for dating sequences of volcanic rocks erupted within short periods of time due to its great precision. Existing K-Ar dates cannot distinguish differences in age between many of these eruptive units (but often suggest it). Thus, application of the $^{40}Ar/^{39}Ar$ technique in a detailed study could also prove to be important in furthering our understanding of silicic volcanism in the Jemez Mountains over the past 3 Ma.

APPENDIX A

SAMPLE LOCATIONS

This appendix contains sample locations for all samples collected during this study. Locations given include latitude and longitude, name of the quadrangle, and general location on the particular dome the sample was collected on. Also included is the type of outcrop the sample was taken from. Samples are generally listed in order of decreasing age.

APPENDIX A (continued)

DM-0: Valle Toledo quadrangle, on SW side of Del Medio II, 35°53'08"N 106°28'18"W. Float exposed in roadcut.

DM-1: Valle Toledo quadrangle, on SW side of Del Medio II, 35°53'16"N 106°28'11"W. Exposures in firebreak cut into dome.

DM-2: Valle Toledo quadrangle, on S side of Del Medio II, 35°52'42"N 106°27'21"W. Exposures in roadcut and on side of dome above road.

DM-3: Bland quadrangle, on SE side of Del Medio II, 35°52'27"N 106°26'31"W. Exposures in roadcut.

DM-4: Valle Toledo quadrangle, on SE side of Del Medio III, 35°53'51"N 106°25'52"W. Large outcrops and obsidian float exposed on side of dome.

DM-5: Valle Toledo quadrangle, on NE side of Del Medio II, 35°55'45"N 106°25'39"W. Float and boulders exposed in roadcut.

DM-6: Same as DM-5.

DM-7: Valle Toledo quadrangle, on SW side of Del Medio III, 35°54'04"N 106°27'08"W. Exposures in roadcut.

DM-8: Valle Toledo quadrangle, on N side of Del Medio III, 35°54'37"N 106°26'47"W. Exposures in roadcut.

DM-9: Valle Toledo quadrangle, on NW side of Del Medio II, 35°55'36"N 106°27'22"W. Exposures in roadcut.

DM-10: Valle Toledo quadrangle, on E side of Del Medio I, 35°54'26"N 106°28'18"W. Float exposed in roadcut.

DM-11: Valle Toledo quadrangle, on W side of Del Medio I, 35°54'17"N 106°28'47"W. Float exposed in roadcut.

DA-1: Valle Toledo quadrangle, on S side of Del Abrigo I, 35°55'23N 106°29'00"W. Exposures in roadcut.

DA-2: Valle Toledo quadrangle, on W-SW side of Del Abrigo I, 35°55'53"N 106°29'11"W. Exposures in roadcut and talus slope.

DA-3: Same as DA-2.

APPENDIX A (continued)

DA-4: Valle Toledo quadrangle, on SE side of Del Abrigo I, 35°55'40"N 106°28'16"W. Exposures in roadcut.

DA-5: Valle Toledo quadrangle, on N-NW side of Del Abrigo I, 35°56'15"N 106°28'44"W. Exposures in roadcut.

DA-6: Valle Toledo quadrangle, near the center of Del Abrigo III, 35°56'48"N 106°28'55"W. Exposures in roadcut and large boulders littering hillside.

DA-7: Valle Toledo quadrangle, on S side of Del Abrigo III, 35°56'37"N 106°28'58"W. Exposures in roadcut and boulders along road.

DA-8: Valle Toledo quadrangle, on N-central part of Del Abrigo II, 35°55'53"N 106°29'08"W. Exposures in roadcut and boulders along road.

SR-1: Valle San Antonio quadrangle, on SW side of Santa Rosa I, 35°56'30"N 106°31'06"W. Exposures in roadcut and float on hillside.

SR-2: Valle San Antonio quadrangle, near the center of Santa Rosa I, 35°56'49"N 106°30'05"W. Float on hillside and in roadcut.

SR-3: Same as SR-2.

SR-4: Valle San Antonio quadrangle, on NW side of Santa Rosa I, 35°57'15"N 106°30'28"W. Exposures in roadcut.

SR-5: Valle Toledo quadrangle, near the center of Santa Rosa II, 35°57'38"N 106°29'53"W. Exposures in roadcut and boulders covering hilltop.

SR-6: Same as SR-5.

SR-7: Same as SR-5.

SR-8: Valle Toledo quadrangle, at center of Santa Rosa II, 35°57'47"N 106°29'51"W. Exposures in roadcut and boulders along road.

S-1: Valle San Antonio quadrangle, on SE side of Seco, 35°56'36"N 106°34'06"W. Exposures in roadcut.

S-2: Valle San Antonio quadrangle, at the peak of Seco (9931 ft.), 35°57'00"N 106°34'27"W. Exposures in roadcut and outcrops.

APPENDIX A (continued)

S-3: Valle San Antonio quadrangle, on SE side of Seco, 35° 56'32"N 106° 33'59"W. Exposures in roadcut and outcrops.

S-4: Same as S-3.

S-5: Valle San Antonio quadrangle, on E-SE side of Seco, 35° 56'32"N 106° 33'44"W. Exposures in roadcut.

S-6: Valle San Antonio quadrangle, on W-NW side of Seco, 35° 57'08"N 106° 35'08"N. Exposures in roadcuts and float on hillside.

S-7: Valle San Antonio quadrangle, on W side of Seco, 35° 56'50"N 106° 35'20"W. Exposures in roadcut.

SL-1: Valle San Antonio quadrangle, on W-SW side of San Luis, 35° 56'44"N 106° 32'59"W. Outcrops and exposures in roadcuts.

SL-2: Same as SL-1.

SL-3: Valle San Antonio quadrangle, on S side of San Luis, 35° 56'20"N 106° 32'30"W. Boulders exposed on hillside above road.

SL-4: Valle San Antonio quadrangle, on E side of San Luis, 35° 56'56"N 106° 31'43"W. Exposures in roadcut.

SL-5: Valle San Antonio quadrangle, on N side of San Luis, 35° 57'22"N 106° 32'05"W. Exposures in roadcut and float on hillside.

SA-1: Seven Springs quadrangle, on S end of San Antonio I, on U.S. Forest Service rd. 106, 35° 55'10"N 106° 38'21"W. Exposure in excavation on W side of road.

SA-2: Seven Springs quadrangle, on S end of San Antonio I, on U.S. Forest Service rd. 106, 35° 54'03"N 106° 38'05"W. Exposure in roadcut on E side of road.

SA-3: Valle San Antonio quadrangle, on N side of San Antonio I, 35° 57'23"N 106° 36'32"W. Outcrops and boulders exposed on hillside.

SA-4: Valle San Antonio quadrangle, on E side of San Antonio II, 35° 56'30"N 106° 35'45"W. Large outcrops 20 - 30 m above road and boulders floating down hillside.

APPENDIX A (continued)

SA-5: Same as SA-4.

SA-6: Same as SA-4.

SA-7: Valle San Antonio quadrangle, central to E-central side of San Antonio I, 35°56'06"N 106°36'37"W. Exposures in roadcuts and outcrops.

SA-8: Same as SA-7.

SA-9: Valle San Antonio quadrangle, on E side of San Antonio I, 35°55'52"N 106°36'06"W. Exposures in roadcut.

SA-10: Seven Springs quadrangle, on NW side of San Antonio I, 35°56'52"N 106°38'10"W. Outcrops and float on hillside.

SA-11: Seven Springs quadrangle, on W side of San Antonio I, 35°56'21"N 106°38'38"W. Exposures on flow front of dome.

SA-12: Seven Springs quadrangle, on W-SW side of San Antonio I, 35°55'11"N 106°39'01"W. Outcrops and boulder size float blocks.

LJ-1: Bland quadrangle, on E-NE side of La Jara, 35°51'21"N 106°29'36"W. Large outcrops on side of dome.

SM-1: Redondo Peak quadrangle, on SE side of South Mountain, on E Fork Jemez River, 35°49'56"N 106°30'32"W. Outcrops on N side of river.

SM-2: Redondo Peak quadrangle, on S side of South Mountain, 35°48'59"N 106°31'23"W. Outcrops and float on E side of river.

SM-3: Redondo Peak quadrangle, on S side of South Mountain, on state highway 4, 35°48'58"N 106°32'00"W. Exposure in roadcut on N side of highway.

SM-4: Same as SM-3.

SM-5: Redondo Peak quadrangle, on W end of South Mountain, on state highway 4, 35°49'43"N 106°35'25"W. Exposure in roadcut on N side of highway.

APPENDIX A (continued)

SM-6: Redondo Peak quadrangle, on W end of South Mountain, 35°48'34"N 106°35'11"W. Large outcrops on N side of road at intersection.

SM-7: Redondo Peak quadrangle, on W end of South Mountain, on state highway 4, 35°49'07"N 106°35'24"W. Outcrops and large float blocks on N side of highway.

SM-9: Redondo Peak quadrangle, on W end of South Mountain, on McCauley Hot Springs trail, 35°48'56"N 106°36'37"W. Outcrops in cliffs to S of trail.

SM-10: Redondo Peak quadrangle, on W end of South Mountain, on Banco Bonito campground road, 35°49'09"N 106°36'21"W. Outcrops on hillside to E of road.

BB-1: Same as SM-9

VC1-R: From VC-1 drillcore, depth = 485 ft.

VC1-BB: From VC-1 drillcore, depth = 578 ft.

APPENDIX B

HAND SAMPLE DESCRIPTIONS

This appendix contains field descriptions of hand samples collected for this study. Also included are brief statements concerning alteration.

APPENDIX B (continued)

DM-0: Aphyric obsidian; rare spherulites (< 1mm).

DM-1: Extremely pumiceous white rhyolite; very rare sanidine phenocrysts (euhedral, < 2mm), glassy. Very sparse brownish oxidation spots.

DM-2: Slightly pumiceous, pink, sparsely porphyritic rhyolite; approximately 5% phenocrysts of mostly sanidine (euhedral, 1-2mm) with minor quartz (subhedral, < 2mm). Brownish oxidation spots fairly common, otherwise unaltered.

DM-3: Dense, flow banded, purple to pink, sparsely porphyritic rhyolite; approximately 5% phenocrysts of mostly sanidine (2-3mm, euhedral), with minor rose quartz (< 2mm, euhedral to subhedral) and rare biotite (< 2mm, euhedral). No visible alteration.

DM-4: Porphyritic obsidian; approximately 5% phenocrysts of dominantly sanidine (< 2mm, euhedral) with lesser quartz (< 2mm, subhedral to euhedral). No visible alteration.

DM-5: Aphyric, faintly flow banded obsidian; very rare spherulites (< 1mm).

DM-6: Extremely pumiceous, white, aphyric rhyolite; brownish oxidation fairly pervasive, some devitrification evident.

DM-7: Pumiceous, off-white, sparsely porphyritic rhyolite; approximately 5-7% phenocrysts of dominantly sanidine (1-3mm, euhedral) with subordinate quartz (< 2mm, subhedral), glassy. Sparse brownish oxidation.

DM-8: Porphyritic obsidian; approximately 4-5% phenocrysts of sanidine (< 2mm, euhedral) and quartz (1-2mm, subhedral). Rare spherulites (1-2 mm).

DM-9: Aphyric obsidian; very rare spherulites (< 1mm).

DM-10: Aphyric obsidian; rare spherulites (< 1mm).

DM-11: Aphyric obsidian; rare spherulites (< 1mm).

APPENDIX B (continued)

DA-1: Slightly pumiceous, light grey to pinkish grey, porphyritic rhyolite; approximately 10% phenocrysts of subequal sanidine/plagioclase (1-3 mm, euhedral) and quartz + rose quartz (< 2mm, subhedral) with minor biotite (< 2mm, euhedral). No visible alteration.

DA-2: Slightly pumiceous, light grey, porphyritic rhyolite; phenocryst assemblage as in DA-1. Brownish oxidation fairly pervasive, biotites altered.

DA-3: Dark grey porphyritic rhyolite; phenocryst assemblage as in DA-1. Sparse brownish oxidation spots, biotites slightly altered.

DA-4: Identical to DA-1. Brown oxidation spots common, biotites altered.

DA-5: Identical to DA-3. Very sparse brownish oxidation spots.

DA-6: Moderately pumiceous, off-white, porphyritic rhyolite. approximately 10-15% phenocrysts of subequal sanidine/plagioclase (< 3mm, euhedral) and quartz + rose quartz (< 2mm, subhedral to euhedral) with minor biotite (1-2mm, euhedral), glassy. Sparse yellowish-brown oxidation.

DA-7: Identical to DA-6. Very rare yellowish-brown oxidation.

DA-8: Identical to DA-3. Sparse brownish oxidation spots.

SR-1: Flow banded, light grey to grey, porphyritic rhyolite; approximately 15-20% phenocrysts of dominantly sanidine/plagioclase (1-3mm, euhedral) with lesser quartz + rose quartz (1-2mm, subhedral) and biotite (< 2mm, euhedral). Rare brown oxidation spots.

SR-2: Slightly pumiceous, light grey, porphyritic rhyolite; phenocryst assemblage as in SR-1, glassy. Sparse brownish oxidation.

SR-3: Moderately pumiceous, grey, porphyritic rhyolite; phenocryst assemblage as in SR-1, glassy. No visible alteration.

APPENDIX B (continued)

SR-4: Slightly pumiceous, flow banded, light grey, porphyritic rhyolite; phenocryst assemblage as in SR-1, glassy. Very sparse brownish oxidation.

SR-5: Moderately pumiceous, light grey, porphyritic rhyolite; approximately 20% phenocrysts of subequal sanidine/plagioclase (1-4mm, euhedral) and rose quartz (1-5mm, subhedral to euhedral) with minor biotite (1-3mm, euhedral), glassy. Rare brownish oxidation.

SR-6: Identical to SR-5.

SR-7: Identical to SR-5.

SR-8: Identical to SR-5.

S-1: Dense, greyish-white, porphyritic rhyolite; approximately 20% phenocrysts of dominantly rose quartz (< 3mm, subhedral to euhedral) with lesser sanidine/plagioclase (1-3mm, euhedral) and minor biotite (1-2mm, euhedral). Some alteration of biotites evident.

S-2: Identical to S-1. Brownish oxidation fairly pervasive, biotites altered.

S-3: Identical to S-1. Biotites slightly altered.

S-4: Identical to S-1. Rare brownish oxidation, most biotites altered, quartz rich inclusion (xenolith?).

S-5: Slightly pumiceous, cream white, porphyritic rhyolite; phenocryst assemblage as in S-1, glassy. Rare brownish oxidation.

S-6: Identical to S-1. Pervasive brownish oxidation, most biotites altered.

S-7: Dense, grey, porphyritic rhyolite; phenocryst assemblage as in S-1. Extremely rare brownish oxidation.

SL-1: Pumiceous, cream white, porphyritic rhyolite; approximately 20-25% phenocrysts of subequal sanidine/plagioclase (2-3mm, euhedral) and quartz (1-2mm, subhedral to anhedral) with minor biotite (1-2mm, euhedral) and rare hornblende (1-2mm, euhedral), glassy. Extremely rare brown oxidation spots.

APPENDIX B (continued)

SL-2: Identical to SL-1.

SL-3: Pumiceous, greyish white, porphyritic rhyolite; phenocryst assemblage as in SL-1. Sparse brown oxidation spots, slight alteration of some biotites.

SL-4: Identical to SL-3. Extremely sparse brownish oxidation.

SL-5: Identical to SL-3. Fairly common brownish oxidation.

SA-1: Pumiceous, white to greyish, faintly flow banded, porphyritic rhyolite; approximately 25% phenocrysts of subequal sanidine/plagioclase (2-4mm, euhedral) and rose quartz (2-4mm, subhedral), with minor biotite (1-3mm, euhedral) and hornblende (1-2mm, euhedral), glassy. Very rare brownish oxidation.

SA-2: Slightly pumiceous, grey to dark grey, flow banded, porphyritic rhyolite; phenocryst assemblage as in SA-1 except for less biotite. Extremely rare brownish oxidation.

SA-3: Pumiceous, greyish white, porphyritic rhyolite; approximately 25% phenocrysts of dominantly quartz + rose quartz (1-4mm, subhedral to anhedral) with lesser sanidine/plagioclase (2-4mm, euhedral), minor biotite (1-3mm, euhedral) and rare hornblende (1-2mm, euhedral), glassy. No visible alteration.

SA-4: Pumiceous, pinkish purple, porphyritic rhyolite; approximately 25-30% phenocrysts of subequal sanidine/plagioclase (2-6mm, euhedral) and quartz + rose quartz (2-5mm, subhedral) with minor biotite (1-4mm, euhedral) and hornblende (1-2mm, euhedral). Minor Fe staining around biotites.

SA-5: Identical to SA-4.

SA-6: Identical to SA-4.

APPENDIX B (continued)

SA-7: Pumiceous, white, porphyritic rhyolite; approximately 20-25% phenocrysts of dominantly sanidine/plagioclase (2-4mm, euhedral) with lesser quartz + rose quartz (1-4mm, subhedral to anhedral) and minor biotite (1-3mm, euhedral) and hornblende (1-2mm, euhedral), glassy. Some minor brownish oxidation, some alteration of biotites.

SA-8: Identical to SA-7. No visible alteration.

SA-9: Identical to SA-1. Rare brown oxidation.

SA-10: Identical to SA-3. No visible alteration.

SA-11: Massive, grey, porphyritic rhyolite; phenocryst assemblage as in SA-1. Rare brownish oxidation.

LJ-1: Pumiceous, off-white, porphyritic rhyolite; approximately 20-25% phenocrysts of subequal sanidine/plagioclase (1-4mm, euhedral) and quartz + rose quartz (1-2mm, subhedral) with minor biotite (1-2mm, euhedral) and hornblende (1-2mm, euhedral), glassy. No visible alteration.

SM-1: Pumiceous, grey, porphyritic rhyolite; approximately 20-25% phenocrysts of subequal sanidine/plagioclase (1-4mm, euhedral, commonly exhibiting a purplish schiller) and rose quartz (2-3mm, anhedral) with minor biotite (1-3mm, euhedral) and hornblende (1-2mm, euhedral), glassy. Fair amount of brownish oxidation.

SM-2: Slightly pumiceous, pinkish grey to grey, flow banded, porphyritic rhyolite; approximately 25% phenocrysts of dominantly sanidine/plagioclase (3-5mm, euhedral, commonly exhibiting purplish schiller) with lesser quartz + rose quartz (2-4mm, anhedral to subhedral) and minor biotite (1-2mm, euhedral). No visible alteration.

SM-3: Dark grey to black, vitrophyric, porphyritic rhyolite; phenocryst assemblage as in SA-1 except for lack of purplish schiller in sanidines, glassy. Minor Fe staining.

SM-4: Identical to SM-3.

APPENDIX B (continued)

SM-5: Extremely pumiceous, white, porphyritic rhyolite; approximately 25% phenocrysts of subequal sanidine/plagioclase (1-4mm, euhedral) with lesser quartz + rose quartz (1-4mm, subhedral) and minor biotite (1-3mm, euhedral, often in "books") and hornblende (< 2mm, euhedral), glassy. No visible alteration.

SM-6: Identical to SM-5.

SM-7: Identical to SM-5.

SM-9: Identical to SM-5. Slight brownish oxidation.

SM-10: Identical to SM-5 only slightly more biotite. Extremely sparse brownish oxidation.

BB-1: Porphyritic obsidian; approximately 15% phenocrysts of dominantly quartz (1-3mm, subhedral) with lesser sanidine/plagioclase (1-3mm, euhedral) and biotite (1-2mm, euhedral). Very sparse brown oxidation spots.

VC1-BB: Identical to SM-8. Small fractures filled with clays(?), minor Fe staining. NOTE: This sample from the VC-1 drillcore.

VC1-R: Porphyritic obsidian; phenocryst assemblage as in BB-1. Small fractures filled with clays(?), otherwise no visible alteration. NOTE: This sample from the VC-1 drillcore.

APPENDIX C

DETAILED PETROGRAPHIC DESCRIPTIONS

In this appendix detailed petrographic descriptions of individual samples are given. The thin sections discussed here are those for which modes are given in Table 2 and are considered representative of the range of lithologies present in the Valle Grande Member. Phenocryst phases present in trace amounts and not listed in Table 2 are presented in order of decreasing abundance. Samples are arranged in order of decreasing age.

APPENDIX C (continued)

DM-1

Groundmass: glassy, extremely pumiceous, vesicles 0.02-2.1mm, stretched vesicles common, perlitic cracks in areas. Phenocrysts: Quartz - anhedral to subhedral, broken, resorbed, 0.1-1.1mm; Sanidine - euhedral to subhedral, rarely broken, carlsbad twinning, 0.2-1.2mm; Plagioclase - subhedral, polysynthetic twinning, rare, 0.2-0.4mm; Biotite - euhedral, reddish brown, strongly pleochroic, rare, 0.1-0.2mm; Oxides - anhedral to subhedral, exsolution very common, rare, 0.02-0.2mm; Zircon - euhedral, colorless, oxide inclusions common, very rare, 0.02-0.4mm; Hornblende - subhedral, brown, pleochroic, very rare, 0.3mm; Clinopyroxene - anhedral, very rare, 0.2mm. Porphyritic, glomeroporphyritic.

DA-6

Groundmass: glassy, slightly pumiceous, vesicles 0.3-3.0mm, some stretched vesicles present, perlitic cracks fairly common, rare spherulites 0.01-0.6mm. Phenocrysts: Sanidine - euhedral to subhedral, some broken and fractured, few resorbed, carlsbad twinning, 0.2-1.8mm; Quartz - subhedral to euhedral, commonly broken, fractured, and resorbed, occasional pyramidal terminations, 0.3-2.0mm; Plagioclase - euhedral to subhedral, rarely broken and resorbed, polysynthetic twinning, 0.2-2.5mm; Biotite - euhedral, brown to reddish brown, strongly pleochroic, 0.2-1.1mm; Hornblende - subhedral to euhedral, brown, pleochroic, 0.2-0.4mm; Oxides - anhedral to subhedral, all exsolved, 0.04-0.4mm; Zircon - euhedral, colorless, rare, 0.04-0.1mm; Allanite - euhedral, non-metamict, brown, pleochroic, very rare, 0.1mm; Clinopyroxene - euhedral, very rare, 0.2mm. Porphyritic, glomeroporphyritic.

SR-1

Groundmass: totally devitrified, spherulitic (spherulites 0.1-0.5mm), non-vesicular. Phenocrysts: Sanidine - euhedral to subhedral, few broken and fractured, carlsbad twinning, occasional sector zoning, 0.4-3.5mm; Quartz - subhedral to euhedral, broken, often resorbed, occasional bipyramids, 0.3-2.5mm; Plagioclase - euhedral to subhedral, polysynthetic twinning, few zoned (oscillatory and core-rim), 0.2-0.8mm; Biotite - euhedral, reddish brown, strongly pleochroic, 0.3-0.8mm; Hornblende - euhedral, brown, 0.2-0.3mm; Oxides - anhedral to subhedral, commonly exsolved, 0.05-0.6mm; Zircon - euhedral to subhedral, colorless, 0.02-0.1mm;

APPENDIX C (continued)

Allanite - euhedral, brown, pleochroic, non-metamict, 0.2-0.1mm; Apatite - euhedral, colorless, as inclusions in oxides, very rare, 0.04-0.07mm. Glomeroporphyritic.

S-5

Groundmass: glassy, pumiceous, stretched vesicles common, vesicles 0.1-2mm, perlitic cracks in areas, rare spherulites 0.1-0.3mm. Phenocrysts: Quartz - euhedral to subhedral, fractured and broken commonly, resorbed, few bipyramidal outlines, 0.3-2.0mm; Sanidine - euhedral to subhedral, few broken, occasionally resorbed, carlsbad twinning, 0.2-3.5mm; Plagioclase - euhedral, rarely broken, polysynthetic twinning common, occasional core-rim and oscillatory zoning, 0.2-1.0mm; Biotite - euhedral, brown, strongly pleochroic, 0.2-0.6mm; Hornblende - subhedral, brown, pleochroic, 0.2-0.6mm; Oxides - anhedral, most exsolved, some resorbed(?), 0.04-0.5mm; Zircon - euhedral to subhedral, colorless, rare, 0.02-0.04mm; Apatite - euhedral, colorless, as inclusions in oxides, very rare, 0.02mm. Porphyritic, glomeroporphyritic.

SR-7

Groundmass: glassy, slightly pumiceous, stretched vesicles, vesicles 0.1-1.8mm, perlitic cracks fairly common, rare spherulites 0.08-0.5mm. Phenocrysts: Sanidine - euhedral to subhedral, few broken and resorbed, carlsbad twinning, 0.3-5mm; Quartz - subhedral to anhedral, commonly fractured and broken, strongly resorbed, few bipyramidal, 0.3-2.4mm; Plagioclase - euhedral to subhedral, few broken, polysynthetic twinning, 0.2-1.0mm; Hornblende - euhedral, brown, pleochroic, 0.2-0.8mm; Biotite - euhedral, brown to reddish brown, strongly pleochroic, 0.3-1.2mm; Oxides - anhedral to subhedral, commonly exsolved, 0.1-0.4mm; Zircon - euhedral to subhedral, colorless, 0.02-0.04mm; Allanite - euhedral to subhedral, brown to dark brown, pleochroic, non-metamict, 0.1-0.6mm. Porphyritic, glomeroporphyritic.

SL-1

Groundmass: glassy, moderately pumiceous, stretched vesicles, vesicles 0.2-1.5mm, perlitic cracks common, rare spherulites 0.05-0.6mm. Phenocrysts: Sanidine - euhedral, often fractured, few resorbed, carlsbad twinning common, 0.3-3.0mm; Quartz - subhedral to

APPENDIX C (continued)

euhedral, commonly fractured, strongly resorbed, occasional pyramidal outlines, 0.5-4.2mm; Plagioclase - euhedral, polysynthetic twinning very common, few zoned core-rim, 0.3-2.1mm; Biotite - euhedral, brown to reddish brown, strongly pleochroic, 0.3-1.2mm; Hornblende - euhedral, brown to green, pleochroic, 0.2-0.5mm; Oxides - anhedral, exsolved, occasional hematite(?) alteration rims, 0.1-0.4mm; Zircon - subhedral to euhedral, colorless, 0.04-0.15mm; Allanite - euhedral, brown, pleochroic, non-metamict, rare, 0.3mm. Porphyritic.

SA-2

Groundmass: glassy, moderately pumiceous, stretched vesicles common, vesicular, vesicles 0.03-2.0mm, rare perlitic cracks. Phenocrysts: Sanidine - euhedral to subhedral, occasionally fractured and broken, rarely resorbed, carlsbad twinning, 0.4-2.5mm; Quartz - subhedral, commonly fractured, broken, and resorbed, 0.4-2.2mm; Plagioclase - euhedral to subhedral, few broken, few resorbed, polysynthetic twinning, zoning (oscillatory and core-rim), 0.4-1.7mm; Biotite - euhedral, light to dark brown, strongly pleochroic, 0.1-1.1mm; Hornblende - euhedral, brown to greenish brown, pleochroic, 0.4-1.0mm; Oxides - anhedral to subhedral, commonly exsolved, 0.1-0.5mm; Zircon - euhedral to subhedral, colorless, often with apatite(?) inclusions, 0.02-0.3mm; Allanite - euhedral to subhedral, brown to deep brown, pleochroic, non-metamict, 0.2-0.6mm; Apatite - euhedral, colorless, as inclusions in oxides, rare, 0.02-0.08mm; Clinopyroxene - subhedral, occasionally with hornblende reaction rims, rare, 0.3-0.4mm; Orthopyroxene - subhedral, hornblende reaction rims, very rare, 0.4mm. Porphyritic, glomeroporphyritic.

LJ-1

Groundmass: glassy, pumiceous, stretched vesicles, vesicular, vesicles 0.2-1.8mm, perlitic cracks fairly common. Phenocrysts: Sanidine - euhedral to subhedral, commonly fractured, resorbed, carlsbad twinning, 0.4-4.2mm; Quartz - subhedral, commonly broken, fractured, a few strongly resorbed, occasionally bipyramidal, 0.4-3.9mm; Plagioclase - euhedral to subhedral, broken, occasionally resorbed, polysynthetic twinning, common oscillatory and core-rim zoning, 0.3-2.8mm; Biotite - euhedral, brown to reddish brown, strongly pleochroic, 0.2-1.1mm; Hornblende - euhedral, greenish brown, pleochroic, 0.1-0.8mm; Oxides - anhedral to subhedral,

APPENDIX C (continued)

exsolved, 0.1-0.4mm; Zircon - euhedral to subhedral, colorless, 0.01-0.2mm; Allanite - subhedral, brown, pleochroic, non-metamict, rare, 0.15-0.4mm; Apatite - euhedral, colorless, enclosed and associated with oxides, very rare, 0.01-0.04mm. Porphyritic, glomeroporphyritic.

SM-5

Groundmass: glassy, extremely pumiceous, stretched vesicles, vesicles 0.02-0.1mm, rare perlitic cracks. Phenocrysts: Sanidine - euhedral to subhedral, often fractured, few resorbed, carlsbad twinning, 0.7-4.2mm; Quartz - subhedral, often fractured, broken, and resorbed, rare pyramidal outlines, 0.3-4.4mm; Plagioclase - euhedral to subhedral, few resorbed, polysynthetic twinning, many zoned oscillatory and core-rim, 0.4-2.4mm; Biotite - euhedral, brown, strongly pleochroic, a few showing bent cleavages, 0.2-1.3mm; Hornblende - subhedral, green to brown, pleochroic, 0.1-0.8mm; Oxides - anhedral, usually exsolved, few resorbed(?), 0.1-0.6mm; Zircon - euhedral to subhedral, colorless, 0.01-0.6mm; Allanite - subhedral, reddish brown, pleochroic, non-matamict, rare, 0.06-0.4mm; Apatite - euhedral, colorless, enclosed in oxides and biotite, very rare, 0.03-0.4mm; Clinopyroxene - subhedral to anhedral, hornblende alteration rims, very rare, 0.2-0.3mm. Porphyritic, glomeroporphyritic.

SA-6

Groundmass: totally devitrified, sperulitic, spherulites 0.2-0.8mm, vesicular, vesicles 0.6-1.2mm. Phenocrysts: Quartz - subhedral to anhedral, commonly fractured, broken,and resorbed, few bipyramidal outlines, 0.4-3.4mm; Sanidine - euhedral to subhedral, occasionally fractured and resorbed, carlsbad twinning, 0.8-4.1mm; Plagioclase - euhedral to subhedral, few resorbed, polysynthetic twinning, commonly zoned oscillatory and core-rim, 0.4-3.8mm; Biotite - euhedral, reddish brown, strongly pleochroic, a few with oxide rims, 0.1-1.4mm; Hornblende - euhedral to subhedral, greenish brown, pleochroic, 0.1-0.75mm; Oxides - anhedral, exsolved, 0.04-0.6mm; Zircon - euhedral to subhedral, colorless, 0.1-0.2mm; Allanite - euhedral to subhedral, brown to reddish brown, pleochroic, non-metamict, 0.1-0.4mm; Apatite - euhedral, colorless, enclosed in oxides, rare, 0.02mm; Clinopyroxene - anhedral, alteration rims of hornblende + oxides, rare, 0.2mm. Porphyritic, glomeroporphyritic.

APPENDIX D

ANALYTICAL METHODS

Sample Collection

Several kilograms of each sample were collected. Samples were inspected in the field and trimmed of weathering rinds and any visible alteration.

Preparation of Rock Powders

Powdered samples were used for both x-ray fluorescence (XRF) and instrumental neutron activation analysis (INAA). Upon returning to the lab approximately 500-600 grams of rock was selected to represent each sample. Rock powders were prepared by first breaking samples up into pieces <2 centimeters in size using a hammer and steel plate. Samples were placed in plastic bags during this step to insure that phenocrysts were not preferentially concentrated. This was especially important for very pumiceous samples. At this point samples were again inspected for signs of alteration and any pieces which were suspect were discarded. Samples were then crushed to pieces <4-5 millimeters in size using a small jaw crusher with porcelain plates. All surfaces in contact with sample were carefully cleaned with acetone and compressed air between each sample. Next, samples were reduced to -200 mesh (~0.004mm) by

APPENDIX D (continued)

running them in a TEMA shatterbox with a tungsten carbide cannister for 60-90 seconds. As before, all surfaces coming into contact with sample were carefully cleaned with acetone and compressed air between each sample. At this point the 500-600 grams of powdered sample was mechanically mixed and split by hand using the cone and quarter method to produce an approximately 200 gram final aliquot for analysis.

X-Ray Fluorescence Analysis

Samples were analyzed for both major elements and trace elements by XRF. Analytical methods and sample preparation procedures for XRF are outlined in Norrish and Hutton (1969) and Norrish and Chappell (1977).

Fused discs were prepared for major element analysis. Approximately 0.5 grams of powdered sample was mixed with ~2.68 grams of lithium tetraborate - lanthanum oxide flux (Spectroflux 105) and a few grains of ammonium nitrate (to insure oxidation of iron) in a platinum crucible. The mixture was then fused over a propane burner for approximately 5 minutes after which it was heated over a hotter burner (~1,000 °C) for at least 5 minutes longer. The molten mixture was then chilled in a mold held at 450 °C and allowed to cool to room

APPENDIX D (continued)

temperature over a period of several hours. Experience has shown that higher heating temperatures and longer heating times during the fusion process reduces the problem of breakage during cooling when dealing with high-silica rhyolite samples.

Pressed powder pellets were prepared for trace element analysis. Approximately 7.5 grams of powdered sample was mixed with 8 drops of a polyvinyl alcohol solution (a binder) and pressed into a pellet with a boric acid backing cup using a die, plunger, and hydraulic press. Pellets were pressed at 7.5 tons for 30 seconds. Experience has shown that higher pressures causes problems of exfoliation and cracking of the pellet when dealing with high-silica rhyolites.

XRF analyses were performed on a Rigaku model 3062 machine. kV and Ma settings as well as slit, filter, and crystals used varied according to the elements being analyzed. All data reduction was performed by an on-line DEC computer. A large number of well characterized standards were used to calibrate XRF runs.

Analytical errors were calculated by multiple runs on triplicates of three separate samples. The elements analyzed by XRF as well as the calculated accuracy and precision is given in Appendix G.

APPENDIX D (continued)

Instrumental Neutron Activation Analysis

Trace elements including the REE's were analyzed by INAA using methods and computer programs described by Jacobs et al. (1977) and Lindstrom and Korotev (1982).

Between 60 and 145 milligrams of each sample was weighed to $\pm$0.0001 gram, placed in a high purity quartz vial, and sealed off by melting the end. The vial containing the sample was then weighed to $\pm$0.0001 gram and all vials were were wrapped in a foil holder for irradiation. The weight and physical characteristics of each vial as well as their relative position in the foil holder were used to identify them after they were returned from irradiation. Samples were irradiated at the Research Reactor Facility at the University of Missouri for ~36 hours at an average neutron flux of $2.23 * 10^{13}$ $n \cdot cm^{-2} \cdot s^{-1}$.

Counts were taken on each sample at intervals of 7 and 40 days after irradiation using a Nuclear Data 6620 system in conjunction with two high purity germanium detectors. Final data reduction was done by hand. Peaks or combinations of peaks giving the values closest to known values for USGS standard G-2, which was run as an unknown, were calculated. These peaks were then used to obtain the final data for the samples being analyzed on

APPENDIX D (continued)

the same run. USGS standard BCR-1 was used to calibrate for Na_2O, whereas all other elements were calibrated to NBS 1633a (fly ash).

Accuracy and precision of the analytical data was calculated from multiple irradiations and runs of G-2 and BCR-1 as well as from triplicates and duplicates of samples run as unknowns. Elements analyzed for by INAA as well as the calculated accuracy and precision is given in Appendix G.

Electron Microprobe Analysis

Electron microprobe analysis was performed at Los Alamos National Laboratory in Los Alamos, New Mexico using a fully automated Cameca microprobe. Wavelength dispersive analysis and data reduction was performed online by a DEC computer using the data reduction scheme described by Bence and Albee (1968). Energy dispersive analysis was provided by an online Tracor-Northern system. Electron beam accelerating voltage was set at 15 kV and sample current was set at 20 Ma. The beam size was set at 5 microns. 15 second counts were used for all elements except for F and Cl for which 60 second counts were used. A well characterized set of intra-laboratory standards were used for calibration. Polished sections

APPENDIX D (continued)

used for microprobe analysis were prepared by Dave Mann of Mann Petrographic in Los Alamos.

Petrographic Analysis

Petrographic analyses as well as point counting were done using an Olympus research microscope (model BH-2) in conjunction with a Swift 31602 automatic point counter. Thin section preparation was begun at Los Alamos National Laboratories during August of 1986. Rock chips were cut, mounted, taken down to 0.05-0.06mm thickness, and left uncovered. These were examined and 10 sections representing most of the dated eruptive units of the Valle Grande Member were selected for microprobe analysis. Sections selected for microprobe work were polished and others were taken down to proper thickness (0.03mm), stained for sanidine, and cover slipped by Mann Petrographic in Los Alamos. A total of 31 sections were prepared which represented all dated units, with the exception of Del Medio I, were examined for general petrographic descriptions. Del Medio I was omitted because all samples collected were aphyric obsidians. Detailed petrographic descriptions and point counts of 10 sections from all dated eruptive units (except Del Medio I) were also done. Between 538 and 724 points were

APPENDIX D (continued)

counted for each section. Samples varied greatly in vesicularity with some being only slightly vesicular and others containing up to ~30-40% vesicles. Since the goal of modal analysis was to estimate relative percentages of various phenocrysts as well as the total magmatic (vesicle free) phenocryst contents the point counts did not take into account vesicles when present, only glass and phenocrysts were counted. Thus, there was no correction to be made for vesicle content.

APPENDIX E

MINERAL CHEMISTRY

In this appendix major element chemistry, cation proportions, and end-member compositions of phenocrysts along with several co-existing glass analyses determined by electron microprobe are given. Analyses are grouped according to type. Within each group analyses are listed in order of decreasing age. Individual analyses are designated by sample number (e.g., DM-3, SR-8), followed by type of analysis (S = sanidine, P = plagioclase, B = biotite, H = hornblende, M = magnetite, I = ilmenite, and G = glass), number of analysis (1, 2, 3, etc:), and finally a designation for the area of the phenocryst analyzed (C = core, I = intermediate, R = rim) for sanidine and plagioclase. All biotite and hornblende analyses are rim compositions.

Table E.1

Sanidine Analyses

Oxides (wt.%)	DM3-S1C	DM3-S1I	DM3-S1R	DM3-S2C
SiO_2	67.15	67.12	67.22	67.23
TiO_2	0.00	0.00	0.00	0.02
Al_2O_3	19.54	19.24	20.06	19.11
FeO	0.13	0.08	0.09	0.16
MgO	0.00	0.00	0.00	0.01
BaO	0.13	0.00	0.00	0.27
CaO	0.31	0.24	0.70	0.34
Na_2O	5.90	5.86	7.67	6.34
K_2O	7.86	8.24	5.38	7.77
TOTAL	101.02	100.77	101.12	101.24
Cation formula (based on 8 oxygens)				
Si	2.9832	2.9912	2.9611	2.9881
Ti	0.0000	0.0000	0.0000	0.0006
Al	1.0233	1.0104	1.0415	1.0010
Fe	0.0048	0.0029	0.0032	0.0059
Mg	0.0000	0.0000	0.0000	0.0003
Ba	0.0022	0.0000	0.0000	0.0047
Ca	0.0145	0.0116	0.0332	0.0162
Na	0.5078	0.5060	0.6554	0.5462
K	0.4457	0.4683	0.3022	0.4407
Calculated end members				
Or	45.902	47.461	30.490	43.693
Ab	52.293	51.282	66.078	54.144
An	1.535	1.216	3.392	1.652

Table E.1 (continued)

Sanidine Analyses

Oxides (wt.%)	DM3-S2R	DM3-S3C	DM3-S3R	DA6-S1R
SiO_2	67.28	67.34	67.66	67.22
TiO_2	0.00	0.02	0.00	0.03
Al_2O_3	19.17	19.43	19.31	18.90
FeO	0.13	0.13	0.09	0.07
MgO	0.01	0.00	0.00	0.00
BaO	0.04	0.20	0.16	0.11
CaO	0.27	0.34	0.27	0.22
Na_2O	5.80	6.07	5.93	5.09
K_2O	8.28	7.63	7.42	9.08
TOTAL	100.99	101.18	100.84	100.71
Cation formula (based on 8 oxygens)				
Si	2.9936	2.9863	3.0009	3.0048
Ti	0.0000	0.0008	0.0000	0.0011
Al	1.0054	1.0158	1.0094	0.9956
Fe	0.0047	0.0048	0.0032	0.0025
Mg	0.0003	0.0000	0.0001	0.0000
Ba	0.0006	0.0034	0.0028	0.0019
Ca	0.0129	0.0163	0.0128	0.0105
Na	0.5008	0.5221	0.5100	0.4409
K	0.4704	0.4320	0.4196	0.5178
Calculated end members				
Or	47.727	44.322	44.358	53.270
Ab	50.810	53.559	53.901	45.367
An	1.358	1.721	1.398	1.121

Table E.1 (continued)

Sanidine Analyses

Oxides (wt.%)	DA6-S2C	DA6-S2I	DA6-S2R	DA6-S3C
SiO_2	67.11	67.05	65.25	66.88
TiO_2	0.00	0.00	0.02	0.00
Al_2O_3	19.22	19.15	18.65	19.28
FeO	0.08	0.11	0.08	0.09
MgO	0.00	0.00	0.00	0.00
BaO	0.04	0.00	0.00	0.17
CaO	0.22	0.19	0.22	0.21
Na_2O	5.28	5.31	5.19	5.11
K_2O	9.43	9.49	8.86	9.24
TOTAL	101.37	101.30	98.27	100.98
Cation formula (based on 8 oxygens)				
Si	2.9883	2.9889	2.9913	2.9879
Ti	0.0000	0.0000	0.0006	0.0000
Al	1.0088	1.0062	1.0080	1.0154
Fe	0.0030	0.0041	0.0031	0.0034
Mg	0.0000	0.0000	0.0000	0.0000
Ba	0.0006	0.0000	0.0000	0.0028
Ca	0.0102	0.0089	0.0106	0.0102
Na	0.4563	0.4592	0.4618	0.4425
K	0.5356	0.5399	0.5180	0.5265
Calculated end members				
Or	53.363	53.510	52.257	53.565
Ab	45.470	45.522	46.587	45.022
An	1.062	1.021	1.116	1.078

Table E.1 (continued)

Sanidine Analyses

Oxides (wt.%)	DA6-S3R	DA6-S4R	DA6-S5R	SR4-S1R
SiO_2	66.82	66.57	66.58	67.01
TiO_2	0.02	0.00	0.00	0.00
Al_2O_3	19.10	19.05	18.69	19.05
FeO	0.00	0.06	0.09	0.05
MgO	0.00	0.00	0.00	0.00
BaO	0.11	0.07	0.02	0.02
CaO	0.22	0.18	0.17	0.19
Na_2O	5.32	5.07	5.09	5.29
K_2O	9.05	9.49	9.16	9.03
TOTAL	100.64	100.50	99.80	100.64
Cation formula (based on 8 oxygens)				
Si	2.9921	2.9905	3.0049	2.9974
Ti	0.0008	0.0000	0.0000	0.0000
Al	1.0079	1.0090	0.9943	1.0042
Fe	0.0000	0.0022	0.0032	0.0019
Mg	0.0000	0.0000	0.0000	0.0000
Ba	0.0019	0.0012	0.0003	0.0003
Ca	0.0106	0.0087	0.0084	0.0092
Na	0.4617	0.4420	0.4453	0.4588
K	0.5173	0.5440	0.5276	0.5157
Calculated end members				
Or	52.123	54.573	53.699	52.358
Ab	46.528	44.341	45.329	46.588
An	1.114	0.916	0.898	0.980

Table E.1 (continued)

Sanidine Analyses

Oxides (wt.%)	SR4-S2R	SR4-S3C	SR4-S3R	SR4-S4C
SiO_2	66.51	67.36	66.62	67.40
TiO_2	0.01	0.01	0.01	0.00
Al_2O_3	19.45	19.11	18.99	19.15
FeO	0.16	0.05	0.08	0.12
MgO	0.00	0.00	0.00	0.00
BaO	0.00	0.00	0.13	0.00
CaO	0.18	0.20	0.18	0.25
Na_2O	5.09	5.20	5.06	5.34
K_2O	9.06	8.93	9.04	8.67
TOTAL	100.47	100.86	100.12	100.92
Cation formula (based on 8 oxygens)				
Si	2.9813	3.0019	2.9972	3.0000
Ti	0.0004	0.0003	0.0003	0.0000
Al	1.0274	1.0036	1.0069	1.0047
Fe	0.0059	0.0019	0.0031	0.0045
Mg	0.0000	0.0000	0.0000	0.0000
Ba	0.0000	0.0000	0.0022	0.0000
Ca	0.0088	0.0095	0.0087	0.0117
Na	0.4426	0.4492	0.4415	0.4606
K	0.5183	0.5077	0.5192	0.4924
Calculated end members				
Or	53.400	52.490	53.387	50.996
Ab	45.608	46.444	45.403	47.706
An	0.951	1.025	0.937	1.257

Table E.1 (continued)

Sanidine Analyses

Oxides (wt.%)	SR4-S4R	SR4-S5C	S1-S1R	S1-S2C
SiO_2	66.91	66.99	67.42	66.38
TiO_2	0.00	0.03	0.00	0.02
Al_2O_3	19.25	19.21	19.22	19.25
FeO	0.09	0.08	0.20	0.07
MgO	0.00	0.00	0.00	0.01
BaO	0.00	0.00	0.22	0.05
CaO	0.20	0.20	0.22	0.21
Na_2O	5.25	5.29	5.51	5.71
K_2O	8.92	8.98	8.66	8.54
TOTAL	100.62	100.79	101.46	100.25
Cation formula (based on 8 oxygens)				
Si	2.9915	2.9916	2.9933	2.9812
Ti	0.0000	0.0009	0.0000	0.0005
Al	1.0145	1.0112	1.0058	1.0187
Fe	0.0032	0.0029	0.0074	0.0026
Mg	0.0000	0.0000	0.0000	0.0009
Ba	0.0000	0.0000	0.0038	0.0009
Ca	0.0095	0.0097	0.0106	0.0102
Na	0.4554	0.4581	0.4747	0.4970
K	0.5088	0.5120	0.4905	0.4895
Calculated end members				
Or	52.204	52.205	50.026	49.022
Ab	46.735	46.717	48.418	49.775
An	1.020	1.037	1.125	1.067

Table E.1 (continued)

Sanidine Analyses

Oxides (wt.%)	S1-S2R	S1-S3R	SR8-S1C	SR8-S1R
SiO_2	67.19	67.45	66.85	66.64
TiO_2	0.00	0.02	0.02	0.02
Al_2O_3	19.02	19.56	18.96	19.25
FeO	0.10	0.13	0.07	0.11
MgO	0.00	0.01	0.00	0.00
BaO	0.11	0.24	0.00	0.00
CaO	0.25	0.24	0.24	0.28
Na_2O	5.48	5.45	5.23	5.58
K_2O	8.58	8.58	8.89	8.15
TOTAL	100.73	101.66	100.26	100.03
Cation formula (based on 8 oxygens)				
Si	2.9996	2.9855	2.9992	2.9892
Ti	0.0000	0.0007	0.0007	0.0006
Al	1.0007	1.0206	1.0026	1.0175
Fe	0.0038	0.0046	0.0024	0.0042
Mg	0.0000	0.0004	0.0000	0.0000
Ba	0.0019	0.0041	0.0000	0.0000
Ca	0.0121	0.0111	0.0116	0.0135
Na	0.4742	0.4674	0.4549	0.4856
K	0.4890	0.4845	0.5087	0.4662
Calculated end members				
Or	49.997	50.047	52.119	48.253
Ab	48.487	48.289	46.608	50.259
An	1.280	1.196	1.232	1.447

Table E.1 (continued)

Sanidine Analyses

Oxides (wt.%)	SR8-S2C	SR8-S2R	SR8-S3R	SR8-S4R
SiO_2	66.80	66.60	67.21	66.34
TiO_2	0.00	0.00	0.00	0.00
Al_2O_3	19.13	19.01	19.40	19.22
FeO	0.07	0.12	0.12	0.13
MgO	0.00	0.00	0.00	0.00
BaO	0.00	0.00	0.00	0.00
CaO	0.26	0.28	0.26	0.28
Na_2O	5.53	5.51	5.63	5.68
K_2O	8.50	8.15	8.70	8.48
TOTAL	100.30	99.67	101.32	100.14
Cation formula (based on 8 oxygens)				
Si	2.9929	2.9972	2.9852	2.9815
Ti	0.0000	0.0000	0.0000	0.0000
Al	1.0104	1.0086	1.0156	1.0183
Fe	0.0027	0.0044	0.0044	0.0049
Mg	0.0000	0.0000	0.0000	0.0000
Ba	0.0000	0.0000	0.0000	0.0000
Ca	0.0124	0.0136	0.0124	0.0135
Na	0.4806	0.4806	0.4847	0.4953
K	0.4859	0.4681	0.4933	0.4864
Calculated end members				
Or	49.598	48.604	49.768	48.831
Ab	49.053	49.892	48.897	49.733
An	1.308	1.462	1.294	1.395

Table E.1 (continued)

Sanidine Analyses

Oxides (wt.%)	SR8-S5R	SL4-S1C	SL4-S1R	SL4-S2C
SiO_2	66.13	65.37	66.08	67.13
TiO_2	0.00	0.01	0.02	0.01
Al_2O_3	18.77	18.99	19.47	19.62
FeO	0.11	0.00	0.00	0.00
MgO	0.00	0.00	0.00	0.00
BaO	0.00	0.02	0.16	0.02
CaO	0.21	0.22	0.29	0.28
Na_2O	5.42	5.34	5.55	5.53
K_2O	8.97	8.58	8.62	8.54
TOTAL	99.61	98.54	100.20	101.14
Cation formula (based on 8 oxygens)				
Si	2.9932	2.9843	2.9719	2.9820
Ti	0.0000	0.0003	0.0006	0.0003
Al	1.0015	1.0220	1.0323	1.0273
Fe	0.0040	0.0000	0.0000	0.0000
Mg	0.0000	0.0000	0.0000	0.0000
Ba	0.0000	0.0003	0.0028	0.0003
Ca	0.0102	0.0109	0.0139	0.0135
Na	0.4755	0.4727	0.4836	0.4761
K	0.5179	0.4999	0.4949	0.4842
Calculated end members				
Or	51.562	50.762	49.683	49.665
Ab	47.341	48.008	48.549	48.833
An	1.058	1.156	1.438	1.428

Table E.1 (continued)

Sanidine Analyses

Oxides (wt.%)	SL4-S2R	SL4-S3C	SL4-S3R	SA8-S1R
SiO_2	66.71	67.37	66.75	65.84
TiO_2	0.00	0.00	0.00	0.04
Al_2O_3	19.24	19.20	19.50	19.37
FeO	0.00	0.00	0.00	0.07
MgO	0.00	0.00	0.00	0.03
BaO	0.04	0.02	0.00	0.42
CaO	0.28	0.24	0.22	0.22
Na_2O	5.63	5.41	5.55	4.41
K_2O	8.66	8.96	8.84	10.18
TOTAL	100.56	101.20	100.86	100.59
Cation formula (based on 8 oxygens)				
Si	2.9858	2.9954	2.9792	2.9714
Ti	0.0000	0.0000	0.0000	0.0014
Al	1.0149	1.0064	1.0260	1.0303
Fe	0.0000	0.0000	0.0000	0.0028
Mg	0.0000	0.0000	0.0000	0.0017
Ba	0.0006	0.0003	0.0000	0.0074
Ca	0.0135	0.0113	0.0102	0.0104
Na	0.4886	0.4668	0.4803	0.3859
K	0.4947	0.5086	0.5033	0.5864
Calculated end members				
Or	49.554	51.487	50.597	59.165
Ab	48.943	47.255	48.288	38.948
An	1.399	1.185	1.074	1.096

Table E.1 (continued)

Sanidine Analyses

Oxides (wt.%)	SA8-S2C	SA8-S2R	SA8-S3R	SA8-S4C
SiO_2	66.39	66.56	67.23	66.33
TiO_2	0.01	0.00	0.03	0.00
Al_2O_3	19.39	19.25	19.19	19.33
FeO	0.17	0.12	0.20	0.18
MgO	0.01	0.04	0.02	0.01
BaO	0.18	0.26	0.04	0.07
CaO	0.18	0.16	0.15	0.17
Na_2O	4.32	4.49	4.38	4.42
K_2O	10.31	9.89	10.51	10.58
TOTAL	100.96	100.76	101.74	101.10
Cation formula (based on 8 oxygens)				
Si	2.9795	2.9872	2.9920	2.9768
Ti	0.0003	0.0000	0.0008	0.0000
Al	1.0254	1.0185	1.0069	1.0227
Fe	0.0063	0.0044	0.0076	0.0069
Mg	0.0004	0.0025	0.0012	0.0007
Ba	0.0032	0.0045	0.0006	0.0012
Ca	0.0085	0.0076	0.0070	0.0082
Na	0.3761	0.3905	0.3778	0.3842
K	0.5906	0.5664	0.5966	0.6065
Calculated end members				
Or	60.302	58.390	60.687	60.546
Ab	38.419	40.277	38.449	38.423
An	0.910	0.828	0.758	0.862

Table E.1 (continued)

Sanidine Analyses

Oxides (wt.%)	SA8-S4R	SM4-S1R	SM4-S2R
SiO_2	66.16	67.33	65.59
TiO_2	0.00	0.00	0.01
Al_2O_3	19.42	19.25	19.29
FeO	0.15	0.14	0.02
MgO	0.01	0.00	0.00
BaO	0.26	0.00	0.15
CaO	0.18	0.18	0.21
Na_2O	4.30	4.27	4.38
K_2O	10.51	10.48	10.34
TOTAL	100.98	101.65	99.99
Cation formula (based on 8 oxygens)			
Si	2.9742	2.9952	2.9740
Ti	0.0000	0.0000	0.0001
Al	1.0289	1.0092	1.0307
Fe	0.0056	0.0051	0.0009
Mg	0.0003	0.0000	0.0000
Ba	0.0045	0.0000	0.0026
Ca	0.0087	0.0084	0.0101
Na	0.3750	0.3687	0.3848
K	0.6027	0.5952	0.5984
Calculated end members			
Or	60.763	61.152	60.021
Ab	37.822	37.902	38.615
An	0.920	0.905	1.061

Table E.2

Plagioclase Analyses

Oxides (wt.%)	DA6-P1C	DA6-P1I	DA6-P1R	DA6-P2C
SiO_2	66.16	63.94	66.58	65.97
TiO_2	0.04	0.03	0.01	0.00
Al_2O_3	21.72	21.30	21.39	22.34
FeO	0.19	0.17	0.11	0.06
MgO	0.00	0.00	0.00	0.00
BaO	0.00	0.02	0.00	0.00
CaO	2.84	2.47	2.24	2.36
Na_2O	9.53	9.56	9.46	9.41
K_2O	1.23	1.28	1.48	1.31
TOTAL	101.71	98.76	101.26	101.46
Cation formula (based on 8 oxygens)				
Si	2.8765	2.8663	2.9013	2.8684
Ti	0.0011	0.0008	0.0001	0.0000
Al	1.1130	1.1255	1.0984	1.1448
Fe	0.0069	0.0062	0.0039	0.0023
Mg	0.0000	0.0000	0.0000	0.0000
Ba	0.0000	0.0003	0.0000	0.0000
Ca	0.1320	0.1186	0.1045	0.1101
Na	0.8035	0.8307	0.7991	0.7933
K	0.0684	0.0731	0.0820	0.0729
Calculated end members				
Or	6.846	7.175	8.354	7.499
Ab	79.940	81.132	80.975	81.154
An	13.174	11.619	10.630	11.306

Table E.2 (continued)

Plagioclase Analyses

Oxides (wt.%)	DA6-P2R	DA6-P3R	SR4-P1C	S1-P1R
SiO_2	66.16	66.17	66.32	66.71
TiO_2	0.00	0.00	0.00	0.03
Al_2O_3	21.36	21.51	20.90	21.08
FeO	0.09	0.16	0.12	0.10
MgO	0.00	0.00	0.00	0.00
BaO	0.00	0.00	0.02	0.00
CaO	2.22	2.05	1.49	1.51
Na_2O	9.56	9.80	9.61	9.70
K_2O	1.41	1.34	1.68	1.94
TOTAL	100.80	101.03	100.14	101.06
Cation formula (based on 8 oxygens)				
Si	2.8969	2.8919	2.9199	2.9150
Ti	0.0000	0.0000	0.0001	0.0008
Al	1.1021	1.1079	1.0849	1.0857
Fe	0.0031	0.0057	0.0043	0.0035
Mg	0.0002	0.0000	0.0000	0.0000
Ba	0.0000	0.0000	0.0003	0.0000
Ca	0.1042	0.0959	0.0703	0.0705
Na	0.8118	0.8301	0.8202	0.8223
K	0.0788	0.0749	0.0945	0.1082
Calculated end members				
Or	7.949	7.512	9.619	10.836
Ab	81.506	82.837	83.141	82.044
An	10.504	9.611	7.168	7.079

Table E.2 (continued)

Plagioclase Analyses

Oxides (wt.%)	S1-P2C	S1-P3C	S1-P3R	SR8-P1R
SiO_2	67.40	66.42	66.44	66.72
TiO_2	0.01	0.03	0.00	0.02
Al_2O_3	20.85	20.98	20.85	20.97
FeO	0.17	0.09	0.13	0.17
MgO	0.00	0.00	0.00	0.00
BaO	0.13	0.00	0.00	0.07
CaO	1.50	1.68	1.82	1.64
Na_2O	9.64	9.78	9.64	9.70
K_2O	1.83	1.66	1.58	1.86
TOTAL	101.51	100.65	100.46	101.16
Cation formula (based on 8 oxygens)				
Si	2.9306	2.9132	2.9177	2.9156
Ti	0.0002	0.0011	0.0000	0.0006
Al	1.0687	1.0844	1.0795	1.0802
Fe	0.0060	0.0033	0.0048	0.0062
Mg	0.0001	0.0000	0.0000	0.0000
Ba	0.0021	0.0000	0.0000	0.0012
Ca	0.0696	0.0791	0.0855	0.0767
Na	0.8126	0.8316	0.8210	0.8219
K	0.1013	0.0926	0.0882	0.1037
Calculated end members				
Or	10.307	9.260	8.899	10.363
Ab	82.335	82.784	82.439	81.798
An	7.096	7.917	8.621	7.675

Table E.2 (continued)

Plagioclase Analyses

Oxides (wt.%)	SR8-P2C	SR8-P2R	SR8-P3C	SR8-P3R
SiO_2	67.23	66.17	66.81	66.91
TiO_2	0.00	0.01	0.02	0.02
Al_2O_3	21.12	20.67	20.49	21.40
FeO	0.13	0.13	0.14	0.15
MgO	0.00	0.00	0.00	0.00
BaO	0.00	0.00	0.00	0.00
CaO	1.88	1.70	1.49	1.92
Na_2O	9.63	9.52	9.36	9.64
K_2O	1.57	1.92	2.01	1.58
TOTAL	101.56	100.12	100.32	101.61
Cation formula (based on 8 oxygens)				
Si	2.9189	2.9200	2.9376	2.9057
Ti	0.0000	0.0003	0.0005	0.0005
Al	1.0806	1.0750	1.0620	1.0953
Fe	0.0047	0.0049	0.0049	0.0056
Mg	0.0000	0.0000	0.0000	0.0000
Ba	0.0000	0.0000	0.0000	0.0000
Ca	0.0874	0.0804	0.0702	0.0892
Na	0.8104	0.8144	0.7980	0.8115
K	0.0868	0.1079	0.1126	0.0874
Calculated end members				
Or	8.843	10.785	11.506	8.874
Ab	82.206	81.124	81.266	82.024
An	8.911	8.052	7.187	9.061

Table E.2 (continued)

Plagioclase Analyses

Oxides (wt.%)	SL4-P1R	SL4-P2R	SA8-P1R	SA8-P2C
SiO_2	67.62	67.06	65.11	64.87
TiO_2	0.00	0.00	0.00	0.00
Al_2O_3	20.92	20.86	22.80	22.45
FeO	0.00	0.00	0.20	0.12
MgO	0.00	0.00	0.01	0.01
BaO	0.11	0.00	0.11	0.20
CaO	1.62	1.59	2.91	2.96
Na_2O	9.49	9.55	9.26	9.13
K_2O	1.91	1.90	1.19	1.17
TOTAL	101.68	100.96	101.60	100.91
Cation formula (based on 8 oxygens)				
Si	2.9331	2.9285	2.8366	2.8454
Ti	0.0000	0.0000	0.0000	0.0000
Al	1.0695	1.0740	1.1709	1.1605
Fe	0.0000	0.0000	0.0074	0.0043
Mg	0.0000	0.0000	0.0006	0.0005
Ba	0.0018	0.0000	0.0018	0.0034
Ca	0.0754	0.0744	0.1359	0.1393
Na	0.7982	0.8088	0.7825	0.7761
K	0.1059	0.1057	0.0661	0.0654
Calculated end members				
Or	10.818	10.714	6.731	6.676
Ab	81.238	81.691	79.243	78.763
An	7.713	7.555	13.796	14.170

Table E.2 (continued)

Plagioclase Analyses

Oxides (wt.%)	SA8-P2R	SA8-P3C	SA8-P3I	SA8-P3R
SiO_2	64.93	64.50	63.25	63.76
TiO_2	0.00	0.01	0.00	0.01
Al_2O_3	22.37	22.52	23.01	22.90
FeO	0.20	0.21	0.22	0.13
MgO	0.00	0.00	0.02	0.03
BaO	0.00	0.15	0.00	0.04
CaO	2.78	3.18	3.56	3.88
Na_2O	9.10	9.04	8.82	8.70
K_2O	1.30	1.21	1.12	0.97
TOTAL	100.68	100.83	100.27	100.42
Cation formula (based on 8 oxygens)				
Si	2.8507	2.8348	2.8037	2.8116
Ti	0.0000	0.0001	0.0000	0.0003
Al	1.1576	1.1668	1.2021	1.1904
Fe	0.0073	0.0078	0.0081	0.0047
Mg	0.0000	0.0001	0.0010	0.0018
Ba	0.0000	0.0025	0.0000	0.0006
Ca	0.1306	0.1499	0.1690	0.1835
Na	0.7751	0.7707	0.7584	0.7442
K	0.0728	0.0676	0.0636	0.0545
Calculated end members				
Or	7.469	6.861	6.449	5.585
Ab	79.119	77.700	76.442	75.627
An	13.371	15.145	17.069	18.683

Table E.2 (continued)

Plagioclase Analyses

Oxides (wt.%)	SA8-P4C	SA8-P4R	SM4-P1C	SM4-P1R
SiO_2	58.46	64.67	62.76	63.31
TiO_2	0.01	0.00	0.01	0.00
Al_2O_3	27.18	22.08	23.48	22.97
FeO	0.21	0.17	0.18	0.23
MgO	0.01	0.00	0.00	0.00
BaO	0.02	0.15	0.00	0.00
CaO	7.66	2.61	4.40	3.90
Na_2O	6.85	9.23	8.64	8.83
K_2O	0.37	1.42	0.77	0.84
TOTAL	100.77	100.33	100.24	100.08
Cation formula (based on 8 oxygens)				
Si	2.9544	2.8546	2.7772	2.8028
Ti	0.0003	0.0000	0.0001	0.0000
Al	1.4215	1.1486	1.2246	1.1986
Fe	0.0078	0.0063	0.0065	0.0086
Mg	0.0003	0.0001	0.0002	0.0000
Ba	0.0003	0.0025	0.0000	0.0000
Ca	0.3643	0.1235	0.2085	0.1849
Na	0.5897	0.7901	0.7415	0.7582
K	0.0208	0.0800	0.0437	0.0474
Calculated end members				
Or	2.171	8.065	4.433	4.820
Ab	60.415	79.225	74.535	76.461
An	37.340	12.417	20.990	18.679

Table E.2 (continued)

Plagioclase Analyses

Oxides (wt.%)	SM4-P2R	SM4-P3R
SiO_2	63.55	65.53
TiO_2	0.02	0.00
Al_2O_3	23.47	22.06
FeO	0.12	0.09
MgO	0.00	0.00
BaO	0.00	0.00
CaO	4.19	2.86
Na_2O	8.67	9.27
K_2O	0.86	1.26
TOTAL	100.88	101.08
Cation formula (based on 8 oxygens)		
Si	2.7905	2.8646
Ti	0.0006	0.0000
Al	1.2150	1.1366
Fe	0.0045	0.0033
Mg	0.0000	0.0000
Ba	0.0000	0.0000
Ca	0.1969	0.1341
Na	0.7383	0.7857
K	0.0484	0.0705
Calculated end members		
Or	4.959	7.151
Ab	74.975	79.243
An	20.026	13.566

Table E.3

Biotite Analyses

Oxides (wt.%)	S1-B1	SL4-B1	SL4-B2	SA8-B1
SiO_2	38.00	37.89	38.26	37.96
Al_2O_3	12.18	12.77	12.42	15.49
FeO	21.91	20.94	20.72	18.73
TiO_2	3.09	3.10	3.04	3.30
MnO	0.99	0.88	0.80	0.49
MgO	11.26	10.09	10.81	11.15
CaO	0.02	0.13	0.05	0.02
Na_2O	0.65	0.41	0.48	0.41
K_2O	8.53	7.77	8.40	8.40
F	3.89	1.60	1.74	3.19
TOTAL	99.45	95.10	96.21	98.23
Cation formula (based on 22 oxygens)				
Si	5.341	5.676	5.666	5.324
Al^{IV}	2.018	2.256	2.168	2.562
Al^{VI}	0.000	0.000	0.000	0.000
Fe	2.575	2.623	2.567	2.197
Ti	0.327	0.349	0.399	0.348
Mn	0.118	0.116	0.101	0.058
Mg	2.359	2.252	2.386	2.331
Ca	0.003	0.021	0.008	0.003
Na	0.177	0.119	0.137	0.111
K	1.530	1.485	1.588	1.504
F	1.729	0.758	0.815	1.415

Table E.3 (continued)

Biotite Analyses

Oxides (wt.%)	SA8-B2	SA8-B3	SM4-B1
SiO_2	37.78	37.86	37.89
Al_2O_3	13.17	13.33	13.25
FeO	20.05	20.22	19.58
TiO_2	3.68	3.81	3.51
MnO	0.52	0.54	0.61
MgO	11.97	11.78	12.31
CaO	0.00	0.01	0.05
Na_2O	0.50	0.42	0.59
K_2O	8.90	8.90	8.87
F	2.04	0.97	2.95
TOTAL	98.03	97.55	98.78
Cation formula (based on 22 oxygens)			
Si	5.466	5.586	5.366
Al^{IV}	2.247	2.319	2.213
Al^{VI}	0.000	0.000	0.000
Fe	2.427	2.495	2.319
Ti	0.401	0.423	0.374
Mn	0.064	0.067	0.073
Mg	2.581	2.590	2.598
Ca	0.000	0.002	0.008
Na	0.141	0.121	0.162
K	1.643	1.675	1.603
F	0.934	0.453	1.322

Table E.4

Hornblende Analyses

Oxides (wt.%)	SR4-H1	SR4-H2	SR8-H1	SL4-H1
SiO_2	48.21	47.15	46.31	47.08
Al_2O_3	6.02	5.67	6.05	6.06
FeO	18.77	20.03	20.20	19.15
TiO_2	0.86	0.94	1.03	1.20
MnO	1.55	1.94	2.00	1.72
MgO	10.66	10.35	9.99	10.91
CaO	9.08	9.71	9.96	9.23
Na_2O	2.20	2.12	2.08	2.25
K_2O	0.82	0.49	0.70	0.63
F	2.18	0.40	2.46	2.21
TOTAL	99.70	98.67	100.09	99.82
Cation formula (based on 23 oxygens)				
Si	6.907	7.061	6.688	6.774
Al^{IV}	1.018	0.939	1.029	1.027
Al^{VI}	0.000	0.074	0.000	0.000
Fe	2.249	2.509	2.440	2.304
Ti	0.093	0.106	0.112	0.130
Mn	0.188	0.246	0.245	0.209
Mg	2.276	2.310	2.151	2.339
Ca	1.394	1.558	1.541	1.432
Na	0.611	0.616	0.583	0.628
K	0.150	0.094	0.128	0.116
F	0.987	0.190	1.124	1.005

Table E.5

Oxide Analyses

Oxides (wt.%)	SR8-M1	SR8-M2	SA8-I1	SM4-M1
SiO_2	0.15	0.13	0.02	0.14
TiO_2	9.00	8.25	44.24	5.38
Al_2O_3	0.76	0.69	0.10	1.17
Cr_2O_3	0.08	0.07	0.07	0.12
Fe_2O_3	49.95	51.50	12.69	55.18
FeO	36.85	36.38	30.92	32.74
MnO	2.18	1.99	5.77	2.03
MgO	0.30	0.25	1.71	0.52
TOTAL	99.27	99.26	95.52	97.28
Cation formula (based on 4 oxygens)				
Si	0.0057	0.0050	0.0005	0.0055
Ti	0.2584	0.2373	0.8721	0.1575
Al	0.0342	0.0311	0.0031	0.0537
Cr	0.0024	0.0021	0.0015	0.0037
Fe^{3+}	1.4351	1.4822	0.2502	1.6167
Fe^{2+}	1.1766	1.1635	0.6778	1.0659
Mn	0.0705	0.0645	0.1281	0.0669
Mg	0.0171	0.0142	0.0668	0.0302
Calculated end members				
X_{Usp}	0.26	0.23	----	0.16
X_{Il}	----	----	0.86	----

Table E.6

Glass Analyses

Oxides (wt.%)	DM3-G1	DM3-G2	DA6-G1	DA6-G2
SiO_2	75.75	76.00	75.92	75.35
TiO_2	0.09	0.07	0.10	0.05
Al_2O_3	12.09	11.94	12.35	12.34
FeO	1.01	0.74	0.69	0.75
MgO	0.02	0.02	0.01	0.02
BaO	0.00	0.02	0.04	0.00
CaO	0.34	0.33	0.33	0.34
Na_2O	3.72	3.81	3.73	3.81
K_2O	4.01	4.23	4.39	4.49
TOTAL	97.03	97.17	97.55	97.15

Oxides (wt.%)	SR4-G1	SR8-G1	SL4-G1
SiO_2	76.15	76.03	76.18
TiO_2	0.05	0.08	0.02
Al_2O_3	12.36	12.30	12.52
FeO	0.81	0.76	0.52
MgO	0.02	0.03	0.00
BaO	0.07	0.00	0.00
CaO	0.30	0.33	0.32
Na_2O	3.93	3.86	4.01
K_2O	3.48	4.15	3.93
TOTAL	97.19	97.54	97.50

APPENDIX F

WHOLE ROCK MAJOR AND TRACE ELEMENT CHEMISTRY

In this appendix the major and trace element chemistry of whole rock samples as determined by XRF and INAA is given. Samples are grouped according to domes taken from and are generally in order of decreasing age. Major elements and trace elements marked with * by XRF, all other trace elements by INAA. Major elements in wt.%, trace elements in PPM. Total Fe as Fe_2O_3, n.d. = not detected, LOI = loss on ignition, --- = not analyzed.

APPENDIX F (continued)

Sample	DM-0	DM-1	DM-2	DM-3	DM-4
Dome	DM-II	DM-II	DM-II	DM-II	DM-III
SiO_2	76.57	73.70	76.76	74.29	76.02
TiO_2	0.087	0.090	0.087	0.078	0.121
Al_2O_3	12.29	12.07	12.30	11.84	12.61
Fe_2O_3	1.12	1.05	1.11	1.01	1.02
MnO	0.061	0.051	0.050	0.054	0.068
MgO	0.19	0.03	0.05	0.04	0.09
CaO	0.35	0.34	0.22	0.33	0.37
Na_2O	4.29	3.93	4.08	3.84	4.33
K_2O	4.65	4.70	4.64	4.63	4.81
P_2O_5	0.007	0.007	0.008	0.010	0.010
LOI	0.39	3.31	0.35	3.33	0.31
H_2O^-	0.07	0.19	0.19	0.19	0.17
TOTAL	100.08	99.47	99.85	99.64	99.93
Rb*	153	147	155	153	143
Sr*	3.9	4.5	5.6	4.0	4.6
Y*	46.2	44.4	38.5	44.4	43.4
Zr*	165.4	162.4	160.7	155.2	183.2
Nb*	51.6	50.1	52.3	50.3	52.1
Mo*	4.8	5.1	3.2	5.0	5.6
Ba*	27	33	43	24	24
Pb*	28.9	28.5	26.8	29.5	28.8
Th*	18.5	18.1	20.7	19.8	18.7
Sc	1.5	1.4	1.5	1.4	1.7
Cr	<1.6	<0.7	<0.9	<0.6	2.7
Zn	35	40	33	32	36
As	n.d.	1.4	n.d.	1.6	1.4
Se	<0.3	n.d.	<0.6	<0.6	<0.4
Br	2.6	3.3	n.d.	2.8	3.6
Rb	152	145	154	152	140
Sb	0.25	0.21	0.25	0.13	0.22
Cs	5.27	4.92	3.87	5.28	4.67
Ba	32	19	59	40	60
La	44.5	43.9	43.3	44.2	43.1
Ce	92.4	91.5	97.4	90.0	88.6
Nd	34.2	33.6	32.5	34.3	34.4
Sm	6.9	6.8	6.1	6.7	6.6
Eu	0.188	0.202	0.211	0.173	0.260
Tb	1.29	1.17	1.05	1.23	1.20
Yb	4.55	4.48	3.79	4.58	4.46
Lu	0.688	0.663	0.564	0.676	0.659
Hf	7.2	6.7	7.1	6.9	7.4
Ta	4.0	3.9	3.8	3.8	3.8
Th	17.2	16.8	17.9	17.1	16.6
U	5.44	5.19	5.43	5.62	5.03

APPENDIX F (continued)

Sample	DM-5	DM-7	DM-8	DM-9	DM-10
Dome	DM-II	DM-III	DM-III	DM-II	DM-I
SiO_2	76.80	73.57	75.44	76.44	76.64
TiO_2	0.088	0.112	0.118	0.093	0.095
Al_2O_3	12.32	12.36	12.73	12.42	12.53
Fe_2O_3	1.10	1.02	1.06	1.08	0.89
MnO	0.054	0.058	0.064	0.059	0.056
MgO	0.01	0.04	0.24	0.05	0.27
CaO	0.34	0.35	0.36	0.35	0.35
Na_2O	4.29	4.02	4.48	4.05	4.28
K_2O	4.69	4.69	4.72	4.59	4.58
P_2O_5	0.007	0.008	0.008	0.008	0.008
LOI	0.37	3.53	0.56	0.43	0.49
H_2O^-	0.11	0.16	0.03	0.04	0.12
TOTAL	100.18	99.92	99.81	99.61	100.31
Rb*	154	137	143	155	154
Sr*	4.6	5.2	4.9	3.9	3.7
Y*	45.3	42.1	43.6	45.5	45.5
Zr*	166.6	179.6	186.0	166.0	164.9
Nb*	51.6	50.6	52.0	51.8	51.8
Mo*	5.8	4.8	5.3	5.3	5.9
Ba*	29	36	25	22	25
Pb*	29.7	27.7	29.2	29.0	30.1
Th*	19.3	18.2	18.3	18.0	19.7
Sc	1.5	1.6	1.6	1.5	1.4
Cr	<0.3	<0.4	<0.8	<1.4	<0.2
Zn	35	31	46	36	40
As	1.8	1.1	n.d.	1.4	1.6
Se	<0.4	<0.2	<0.4	<0.3	<0.1
Br	3.6	3.3	2.2	3.0	3.2
Rb	151	133	139	153	148
Sb	0.24	0.15	0.29	0.14	0.23
Cs	5.19	4.59	4.57	5.23	5.06
Ba	45	51	13	42	4
La	45.3	45.1	44.3	45.0	44.3
Ce	93.1	90.7	94.0	93.0	90.9
Nd	35.3	35.3	34.4	36.2	32.9
Sm	6.8	6.7	6.8	6.7	6.7
Eu	0.192	0.254	0.254	0.188	0.184
Tb	1.24	1.19	1.17	1.25	1.20
Yb	4.59	4.29	4.34	4.58	4.42
Lu	0.693	0.653	0.654	0.691	0.663
Hf	7.3	7.4	7.4	7.1	6.8
Ta	4.1	3.8	3.8	4.0	3.8
Th	17.4	16.7	16.7	17.3	17.0
U	5.42	5.40	5.36	5.90	5.50

APPENDIX F (continued)

Sample	DM-11	DA-1	DA-3	DA-4	DA-5
Dome	DM-I	DA-I	DA-I	DA-I	DA-I
SiO_2	76.48	77.33	76.82	76.85	76.74
TiO_2	0.095	0.093	0.089	0.094	0.092
Al_2O_3	12.26	12.37	12.33	12.42	12.48
Fe_2O_3	1.12	0.89	0.90	0.89	0.95
MnO	0.056	0.044	0.050	0.056	0.052
MgO	0.02	0.39	0.00	0.07	0.20
CaO	0.35	0.30	0.29	0.31	0.28
Na_2O	4.25	4.09	3.96	4.09	3.99
K_2O	4.66	4.70	4.69	4.70	4.66
P_2O_5	0.007	0.008	0.015	0.008	0.012
LOI	0.30	0.11	0.26	0.25	0.38
H_2O^-	0.09	0.06	0.03	0.03	0.07
TOTAL	99.69	100.39	99.43	99.77	99.91
Rb*	154	199	203	199	196
Sr*	3.6	7.9	7.3	7.9	7.8
Y*	45.4	51.7	36.9	44.8	40.0
Zr*	165.7	113.2	113.6	114.9	114.7
Nb*	51.8	54.2	55.9	55.9	55.7
Mo*	5.5	3.3	5.2	3.2	4.6
Ba*	27	31	31	26	34
Pb*	31.5	24.1	22.8	26.8	25.5
Th*	19.1	24.6	23.3	23.6	22.9
Sc	1.4	1.4	1.5	1.5	1.7
Cr	<1.3	<0.6	<0.5	<0.4	<1.0
Zn	45	11	10	13	16
As	n.d.	1.7	2.4	n.d.	2.2
Se	<0.3	<0.5	<0.5	<0.2	<0.2
Br	3.1	n.d.	0.5	n.d.	0.5
Rb	154	193	198	196	192
Sb	0.23	0.25	0.40	0.10	0.35
Cs	5.04	4.58	5.10	5.96	4.92
Ba	36	50	52	63	49
La	44.4	36.5	28.8	34.9	37.8
Ce	92.9	66.5	61.6	73.1	75.8
Nd	34.2	23.2	18.4	24.8	28.3
Sm	6.8	6.2	4.6	5.6	6.2
Eu	0.16	0.233	0.194	0.205	0.283
Tb	1.22	1.22	0.96	1.18	1.13
Yb	4.54	5.26	4.26	5.28	4.56
Lu	0.683	0.786	0.661	0.803	0.659
Hf	6.9	6.0	5.6	6.3	5.7
Ta	3.8	5.2	5.2	5.2	5.1
Th	16.9	23.1	22.6	23.8	23.0
U	5.40	7.03	7.51	7.75	7.99

APPENDIX F (continued)

Sample	DA-6	DA-7	DA-8	SR-1	SR-2
Dome	DA-III	DA-III	DA-II	SR-I	SR-I
SiO_2	75.15	75.32	77.13	77.15	74.87
TiO_2	0.101	0.097	0.100	0.079	0.080
Al_2O_3	12.41	12.30	12.60	12.58	12.82
Fe_2O_3	0.85	0.85	0.86	0.89	0.85
MnO	0.061	0.057	0.043	0.051	0.076
MgO	0.01	0.07	0.08	0.00	0.00
CaO	0.40	0.41	0.30	0.31	0.34
Na_2O	3.86	3.87	4.03	4.22	4.10
K_2O	4.68	4.70	4.59	4.64	4.34
P_2O_5	0.007	0.007	0.010	0.008	0.007
LOI	2.29	2.67	0.21	0.43	1.85
H_2O^-	0.40	0.13	0.18	0.11	0.74
TOTAL	100.22	100.48	100.14	100.47	100.07
Rb*	190	196	197	232	200
Sr*	9.9	8.4	7.3	2.6	3.4
Y*	51.2	52.4	38.4	58.7	64.2
Zr*	115.4	112.3	114.4	120.9	117.7
Nb*	55.1	54.6	55.6	74.1	73.9
Mo*	6.3	6.5	5.6	6.8	6.8
Ba*	42	36	32	10	84
Pb*	45.6	30.9	61.0	33.1	34.6
Th*	26.8	23.6	26.3	30.3	29.3
Sc	1.5	1.5	1.4	1.4	1.6
Cr	<0.9	<0.4	<0.6	<0.7	<1.1
Zn	22	20	15	21	32
As	2.1	2.2	3.1	3.0	2.5
Se	<0.4	<0.2	<0.1	<0.4	<0.5
Br	2.1	2.1	n.d.	1.5	1.8
Rb	186	189	196	228	196
Sb	0.31	0.32	0.35	0.40	0.38
Cs	7.41	7.33	5.31	7.83	7.46
Ba	84	51	46	0	105
La	33.9	35.3	31.4	30.2	41.8
Ce	71.3	75.5	73.7	59.1	89.0
Nd	23.8	25.4	22.0	24.6	29.8
Sm	5.6	5.8	5.0	6.4	7.3
Eu	0.201	0.202	0.221	0.155	0.121
Tb	1.16	1.26	0.94	1.42	1.61
Yb	5.14	5.24	4.01	6.01	6.89
Lu	0.759	0.802	0.593	0.872	1.013
Hf	5.6	5.7	6.0	6.3	6.5
Ta	4.9	5.0	5.1	6.4	6.5
Th	22.9	22.6	22.9	27.8	28.3
U	7.25	7.58	7.47	9.5	9.22

APPENDIX F (continued)

Sample	SR-3	SR-4	SR-5	SR-6	SR-7
Dome	SR-I	SR-I	SR-II	SR-II	SR-II
SiO_2	74.75	74.86	74.09	74.44	74.51
TiO_2	0.082	0.080	0.079	0.084	0.087
Al_2O_3	13.49	12.49	12.75	12.80	12.50
Fe_2O_3	0.97	0.87	0.95	0.93	0.93
MnO	0.073	0.071	0.076	0.073	0.071
MgO	0.17	0.14	0.15	0.11	0.26
CaO	0.35	0.37	0.37	0.37	0.35
Na_2O	4.24	3.95	3.98	3.90	3.90
K_2O	4.33	4.78	5.04	5.01	4.87
P_2O_5	0.006	0.003	0.012	0.006	0.004
LOI	1.60	2.58	2.52	2.43	2.42
H_2O^-	0.50	0.20	0.18	0.21	0.26
TOTAL	100.56	100.39	100.20	100.36	100.16
Rb*	169	228	227	272	271
Sr*	4.9	1.5	7.7	3.4	3.7
Y*	60.0	67.0	81.6	80.0	78.8
Zr*	125.8	113.8	126.0	125.2	123.9
Nb*	78.9	72.3	90.6	89.4	90.8
Mo*	8.2	8.0	6.4	6.1	5.8
Ba*	146	9	22	18	31
Pb*	37.7	47.8	38.7	39.8	33.0
Th*	32.8	29.5	34.4	34.5	34.3
Sc	1.7	1.4	1.6	1.5	1.5
Cr	<0.6	<0.4	<0.4	1.1	<0.9
Zn	28	26	24	31	26
As	3.0	3.1	28.5	8.6	2.4
Se	<0.4	<0.8	<0.2	<1.1	<0.8
Br	1.4	1.7	1.9	1.3	1.3
Rb	166	223	275	272	269
Sb	0.40	0.40	0.55	0.53	0.50
Cs	6.80	8.37	10.17	9.55	9.89
Ba	156	42	43	60	54
La	28.0	30.4	36.1	37.1	32.9
Ce	71.8	69.4	74.8	81.7	72.4
Nd	20.9	26.5	31.3	28.9	30.9
Sm	6.0	6.4	7.3	7.0	7.1
Eu	0.103	0.093	0.095	0.090	0.093
Tb	1.43	1.52	1.73	1.70	1.78
Yb	6.30	6.79	8.65	8.48	8.52
Lu	0.942	1.041	1.338	1.288	1.303
Hf	7.2	6.3	7.4	7.5	7.3
Ta	6.7	6.4	8.0	7.6	8.0
Th	29.1	27.0	31.4	31.7	31.0
U	9.42	9.61	11.90	11.40	11.40

APPENDIX F (continued)

Sample	SR-8	S-1	S-3	S-5	S-7
Dome	SR-II	S	S	S	S
SiO_2	74.57	76.92	74.89	75.62	75.35
TiO_2	0.086	0.080	0.084	0.079	0.089
Al_2O_3	12.62	12.66	12.81	12.39	12.70
Fe_2O_3	0.94	0.88	0.84	0.89	0.95
MnO	0.082	0.073	0.078	0.066	0.081
MgO	0.36	0.02	0.10	0.10	0.10
CaO	0.37	0.24	0.37	0.36	0.36
Na_2O	4.16	4.07	4.30	3.76	4.14
K_2O	4.83	4.67	4.75	4.58	4.66
P_2O_5	0.008	0.007	0.005	0.005	0.019
LOI	2.36	0.23	1.81	2.15	1.71
H_2O^-	0.20	0.07	0.16	0.19	0.17
TOTAL	100.59	99.92	100.20	100.19	100.33
Rb*	278	284	273	259	269
Sr*	2.7	2.9	3.6	2.9	6.3
Y*	83.5	60.3	81.0	77.6	80.0
Zr*	121.1	123.3	118.9	119.2	122.3
Nb*	91.2	91.0	91.4	87.8	92.4
Mo*	6.6	5.6	6.5	5.7	5.9
Ba*	14	14	20	18	59
Pb*	32.2	32.0	30.4	35.1	33.8
Th*	32.6	35.2	32.5	35.0	34.5
Sc	1.5	1.5	1.5	1.5	1.5
Cr	<0.4	<0.5	<2.4	<1.3	<0.4
Zn	29	15	35	29	33
As	2.9	2.5	3.4	2.8	3.5
Se	<0.6	<0.7	<0.9	<0.9	<1.1
Br	2.0	0.6	1.2	1.5	1.4
Rb	275	266	268	252	261
Sb	0.56	0.41	0.54	0.49	0.45
Cs	10.14	9.14	9.65	9.02	9.41
Ba	44	74	55	88	55
La	32.9	26.1	31.7	30.5	33.4
Ce	73.9	68.9	70.4	84.4	74.3
Nd	28.9	13.5	22.6	20.0	26.0
Sm	6.9	4.9	6.7	6.3	7.0
Eu	0.085	0.130	0.085	0.083	0.105
Tb	1.80	1.36	1.68	1.64	1.73
Yb	8.79	6.73	7.99	7.81	8.17
Lu	1.333	1.047	1.262	1.203	1.231
Hf	7.1	6.8	6.5	6.2	6.7
Ta	8.0	8.4	7.9	7.6	7.8
Th	30.4	30.7	30.1	30.2	30.9
U	12.00	11.2	10.80	10.30	10.78

APPENDIX F (continued)

Sample	SL-1	SL-2	SL-3	SL-4	SL-5
Dome	SL	SL	SL	SL	SL
SiO_2	73.55	74.99	75.82	74.44	74.98
TiO_2	0.083	0.080	0.086	0.114	0.083
Al_2O_3	13.30	12.38	12.29	12.92	12.30
Fe_2O_3	1.00	0.87	0.86	1.06	0.91
MnO	0.080	0.079	0.077	0.065	0.072
MgO	0.25	0.15	0.01	0.44	0.04
CaO	0.37	0.37	0.34	0.50	0.37
Na_2O	4.06	4.03	4.09	3.99	3.97
K_2O	4.67	4.63	4.65	4.62	4.68
P_2O_5	0.007	0.006	0.004	0.011	0.008
LOI	2.63	2.40	2.03	2.21	2.54
H_2O^-	0.20	0.12	0.23	0.25	0.15
TOTAL	100.20	100.11	100.49	100.62	100.10
Rb*	261	268	265	229	266
Sr*	3.8	2.9	3.2	18.2	4.9
Y*	81.0	81.2	80.8	64.0	78.8
Zr*	127.4	121.3	120.4	116.5	117.8
Nb*	93.0	88.9	87.7	72.4	88.3
Mo*	5.8	5.8	5.8	5.2	6.2
Ba*	28	19	22	105	48
Pb*	34.6	31.0	31.0	29.1	45.9
Th*	35.8	37.0	31.6	34.2	32.6
Sc	1.6	1.5	1.4	2.0	1.4
Cr	<1.6	<0.3	<0.4	<1.1	<0.9
Zn	30	34	25	25	22
As	3.1	3.0	3.0	2.4	3.5
Se	<0.3	<0.7	<0.4	<0.7	n.d.
Br	1.5	1.5	1.4	1.0	1.5
Rb	255	266	253	229	252
Sb	0.47	0.56	0.47	0.39	0.43
Cs	9.32	9.62	10.03	7.79	9.58
Ba	40	37	58	55	93
La	38.5	30.9	27.8	37.0	29.1
Ce	81.8	67.3	60.0	78.4	57.1
Nd	23.8	23.5	21.2	24.3	19.1
Sm	7.4	6.7	6.5	6.3	6.3
Eu	0.085	0.084	0.093	0.165	0.083
Tb	1.80	1.70	1.73	1.42	1.60
Yb	8.41	8.24	7.87	6.95	8.00
Lu	1.280	1.269	1.274	1.015	1.238
Hf	6.7	6.5	6.3	5.7	6.3
Ta	7.9	7.7	7.9	6.7	7.9
Th	32.3	29.4	28.5	29.8	28.8
U	10.40	11.00	9.95	9.63	10.75

APPENDIX F (continued)

Sample	SA-1	SA-2	SA-3	SA-4	SA-5
Dome	SA-I	SA-I	SA-I	SA-II	SA-II
SiO_2	74.30	73.90	72.91	75.72	76.25
TiO_2	0.148	0.149	0.176	0.156	0.158
Al_2O_3	12.61	12.91	13.31	12.93	12.84
Fe_2O_3	1.18	1.24	1.26	1.22	1.20
MnO	0.053	0.054	0.058	0.054	0.054
MgO	0.32	0.41	0.25	0.29	0.27
CaO	0.69	0.69	0.77	0.64	0.06
Na_2O	3.71	3.79	3.85	3.97	3.94
K_2O	4.82	5.04	5.03	4.82	4.76
P_2O_5	0.020	0.023	0.027	0.023	0.024
LOI	2.18	1.97	2.30	0.26	0.29
H_2O^-	0.18	0.24	0.20	0.06	0.06
TOTAL	100.21	100.42	100.14	100.14	99.91
Rb*	179	187	184	181	182
Sr*	43.3	53.5	48.8	45.0	42.8
Y*	45.9	47.2	49.0	44.4	42.8
Zr*	121.4	129.5	139.2	129.7	129.8
Nb*	49.1	50.5	53.0	49.9	50.4
Mo*	4.1	4.3	4.4	3.6	3.5
Ba*	207	224	217	238	218
Pb*	26.3	25.6	26.2	24.8	23.6
Th*	25.9	25.3	28.2	25.9	26.8
Sc	2.4	2.3	2.6	2.4	2.6
Cr	<0.8	<0.6	1.6	<0.9	1.0
Zn	24	23	27	20	22
As	2.1	2.4	1.9	2.0	2.0
Se	<1.0	<0.5	<0.8	<0.3	<0.6
Br	1.4	1.4	0.9	0.5	0.7
Rb	179	183	181	176	183
Sb	0.30	0.33	0.31	0.29	0.30
Cs	5.38	5.40	5.36	4.63	4.67
Ba	232	237	273	253	221
La	40.0	42.7	50.6	40.2	42.0
Ce	82.7	88.6	102.1	82.1	87.8
Nd	26.4	28.0	31.1	28.2	29.6
Sm	5.6	5.8	6.7	6.1	6.5
Eu	0.293	0.299	0.330	0.328	0.354
Tb	1.09	1.12	1.17	1.11	1.10
Yb	4.81	5.00	5.26	4.72	4.52
Lu	0.734	0.761	0.799	0.703	0.655
Hf	4.7	5.1	5.8	5.5	5.4
Ta	4.7	4.9	5.0	4.7	4.9
Th	23.1	23.7	25.7	23.5	24.5
U	6.91	6.9	7.03	6.84	6.79

APPENDIX F (continued)

Sample	SA-6	SA-8	SA-9	SA-10	SA-11
Dome	SA-II	SA-I	SA-I	SA-I	SA-I
SiO_2	76.11	74.82	75.74	73.00	75.74
TiO_2	0.156	0.144	0.162	0.168	0.161
Al_2O_3	12.83	12.87	13.01	12.90	12.92
Fe_2O_3	1.24	1.16	1.26	1.37	1.26
MnO	0.051	0.058	0.055	0.060	0.054
MgO	0.18	0.20	0.40	0.38	0.24
CaO	0.66	0.70	0.62	0.75	0.72
Na_2O	3.93	3.66	3.89	3.73	3.88
K_2O	4.77	4.72	4.87	4.93	4.73
P_2O_5	0.026	0.023	0.023	0.027	0.030
LOI	0.24	1.99	0.20	2.24	0.44
H_2O^-	0.10	0.22	0.20	0.18	0.06
TOTAL	100.29	100.57	100.43	99.74	100.24
Rb*	178	170	181	194	169
Sr*	46.2	45.4	41.1	50.5	48.5
Y*	42.1	43.6	37.8	48.4	45.3
Zr*	127.3	123.7	140.6	130.7	124.9
Nb*	49.1	48.0	51.1	49.9	49.1
Mo*	3.4	3.7	3.2	4.0	3.8
Ba*	240	230	209	272	247
Pb*	23.6	24.7	25.2	26.2	25.1
Th*	24.6	24.6	27.1	26.0	24.5
Sc	2.2	2.3	2.5	2.5	2.3
Cr	1.2	0.8	1.5	1.0	1.8
Zn	25	24	20	28	29
As	2.1	1.6	1.9	1.4	n.d.
Se	<0.6	<0.3	<0.3	<0.7	<0.4
Br	0.8	0.7	n.d.	1.3	n.d.
Rb	174	170	177	195	167
Sb	0.28	0.28	0.13	0.28	0.29
Cs	4.49	4.85	4.74	5.39	5.25
Ba	244	253	206	260	227
La	42.0	44.9	45.3	47.7	39.3
Ce	84.8	91.7	91.2	97.4	81.4
Nd	30.5	31.8	31.1	31.2	27.9
Sm	6.2	5.9	6.4	6.5	5.7
Eu	0.339	0.312	0.358	0.322	0.305
Tb	1.09	1.02	1.07	1.12	1.06
Yb	4.51	4.71	4.12	5.31	4.90
Lu	0.664	0.713	0.606	0.762	0.753
Hf	5.2	5.7	5.9	5.3	5.1
Ta	4.6	4.8	5.0	4.7	4.7
Th	23.3	23.7	25.7	24.2	22.5
U	6.93	6.60	7.24	6.71	6.73

APPENDIX F (continued)

Sample	LJ-1	SM-1	SM-2	SM-3	SM-4
Dome	LJ	SM	SM	SM	SM
SiO_2	73.58	76.03	77.18	74.90	75.66
TiO_2	0.132	0.124	0.127	0.125	0.122
Al_2O_3	13.07	12.11	12.32	12.55	12.33
Fe_2O_3	1.14	1.04	0.98	1.02	1.00
MnO	0.062	0.054	0.029	0.055	0.048
MgO	0.32	0.31	0.31	0.30	0.17
CaO	0.60	0.53	0.51	0.58	0.53
Na_2O	3.84	3.76	3.87	3.89	3.78
K_2O	4.75	4.62	4.67	4.79	4.72
P_2O_5	0.025	0.015	0.018	0.019	0.018
LOI	2.44	1.62	0.22	1.85	1.84
H_2O^-	0.14	0.17	0.10	0.18	0.13
TOTAL	100.10	100.38	100.33	100.26	100.35
Rb*	212	209	223	218	219
Sr*	27.2	25.3	23.9	25.2	24.7
Y*	57.0	58.3	52.4	59.5	58.1
Zr*	118.1	110.1	121.5	113.5	113.7
Nb*	62.9	59.6	62.1	61.5	60.1
Mo*	5.4	4.7	4.4	4.6	4.8
Ba*	136	115	106	110	119
Pb*	28.0	27.8	25.1	26.1	26.6
Th*	32.5	32.2	32.7	32.6	31.2
Sc	2.4	2.2	2.3	2.2	2.3
Cr	<1.0	<1.0	<0.9	<1.2	<0.7
Zn	20	20	29	29	19
As	2.8	3.1	2.5	2.6	2.7
Se	<0.8	<0.9	<1.0	<0.8	n.d.
Br	1.0	1.0	0.3	0.4	1.0
Rb	199	196	211	210	203
Sb	0.40	0.23	0.36	0.41	0.41
Cs	7.20	6.97	6.47	7.11	7.24
Ba	250	84	77	176	166
La	39.9	31.6	36.8	34.3	31.1
Ce	79.7	61.5	75.7	74.6	65.1
Nd	23.2	13.5	22.2	24.1	25.5
Sm	5.9	5.8	5.9	6.0	5.6
Eu	0.218	0.203	0.207	0.201	0.191
Tb	1.21	1.29	1.26	1.35	1.29
Yb	5.80	5.60	5.44	6.11	5.97
Lu	0.928	0.890	0.837	0.964	0.939
Hf	5.3	5.2	4.6	4.5	5.5
Ta	6.3	6.0	6.2	6.0	6.2
Th	30.0	26.9	29.3	28.7	27.9
U	8.35	7.87	8.71	8.31	8.90

APPENDIX F (continued)

Sample	SM-5	SM-6	SM-7	SM-9	SM-10
Dome	SM	SM	SM	SM	SM
SiO_2	74.34	74.33	74.87	73.87	73.57
TiO_2	0.118	0.130	0.126	0.132	0.128
Al_2O_3	12.38	13.05	12.47	12.78	12.46
Fe_2O_3	0.98	1.07	1.04	1.09	1.07
MnO	0.055	0.061	0.059	0.062	0.063
MgO	0.26	0.33	0.33	0.27	0.28
CaO	0.57	0.64	0.57	0.58	0.57
Na_2O	3.67	3.94	3.73	3.63	3.76
K_2O	4.63	4.81	4.65	4.98	4.81
P_2O_5	0.019	0.019	0.019	0.016	0.014
LOI	2.57	1.95	2.34	2.35	2.56
H_2O^-	0.28	0.08	0.10	0.29	1.18
TOTAL	99.87	100.41	100.30	100.05	100.47
Rb*	208	220	220	219	234
Sr*	27.2	28.4	23.8	24.3	22.7
Y*	55.7	60.0	59.9	62.0	62.4
Zr*	120.1	120.4	117.7	128.0	116.1
Nb*	60.2	62.4	62.9	65.4	65.6
Mo*	4.5	5.2	5.0	5.2	5.1
Ba*	114	126	104	108	98
Pb*	26.0	26.0	26.7	27.1	26.5
Th*	31.2	32.1	33.3	34.2	34.7
Sc	2.2	2.4	2.3	2.5	2.5
Cr	<0.7	<0.6	0.6	1.0	0.7
Zn	29	21	20	21	15
As	2.6	2.6	2.8	2.7	2.7
Se	<0.2	<0.8	<0.7	<0.1	<0.2
Br	1.1	0.6	0.9	0.7	1.0
Rb	204	200	211	201	227
Sb	0.39	0.43	0.45	0.42	0.47
Cs	6.84	7.43	7.72	7.59	8.14
Ba	169	123	147	90	187
La	37.4	36.3	30.9	37.1	37.8
Ce	76.8	76.0	63.7	72.0	73.9
Nd	19.7	23.5	21.7	19.5	22.7
Sm	5.9	6.2	5.9	6.4	6.4
Eu	0.199	0.239	0.209	0.209	0.197
Tb	1.21	1.34	1.25	1.31	1.33
Yb	6.12	5.65	6.09	6.10	6.47
Lu	0.970	0.975	1.038	1.043	1.035
Hf	5.1	4.6	5.3	6.0	5.5
Ta	6.2	6.2	6.4	6.6	6.5
Th	29.5	28.2	29.1	31.0	31.5
U	8.90	---	---	---	---

APPENDIX F (continued)

Sample	BB-1	VC1-BB	VC1-R
Dome	----	------	-----
SiO_2	73.40	73.41	74.38
TiO_2	0.288	0.288	0.267
Al_2O_3	13.31	13.11	12.83
Fe_2O_3	1.94	2.00	1.89
MnO	0.054	0.056	0.058
MgO	0.87	0.66	0.60
CaO	1.49	1.48	1.23
Na_2O	3.82	3.81	3.74
K_2O	4.30	4.32	4.48
P_2O_5	0.076	0.074	0.068
LOI	0.38	0.85	0.75
H_2O^-	0.00	0.05	0.12
TOTAL	99.93	100.11	100.41
Rb*	150	155	166
Sr*	166.1	163.6	120.6
Y*	30.5	29.9	31.7
Zr*	134.3	134.6	135.3
Nb*	36.8	38.3	40.3
Mo*	3.2	3.6	3.9
Ba*	585	520	486
Pb*	20.8	21.4	23.2
Th*	22.0	23.1	25.6
Sc	3.8	3.7	3.6
Cr	8.2	7.8	6.9
Zn	24	31	32
As	1.5	3.1	n.d.
Se	<0.3	n.d.	0.6
Br	0.4	n.d.	n.d.
Rb	138	155	165
Sb	0.14	0.31	0.33
Cs	4.61	4.85	5.18
Ba	581	536	469
La	34.6	35.6	36.1
Ce	67.2	68.0	70.2
Nd	14.5	21.2	23.0
Sm	3.7	3.8	3.9
Eu	0.537	0.519	0.445
Tb	0.59	0.60	0.68
Yb	3.02	3.33	3.66
Lu	0.530	0.533	0.586
Hf	5.1	4.7	5.1
Ta	3.8	3.7	3.8
Th	19.5	20.9	21.5
U	---	---	---

APPENDIX G

ACCURACY AND PRECISION OF ANALYTICAL DATA

This appendix presents calculated accuracy (closeness of the measured value to an accepted value) and precision (ability to make repeat measurements) of the analytical data presented in Appendix F.

The accuracy of the INAA data is constrained by taking the mean, standard deviation (S.D.), and coefficient of variation (C.V.) of values obtained on U.S.G.S. standards BCR-1 and G-2 for six separate irradiations and comparing these to published values for these standards.

The precision of the INAA data has been determined by analyses of triplicates and duplicates of samples SA-4, SA-5, and SA-6. These samples were taken from the same outcrop (within ~50 meters of each other), thus S.D.'s and C.V.'s are presented which show sample preparation error as well as the combined effects of outcrop variability and sample preparation error.

The precision of the XRF data was determined by multiple runs of triplicates of samples SA-4, SA-5, and SA-6. Thus S.D.'s and C.V.'s are presented which show the effect of sample preparation variability and the combined effect of outcrop variability, sample preparation variability, and machine error.

APPENDIX G (continued)

INAA Accuracy
BCR-1

Element	Mean	S.D.	C.V.(%)	Accepted*
Sc	32.04	0.14	0.44	32.8 ± 1.7
Cr	10.60	0.50	4.72	16 ± 4
Zn	149.00	3.90	2.62	129 ± 1
Rb	48.58	1.20	2.47	47.1 ± 0.6
Sb	0.61	0.06	9.84	0.62 ± 0.10
Cs	0.94	0.03	3.19	0.97 ± 0.13
Ba	663.33	20.14	3.04	678 ± 16
La	24.32	0.07	0.29	25.0 ± 0.08
Ce	51.98	0.75	1.44	53.7 ± 0.8
Nd	29.33	1.45	4.94	28.7 ± 0.6
Sm	6.69	0.04	0.60	6.58 ± 0.17
Eu	1.90	0.01	0.53	1.96 ± 0.05
Tb	1.07	0.01	0.93	1.05 ± 0.09
Yb	3.41	0.05	1.47	3.39 ± 0.08
Lu	0.515	0.006	1.17	0.512 ± 0.025
Hf	5.12	0.06	1.17	4.9 ± 0.3
Ta	0.75	0.02	2.67	0.79 ± 0.09
Th	5.61	0.09	1.60	6.04 ± 0.60
U	1.78	0.16	8.99	1.71 ± 0.16

Mean = mean of 6 irradiations at the University of Missouri reactor.
* = Gladney and Burns (1983)
S.D. = standard deviation at the 1 sigma level
C.V. = coefficient of variation, defined as:
[(S.D. / Mean) 100]

APPENDIX G (continued)

INAA Accuracy
G-2

Element	Mean	S.D.	C.V.(%)	Accepted*
Sc	3.34	0.01	0.30	3.5 ± 0.4
Cr	8.00	0.17	2.13	9 ± 2
Zn	65.33	4.27	6.54	85 ± 7
Rb	167.33	2.07	1.24	170 ± 3
Sb	0.04	0.006	15.00	0.078 ± 0.032
Cs	1.36	0.03	2.21	1.33 ± 0.14
Ba	1811.50	47.36	2.61	1880 ± 20
La	85.11	0.56	0.66	86 ± 5
Ce	165.32	1.69	1.02	159 ± 11
Nd	54.32	1.95	3.59	53 ± 8
Sm	7.38	0.11	1.49	7.2 ± 0.6
Eu	1.33	0.02	1.5	1.41 ± 0.12
Tb	0.48	0.02	4.17	0.48 ± 0.07
Yb	0.72	0.03	4.17	0.78 ± 0.14
Lu	0.104	0.007	6.73	0.113 ± 0.024
Hf	8.58	0.37	4.31	7.9 ± 0.7
Ta	0.79	0.02	2.53	0.88 ± 0.12
Th	24.07	0.52	2.16	24.6 ± 1.5
U	1.97	0.12	6.09	2.04 ± 0.17

Mean = mean of 6 irradiations at the University of Missouri reactor.
* = Gladney and Burns (1983)
S.D. = standard deviation at the 1 sigma level
C.V. = coefficient of variation, defined as: [(S.D. / Mean) 100]

APPENDIX G (continued)

INAA Precision
Example of Sample Preparation Error

Element	SA-6(1)	SA-6(2)	SA-6(3)	Mean	S.D.	C.V.(%)
Sc	2.24	2.21	2.24	2.23	0.02	0.78
Cr	1.6	1.2	0.9	1.2	0.35	29.30
Zn	28	22	24	25	3.06	12.22
As	1.9	2.6	1.9	2.1	0.40	19.20
Se	0.4	0.9	0.4	0.6	0.29	48.10
Br	0.3	0.8	1.4	0.8	0.55	68.80
Rb	176	173	174	174	1.50	0.88
Sb	0.26	0.28	0.30	0.28	0.02	7.14
Cs	4.49	4.46	4.52	4.49	0.03	0.67
Ba	247	253	232	244	10.8	4.4
La	40.73	42.08	43.16	41.99	1.22	2.90
Ce	83.6	83.9	86.8	84.8	1.77	2.08
Nd	29.6	31.5	30.5	30.5	0.95	3.12
Sm	6.16	6.18	6.34	6.23	0.098	1.58
Eu	0.340	0.340	0.336	0.339	0.002	0.68
Tb	1.11	1.09	1.07	1.09	0.02	1.83
Yb	4.43	4.59	4.50	4.51	0.08	1.78
Lu	0.661	0.664	0.668	0.664	0.004	0.53
Hf	5.04	5.38	5.15	5.19	0.17	3.34
Ta	4.62	4.64	4.63	4.63	0.01	0.22
Th	23.19	23.07	23.51	23.26	0.23	0.98
U	6.96	6.86	6.96	6.93	0.06	0.83

S.D. = standard deviation at the 1 sigma level
C.V. = coefficient of variation, defined as:
[(S.D. / Mean) 100]

APPENDIX G (continued)

INAA Precision
Cumulative

Element	Mean	S.D.	C.V.(%)
Sc	2.40	0.17	7.08
Cr	1.0	0.15	15.0
Zn	22	2.5	11.2
As	2.0	0.06	2.96
Se	0.50	0.17	34.00
Br	0.7	0.2	28.57
Rb	178	4.7	2.6
Sb	0.29	0.01	3.45
Cs	4.60	0.09	1.96
Ba	239	16.5	6.9
La	41.41	1.01	2.44
Ce	84.9	2.85	3.36
Nd	29.4	1.16	3.94
Sm	6.27	0.18	2.87
Eu	0.340	0.013	3.82
Tb	1.10	0.01	0.91
Yb	4.58	0.12	2.62
Lu	0.674	0.026	3.86
Hf	5.38	0.17	3.16
Ta	4.74	0.11	2.32
Th	23.76	0.65	2.74
U	6.85	0.07	1.02

S.D. = standard deviation at the 1 sigma level
C.V. = coefficient of variation, defined as:
[(S.D. / Mean) 100]

APPENDIX G (continued)

XRF Precision
Example of Sample Preparation Error

Element	SA-6(1)	SA-6(2)	SA-6(3)	Mean	S.D.	C.V.(%)
SiO_2	76.10	76.05	76.17	76.11	0.06	0.08
TiO_2	0.155	0.157	0.156	0.156	0.001	0.64
Al_2O_3	12.80	12.82	12.87	12.83	0.04	0.31
Fe_2O_3	1.27	1.24	1.23	1.25	0.02	1.60
MnO	0.050	0.051	0.052	0.051	0.001	1.96
MgO	0.18	0.15	0.20	0.18	0.03	16.67
CaO	0.66	0.66	0.66	0.66	0.00	0.00
Na_2O	3.91	3.95	3.93	3.93	0.02	0.51
K_2O	4.78	4.78	4.77	4.78	0.006	0.13
P_2O_5	0.026	0.025	0.025	0.025	0.001	4.00
Rb	177.6	177.6	177.6	177.6	0.00	0.00
Sr	46.09	46.09	46.34	46.17	0.14	0.30
Y	41.90	42.38	42.09	42.12	0.24	0.57
Zr	126.8	133.3	121.8	127.3	5.79	4.55
Nb	48.9	49.0	49.3	49.1	0.19	0.39
Mo	3.2	3.5	3.4	3.4	0.15	4.45
Ba	240.2	237.8	241.0	239.7	1.67	0.70
Pb	24.02	23.51	23.39	23.64	0.33	1.40
Th	25.03	24.36	24.44	24.61	0.37	1.50

S.D. = standard deviation at the 1 sigma level
C.V. = coefficient of variation, defined as:
[(S.D. / Mean) 100]

APPENDIX G (continued)

XRF Precision
Cumulative

Element	Mean	S.D.	C.V.(%)
SiO_2	76.03	0.27	0.36
TiO_2	0.157	0.001	0.64
Al_2O_3	12.87	0.06	0.47
Fe_2O_3	1.22	0.02	1.64
MnO	0.053	0.002	3.77
MgO	0.25	0.06	24.00
CaO	0.64	0.02	3.13
Na_2O	3.95	0.02	0.51
K_2O	4.79	0.05	1.04
P_2O_5	0.024	0.002	8.33
Rb	180.3	2.3	1.28
Sr	44.65	1.71	3.83
Y	43.13	1.19	2.76
Zr	128.9	1.41	1.09
Nb	49.8	0.68	1.37
Mo	3.5	0.14	4.00
Ba	232	12	5.17
Pb	24.00	0.71	2.96
Th	25.79	1.12	4.34

S.D. = standard deviation at the 1 sigma level
C.V. = coefficient of variation, defined as:
[(S.D. / Mean) 100]

APPENDIX H

PARTITION COEFFICIENTS

This appendix gives a tabulation of partition coefficients used in Rayleigh fractionation modeling as well as a list of sources used.

APPENDIX H (continued)

Element	San	Plag	Bio	Hbl	Mgt	Ilm
Sc	0.03	0.17	15.50	10.00	8.90	8.00
Rb	0.74	0.16	5.30	0.01	0.00	0.00
Sr	2.00	10.00	0.53	0.02	0.15	0.00
Y	0.10	0.07	1.00	6.00	1.00	0.10
Zr	0.05	0.36	1.80	4.00	0.80	1.00
Nb	0.05	0.06	9.50	4.00	2.50	3.00
Cs	0.20	0.05	2.40	0.02	0.00	0.00
Ba	5.20	1.40	3.70	0.04	0.00	0.00
La	0.063	0.55	3.55	0.33	26.00	0.00
Ce	0.034	0.40	3.49	1.50	22.90	0.00
Sm	0.017	0.20	1.76	7.80	12.49	0.00
Eu	2.80	5.40	0.87	5.00	2.80	0.00
Tb	0.092	0.18	1.20	12.00	7.50	0.10
Yb	0.022	0.15	0.69	8.00	1.00	0.10
Lu	0.070	0.12	0.80	5.50	0.91	0.10
Hf	0.015	0.18	0.68	1.40	1.80	0.70
Ta	0.025	0.13	1.30	1.50	1.13	30.00
Pb	2.50	0.60	0.70	0.00	0.00	0.00
Th	0.016	0.20	1.74	0.01	13.10	0.40
U	0.022	0.15	0.19	0.40	0.21	0.00

Sources: Higuchi and Nagasawa (1969)
Schnetzler and Philpotts (1970)
Nagasawa and Schnetzler (1971)
Arth (1976)
Mahood and Hildreth (1983)
Michael (1983)
Nash and Crecraft (1985)

APPENDIX H (continued)

Element	Zir	All	Ap	Cpx	Opx
Sc	68.70	49.40	0.00	83.00	7.00
Rb	0.00	0.00	0.00	0.03	0.003
Sr	0.00	100.00	2.00	0.52	0.01
Y	60.00	100.00	40.00	4.00	1.00
Zr	6400.00	2.00	0.10	0.60	0.20
Nb	50.00	2.00	0.10	0.80	0.80
Cs	0.00	0.00	0.00	0.01	0.30
Ba	0.00	0.00	2.00	2.30	0.003
La	16.90	2362.00	20.00	11.80	0.10
Ce	16.80	2063.00	35.00	10.30	0.15
Sm	14.40	756.00	63.00	9.55	0.25
Eu	16.00	122.00	30.00	4.60	0.17
Tb	37.00	235.00	20.00	1.80	0.65
Yb	527.00	24.50	25.00	4.10	0.85
Lu	642.00	22.00	25.00	3.80	0.90
Hf	3742.00	9.80	0.10	0.37	0.10
Ta	47.50	1.90	0.00	0.77	0.15
Pb	0.00	0.00	0.00	0.00	0.00
Th	76.80	420.00	2.00	5.41	0.15
U	340.50	14.00	0.00	0.07	0.006

Sources: Higuchi and Nagasawa (1969)
Schnetzler and Philpotts (1970)
Nagasawa and Schnetzler (1971)
Arth (1976)
Mahood and Hildreth (1983)
Michael (1983)
Nash and Crecraft (1985)

REFERENCES CITED

Aldrich, M.J., 1986, Tectonics of the Jemez Lineament in the Jemez Mountains and Rio Grande Rift: Journal of Geophysical Research, v. 91, p. 1753-1762.

Aldrich, M.J., Chapin, C.E., and Laughlin, A.W., 1986, Stress history and tectonic development of the Rio Grande Rift, New Mexico: Journal of Geophysical Research, v. 91, p. 6199-6211.

Arth, J.G., 1976, Behavior of trace elements during magmatic processes - A summary of theoretical models and their applications: Journal of Research of the U.S. Geological Survey, v. 4, p. 41-47.

Atherton, M.P., 1981, Horizontal and vertical zoning in the Peruvian Coastal Batholith: Journal of the Geological Society of London, v. 138, p. 343-349.

Bacon, C.R., Macdonald, R., Smith, R.L., and Baedecker, P.A., 1981, Pleistocene high-silica rhyolites of the Coso Volcanic Field, Inyo County, California: Journal of Geophysical Research, v. 86, p. 10223-10241.

Bailey, R.A., Smith, R.L., and Ross, C.S., 1969, Stratigraphic nomenclature of volcanic rocks in the Jemez Mountains, New Mexico: U.S. Geological Survey Bulletin 1274-P, p. 1-19.

Baker, B.H., and McBirney, A.R., 1985, Liquid fractionation. Part III: Geochemistry of zoned magmas and the compositional effects of liquid fractionation: Journal of Volcanology and Geothermal Research, v. 24, p. 55-81.

Bateman, P.C., and Chappell, B.W., 1979, Crystallization, fractionation, and solidification of the Tuolumne Intrusive Series, Yosemite National Park: Geological Society of America Bulletin, v. 90, p. 465-482.

Bence, A.E., and Albee, A.L., 1968, Empirical correction factors for electron microanalysis of silicates and oxides: Journal of Geology, v. 76, p. 382-403.

Brown, W.L., and Parsons, I., 1981, Towards a more practical two-feldspar geothermometer: Contributions to Mineralogy and Petrology, v. 76, p. 369-377.

Brown, W.L., and Parsons, I., 1985, Calorimetric and phase diagram approaches to two-feldspar geothermometry: A critique: American Mineralogist, v. 70, p. 356-361.

Buddington, A.F., and Lindsley, D.H., 1964, Iron-titanium oxide minerals and synthetic equivalents: Journal of Petrology, v. 5, p. 310-357.

Cameron, K.L., and Hanson, G.N., 1982, Rare earth element evidence concerning the origin of voluminous mid-Tertiary rhyolitic ignimbrites and related volcanic rocks, Sierra Madre Occidental, Chihuahua, Mexico: Geochimica et Cosmochimica Acta, v. 46, p. 1489-1503.

Cameron, K.L., 1983, The Bishop Tuff revisited: Isotope dilution REE data consistent with crystal fractionation: EOS (American Geophysical Union Transactions), v. 64, p. 883.

Cameron, K.L., 1984, Bishop Tuff revisited: New REE data consistent with crystal fractionation: Science, v. 224, p. 1338-1340.

Carrigan, C.R., and Cygan, R.T., 1986, Implications of magma chamber dymanics for Soret-related fractionation: Journal of Geophysical Research, v. 91, p. 11451-11461.

Christiansen, E.H., Burt, D.M., Sheridan, M.F., and Wilson, R.T., 1983, Petrogenesis of topaz rhyolites from the western United States: Contributions to Mineralogy and Petrology, v. 83, p. 16-30.

Christiansen, E.H., Bikun, J.V., Sheridan, M.F., and Burt, D.M., 1984, Geochemical evolution of topaz rhyolites from the Thomas Range and Spor Mountain, Utah: American Mineralogist, v. 69, p. 223-236.

Christiansen, E.H., Sheridan, M.F., and Burt, D.M., 1986, The geology and geochemistry of Cenozoic topaz rhyolites from the western United States: Geological Society of America Special Paper 205, 82 p.

Condie, K.C., 1978, Geochemistry of Proterozoic granitic plutons from New Mexico, U.S.A.: Chemical Geology, v. 21, p. 131-149.

Dalrymple, G.B., 1979, Critical tables for conversion of K-Ar ages from old to new constants. Geology, v. 7, p. 558-560.

Deer, W.A., Howie, R.A., and Zussman, J., 1982, An introduction to the rock forming minerals: London, Longman, 528 p.

Doell, R.R., Dalrymple, G.B., Smith, R.L., and Bailey, R.A., 1968, Paleomagnetism, potassium-argon ages, and geology of rhyolites and associated rocks of the Valles Caldera, New Mexico: *in* Coats, R.R., Hay, R.L., and Anderson, C.A., eds., Studies in Volcanology: Geological Society of America Memoir 116, p. 211-248.

Eichelberger, J.C., 1980, Vesiculation of mafic magma during replenishment of silicic magma reservoirs: Nature, v. 288, p. 446-450.

Ewart, A., 1971, Chemical changes accompanying spherulitic crystallization in rhyolitic lavas, Central Volcanic Region, New Zealand: Mineralogical Magazine, v. 38, p. 424-434.

Ewart, A., 1979, A review of the mineralogy and chemistry of Tertiary-recent dacitic, latitic, rhyolitic, and related salic volcanic rocks, *in* Barker, F., ed., Trondhjemites, dacites, and related rocks, New York, Elsevier, p. 13-121.

Gardner, J.N., and Goff, F., 1984, Potassium-argon dates from the Jemez Volcanic Field: Implications for tectonic activity in the north-central Rio Grande rift, *in* Baldridge, W.C., Dickerson, P.W., Riecker, R.E., and Zidek, J., eds., New Mexico Geological Society Guidebook, 35th Field Conference, Rio Grande rift: Northern New Mexico: New Mexico Bureau of Mines and Mineral Resources, Socorro, New Mexico, p. 75-81.

Gardner, J.N., Goff, F., Garcia, S., and Hagan, R.C., 1986, Stratigraphic relations and lithologic variations in the Jemez Volcanic Field, New Mexico: Journal of Geophysical Research, v. 91, p. 1763-1778.

Gladney, E.S., and Burns, C.E., 1983, 1982 compilation of elemental concentrations in 11 U.S.G.S. rock standards: Geostandards Newsletter, v. 7, no. 1, p. 3-226.

Goff, F., Heiken, G.H., Tamanyu, S., Gardner, J., Self, S., Drake, R., and Shafiqullah, M., 1984, Location of Toledo Caldera and formation of the Toledo Embayment, Jemez Mountains, New Mexico: EOS (American Geophysical Union Transactions), v. 65, p. 1145.

Goff, F., Rowley, J., Gardner, J.N., Hawkins, W., Goff, S., Charles, R., Wachs, D., Maasen, L., and Heiken, G., 1986, Initial results from VC-1, first Continental Scientific Drilling Program corehole in Valles Caldera: Journal of Geophysical Research, v. 91, p. 1742-1752.

Green, N.L., and Usdansky, S.I., 1986, Ternary feldspar mixing relations and thermobarometry: American Mineralogist, v. 71, p. 1100-1108.

Griggs, R.L., 1964, Geology and groundwater resources of the Los Alamos area, New Mexico: U.S. Geological Survey Water Supply Paper 1753, 81 p.

Hammarstrom, J.M., and Zen, E-an, 1986, Aluminum in hornblende: An empirical igneous geobarometer: American Mineralogist, v. 71, p. 1297-1313.

Hanson, G.N., 1978, The application of trace elements to the petrogenesis of igneous rocks of granitic composition: Earth and Planetary Science Letters, v. 38, p. 26-43.

Hawthorne, F.C., 1981, Crystal chemistry of the amphiboles, *in* Veblen, D.R., ed., Amphiboles and other hydrous pyriboles - mineralogy: Mineralogical Society of America Reviews in Mineralogy, v. 9A, p. 1-102.

Heiken, G., Goff, F., Stix, J., Tamanyu, G., Shafiqullah, M., Garcia, S., and Hagan, R., 1986, Intracaldera volcanic activity, Toledo Caldera and Embayment, Jemez Mountains, New Mexico: Journal of Geophysical Research, v. 91, p. 1799-1815.

Heiken, G., and Goff, F., 1983, Hot dry rock geothermal energy in the Jemez volcanic field, New Mexico: Journal of Volcanology and Geothermal Research, v. 15, p. 223-246.

Higuchi, H., and Nagasawa, H., 1969, Partition of trace elements between rock-forming minerals and the host volcanic rocks: Earth and Planetary Science Letters, v. 7, p. 281-287.

Hildreth, W., 1979, The Bishop Tuff: Evidence for the origin of compositional zonation in silicic magma chambers: *in* Chapin, C.E., and Elston, W.E., eds., Ash flow tuffs: Geological Society of America Special Paper 180, p. 43-75.

Hildreth, W., 1981, Gradients in silicic magma chambers: Implications for lithospheric magmatism: Journal of Geophysical Research, v. 86, p. 10153-10192.

Hollister, L.S., Grissom, G.C., Peters, E.K., Stowell, H.H., and Sisson, V.B., 1987, Confirmation of the empirical correlation of Al in hornblende with pressure of solidification of Calk-Alkaline plutons: American Mineralogist, v. 72, p. 231-239.

Huppert, H.E., Sparks, R.S.J., and Turner, J.S., 1982a, Effects of volatiles on mixing in Calk-Alkaline magma systems: Nature, v. 297, p. 554-557.

Huppert, H.E., Turner, J.S., and Sparks, R.S.J., 1982b, Replenished magma chambers: Effects of compositional zonation and input rates: Earth and Planetary Science Letters, v. 57, p. 345-357.

Huppert, H.E., and Sparks, R.S.J., 1984, Double-diffusive convection due to crystallization in magmas: Annual Review of Earth and Planetary Sciences, v. 12, p. 11-37.

Izett, G.A., Obradovich, J.D., Naeser, C.W., and Cebula, G.T., 1981, Potassium-argon and fission-track zircon ages of Cerro Toledo rhyolite tephra in the Jemez Mountains, New Mexico: U.S. Geological Survey Professional Paper 1199-D, p. 37-43.

Jacobs, J.W., Korotev, R.L., Blanchard, D.P., and Haskins, L.A., 1977, A well tested procedure for instrumental neutron activation analysis of silicate rocks and minerals: Journal of Radioanalytical Chemistry, v. 40, p. 93-114.

Jezek, P.A., and Noble, D.C., 1978, Natural hydration and ion exchange of obsidian: An electron microprobe study: American Mineralogist, v. 63, p. 266-273.

Kite, W.M., Self, S., Goff, F.E., and Wright, J.V., 1982, Pliocene explosive volcanism in the Jemez Mountains, New Mexico: EOS (American Geophysical Union Transactions), v. 63, p. 1131.

Kochnar, N., 1977, Post-emplacement alkali modifications in rapidly cooled acid volcanic rocks: American Mineralogist, v. 62, p. 333-335.

Kuentz, D.C., 1986, The Otowi Member of the Bandelier Tuff: A study of the petrology, petrography, and geochemistry of an explosive silicic eruption, Jemez Mountains, New Mexico [M.S. thesis]: Arlington, University of Texas at Arlington, 168 p.

LeBas, M.J., LeMaitre, R.W., Streckeisen, A., and Zanettin, B., 1986, A chemical classification of volcanic rocks based on the total alkali-silica diagram: Journal of Petrology, v. 27, p. 745-750.

Leeman, W.P., and Phelps, D.W., 1981, Partitioning of rare earths and other trace elements between sanidine and coexisting volcanic glass: Journal of Geophysical Research, v. 86, p. 10193-10199.

Lesher, C.E., and Walker, D., 1983, Soret fractionation of high-silica rhyolite magma: EOS (American Geophysical Union Transactions), v. 64, p. 883.

Lesher, C.E., 1986, Effects of silicate liquid composition on mineral-liquid element partitioning from Soret diffusion studies: Journal of Geophysical Research, v. 91, p. 6123-6141.

Lindstrom, D.J., and Korotev, R.L., 1982, TEABAGS: computer programs for instrumental neutron activation analysis: Journal of Radioanalytical Chemistry, v. 70, p. 439-458.

Lipman, P.W., 1965, Chemical comparison of glassy and crystalline rocks: U.S. Geological Survey Bulletin 1201-D, p. D1-D24.

Luth, W.C., Jahns, R.H., and Tuttle, O.F., 1964, The granite system at pressures of 4-10 kilobars: Journal of Geophysical Research, v. 69, p. 759-773.

Mahood, G.A., 1981, Chemical evolution of a Pleistocene rhyolitic center: Sierra La Primavera, Jalisco, Mexico: Contributions to Mineralogy and Petrology, v. 77, p. 129-149.

Mahood, G., and Hildreth, W., 1983, Large partition coefficients for trace elements in high-silica rhyolites: Geochimica et Cosmochimica Acta, v. 47, p. 11-30.

Manning, D.A.C., 1981, The effect of fluorine on liquidus phase relationships in the system Qz-Ab-Or with excess water at 1 kb: Contributions to Mineralogy and Petrology, v. 76, p. 206-215.

Marsh, B.D., and Maxey, M.R., 1985, On the distribution and separation of crystals in convecting magma: Journal of Volcanology and Geothermal Research, v. 24, p. 95-150.

Marvin, R.F., and Dobson, S.W., 1979, Radiometric ages: Compilation B: Isochron/West, v. 26, p. 3-25.

McBirney, A.R., 1980, Mixing and unmixing of magmas: Journal of Volcanology and Geothermal Research, v. 7, p. 357-371.

McBirney, A.R., Baker, B.H., and Nilson, R.H., 1985, Liquid fractionation. Part I: Basic principles and experimental simulations: Journal of Volcanology and Geothermal Research, v. 24, p. 1-24.

McCarthy, T.S., and Groves, D.I., 1979, The Blue Tier Batholith, northeastern Tasmania: A cumulate-like product of fractional crystallization: Contributions to Mineralogy and Petrology, v. 71, p. 193-209.

Michael, P.J., 1983, Chemical differentiation of the Bishop Tuff and other high-silica magmas through crystallization processes: Geology, v. 11, p. 31-34.

Mineyev, D.A., Dikov, Yu.P., Sobolev, B.P., and Borutstayan, V.L., 1966, Differentiation of rare-earth elements under supercritical conditions: Geochemistry International, v. 4, p. 357-359.

Mittlefehldt, D.W., and Miller, C.F., 1983, Geochemistry of the Sweetwater Wash Pluton, California: Implications for "anomalous" trace element behavior during differentiation of felsic magmas: Geochimica et Cosmochimica Acta, v. 47, p. 109-124.

Nagasawa, H., and Schnetzler, C.C., 1971, Partitioning of rare earth, alkali and alkaline earth elements between phenocrysts and acidic igneous magma: Geochimica et Cosmochimica Acta, v. 35, p. 953-968.

Nash, W.P., and Crecraft, H.R., 1981, Evolution of silicic magmas in the upper crust: An experimental analog: EOS (American Geophysical Union Transactions), v. 62, p. 1075.

Nash, W.P., and Crecraft, H.R., 1985, Partition coefficients for trace elements in silicic magmas: Geochimica et Cosmochimica Acta, v. 49, p. 2309-2322.

Nilson, R.H., McBirney, A.R., and Baker, B.H., 1985, Liquid fractionation. Part II: Fluid dynamics and quantitative implications for magmatic systems: Journal of Volcanology and Geothermal Research, v. 24, p. 25-54.

Norrish, K., and Hutton, J.T., 1969, An accurate X-ray spectrographic method for the analysis of a wide range of geological samples: Geochimica et Cosmochimica Acta, v. 33, p. 431-453.

Norrish, K., and Chappell, B.W., 1977, X-ray flourescense spectrometry, *in* Zussman, J., ed., Physical methods in determinative mineralogy: New York, Academic Press, p. 201-272.

Prigmore, S.M., 1978, Mineralogical, petrological, and geochemical aspects of Pleistocene low temperature rhyolites of the Tewa Group, Jemez Mountains, New Mexico [Ph.D. thesis]: Dallas, Southern Methodist University, 83 p.

Rice, A., 1981, Convective fractionation: A mechanism to produce cryptic zoning (macrosegregation), layering, crescumulates, banded tuffs and explosive volcanism in igneous processes: Journal of Geophysical Research, v. 86, p. 405-417.

Roedder, E., 1979, Silicate liquid immiscibility in magmas, *in* Yoder, H.S., Jr., ed., The evolution of the igneous rocks - fiftieth anniversary perspectives: Princeton, Princeton University Press, p. 15-57.

Ryerson, F.J., and Hess, P.C., 1978, Implications of liquid-liquid distribution coefficients to mineral-liquid partitioning: Geochimica et Cosmochimica Acta, v. 42, p. 921-932.

Schnetzler, C.C., and Philpotts, J.A., 1970, Partition coefficients of rare-earth elements between igneous matrix and rock-forming mineral phenocrysts - II: Geochimica et Cosmochimica Acta, v. 34, p. 331-340.

Self, S., Gardner, J.N., and Goff, F.E., 1984, Explosive rhyolitic volcanism in the Jemez Mountains, New Mexico: Vent locations, calderas, and relation to regional structure: EOS (American Geophysical Union Transactions), v. 65, p. 1145.

Self, S., Goff, F., Gardner, J.N., Wright, J.V., and Kite, W.M., 1986, Explosive rhyolitic volcanism in the Jemez Mountains: Vent locations, caldera development, and relation to regional structure: Journal of Geophysical Research, v. 91, p. 1779-1798.

Shaw, H.R., 1965, Comments on viscosity, crystal settling, and convection in granitic magmas: American Journal of Science, v. 263, p. 120-152.

Shaw, H.R., Smith, R.L., and Hildreth, W., 1976, Thermogravitational mechanisms for chemical variations in zoned magma chambers: Geological Society of America Abstracts with Programs, v. 8, p. 1102.

Smith, R.L., Bailey, R.A., and Ross, C.S., 1961, Structural evolution of the Valles Caldera, New Mexico, and its bearing on the emplacement of ring dykes: U.S. Geological Survey Professional Paper 424-D, p. D145-D149.

Smith, R.L., and Bailey, R.A., 1968, Resurgent cauldrons, *in* Coats, R.R., Hay, R.L., and Anderson, C.A., eds., Studies in Volcanology: Geological Society of America Memoir 116, p. 613-662.

Smith, R.L., Bailey, R.A., and Ross, C.S., 1970, Geologic map of the Jemez Mountains, New Mexico: U.S. Geological Survey Miscellaneous Investigation Map I-571.

Smith, R.L., 1979, Ash flow magmatism, *in* Chapin, C.E., and Elston, W.E., eds., Ash flow tuffs: Geological Society of America Special Paper 180, p. 5-27.

Sparks, R.S.J., Huppert, H.E., and Turner, J.S., 1984, The fluid dynamics of evolving magma chambers: Philisophical Transactions of the Royal Society of London, v. A310, p. 511-534.

Speer, J.A., 1984, Micas in igneous rocks, *in* Bailey, S.W., ed., Micas: Mineralogical Society of America Reviews in Mineralogy, v. 13, p. 299-356.

Spera, F.J., Yuen, D.A., and Kemp, D.V., 1984, Mass transfer rates along vertical walls in magma chambers and marginal upwelling: Nature, v. 310, p. 764-767.

This thesis is accepted on behalf of the faculty of the Institute by the following committee:

Philip R. Kyle

Advisor

James Neal Gardner

Kenneth C. Condie

31 July, 1987

Date